Improved spectral estimates of climate oscillations in the Quaternary and Neogene

by

Ryan Borowiecki

A thesis submitted in partial fulfillment of the requirements for the degree of

Doctor of Philosophy

in

Geophysics

Department of Physics

University of Alberta

Abstract

Centennial, millennial and multi-millennial scale climate cycles have been observed in paleoclimate proxies distributed globally. Examples of these cyclical climate cycles include oscillations with periods of ~2.3, ~1.5, ~1, and ≤0.5 thousand years (kyr) in the Quaternary. In the Neogene, longer record length and decreased resolution limit observations to longer climate oscillations driven by variations in orbital eccentricity (~400 kyr and ~100 kyr), obliquity (~40 kyr) and precession (~20 kyr). These oscillations have been widely observed in high-resolution marine and continental deposits. Understanding forced climate oscillations related to solar fluctuations and orbital cyclicity is critical in understanding the warming trends currently observed in modern climate records.

For the Holocene, countless studies have related cycles with periods of 2.3, 1 and ≤0.5 kyr to fluctuations in solar intensity received at Earth's surface. For other oscillations such as the 1.5 kyr cycle observed in Northern Hemisphere proxies, there is still some degree of ambiguity on the forcing mechanism behind the cyclical warming/cooling. This is primarily due to difficulty distinguishing cycles from one another; distinguishing this 1.5 kyr cycle from surrounding cycles and determining the onset and cessation of this cycle is crucial to the evaluation of the mechanism driving this cycle. Commonly methods for paleoclimate spectral analysis, such as the Continuous Wavelet Transform and Short-Time Fourier Transform, cannot clearly reveal the onset or cessation of sporadic climatic cycles if neighboring spectral peaks are present within an

octave due to spectral smearing and leakage. Adapting spectral analysis methods such as the Synchrosqueezing Transform (SST), which is commonly used in other disciplines such as speech analysis to paleoclimate proxies, has numerous advantages for Quaternary and Neogene climate research. Chiefly, the improved time-frequency localization can provide more clarity on the onset and cessation as well as the exact period of oscillations. In addition, when the SST is inverted, it can provide a more precise reconstruction of individual climate oscillations, which allows a direct comparison of individual cycles to the proposed forcing mechanism for that cycle. A few real data examples demonstrate the advantages of the SST method.

In the Miocene/Pliocene, the climate oscillations that can be sufficiently resolved are limited to orbital fluctuations; these fluctuations are commonly observed in marine deposits, but less commonly in continental settings. The chief difficulty in observing these cycles in continental deposits is a relatively slow sediment accumulation rate, thus requiring samples collected at a high resolution to observe. High resolution samples collected from a red clay deposit in Northern China coupled with spectral analysis show that these orbital fluctuations have a tremendous impact on continental climate. Orbital obliquity is observed for the first time in the red clay deposits, and it has a particularly strong impact on the sedimentation processes taking place in aeolian settings like the deposit sampled.

Observation of centennial and millennial scale cycles is not just limited to the Holocene, the same solar fluctuations driving Holocene climate change can be observed in late Pleistocene records as well. Several proxies with sufficient resolution of the shorter millennial and centennial scale oscillations extrapolate the solar influence on

climate ahead of the Holocene. Spectral analysis on high resolution pollen concentration records from Lake Kotokel in southern Siberia, Russia, during the Last Glacial Maximum (LGM) reveals many of the same oscillations observed in the Holocene. Demonstrating that climate fluctuations in the LGM and Holocene are similar in the time-frequency domain suggests that linkages between climate proxies and solar activity at the centennial time scale in the Holocene can be extended to the LGM.

Preface

This dissertation is submitted for the degree of Doctor of Philosophy in Geophysics at the University of Alberta. The research described herein is original, and neither this nor any substantially similar dissertation was or is being submitted for any other degree or other qualification at any other university.

A version of **chapter 2** is under revision with *Computers & Geosciences*. I was responsible for code development, data analysis, figure preparation and manuscript writing.

A manuscript, including the contents of **chapter 3** of this thesis, is being prepared to be submitted to the Journal for Geophysical Research. I am responsible for code development, data analysis, figure preparation, and manuscript writing.

A version of **chapter 4** has been published as Kravchinsky, V. A., Zhang, R., Borowiecki, R., Tarasov, P. E., van der Baan, M., Anwar, T., Goguitchaichvili, A., & Müller, S. (2021). Centennial scale climate oscillations from southern Siberia in the Last Glacial Maximum. Quaternary Science Reviews, 270, 107171. I was responsible for the age model development and contributed substantially to writing, especially to the analysis and discussion.

One more manuscript was completed during the thesis preparation: Kravchinsky, V. A., Borowiecki, R., Zhang, R., Czarnecki, J., Czarnecki, A., Boers, N., Berger, A., Billups, K., Goguitchaichvili, A., & van der Baan, M. (2023). Deciphered periodicities of the Dansgaard-Oeschger and Heinrich climate events. The manuscript is currently under

review. With other lead co-authors, I was responsible for the data analysis, figure preparation and manuscript writing.

Acknowledgements

I would like to express my gratitude to my supervisors Dr. Vadim Kravchinsky and Dr. Mirko van der Baan. Their support, motivation, knowledge, and expertise were invaluable in the completion of my thesis research. I truly appreciate their efforts, guidance, time invested, and mentoring through my PhD.

I would also like to thank my PhD final exam committee members, Dr. Mauricio Sacchi, Dr. Joseph Maciejko, and Dr. Philippe Sorrel for their feedback which helped in improving the quality of my thesis. I would also like to thank Dr. Andrzej Czarnecki for their suggestions and discussion on spectral analysis and Dr. Britta Jensen for feedback and recommendations on Quaternary climate.

I am also very appreciative of my colleagues in the Department of Physics, the Paleomagnetic Laboratory at the University of Alberta, and the State Key Laboratory of Continental Dynamics at Northwest University (NWU); discussions with them were always insightful and inspirational. Special thanks go to Prof. Rui Zhang (NWU) for his support and assistance during my field trip to China.

Finally, I would like to extend gratitude to my partner, family, and friends whose encouragement and support have helped me succeed in my academic career.

Contents

List of Tables

List of Figures

1. Introduction

1.1 Background

Paleoclimatology describes the study of changes in Earth's climate over timescales ranging from hundreds to millions of years. These changes can be brought about by external forcing driven by astronomical phenomena such as variations in the earth's orbit around the sun, or by numerous factors internal to Earth's atmospheric system such as changes in ocean water circulation of ice sheet cover. Climate variations can present themselves as either an abrupt single occurrence such as the Permian-Triassic Extinction, or cyclical events that are periodically repeated. The study of these cyclical and spontaneous events is of interest to earth scientists as it provides the ability to determine causal relationships between forcing mechanisms for climate change and the climatic response to those mechanisms. Establishing and solidifying these complex relationships is a key component in understanding the climate change challenges currently facing society as it allows scientists to address natural evolution and better quantify the extent of anthropogenic impact on climate.

Modern climatological records only extend back several hundred years at most,representing a snapshot in geologic time, these records do not provide sufficient record length to observe cyclical variations longer than ~100 years as an insufficient

number of observed wavelengths would be present (Oppenheim and Schafer, 1999). Instead, to study cyclical climate variations, proxies from the geologic record are used to infer specific climatological conditions at the time of deposition. Paleoclimate proxies are the sediment properties which correlate to a certain climatic condition such as wind speed, humidity, precipitation, or temperature that influences that specific sediment property. A wide range of sediment properties can act as proxies; commonly used proxies in paleoclimatology include oxygen isotopes, magnetic susceptibility, sediment grain size, ice rafted debris, biogenic material, and many other geochemical parameters. Numerous factors dictate the proxy type used including the study location, accessibility to samples, geologic setting, along with diagenetic history typically dictate which proxies are available for analysis. Holocene climate analysis, for example, has several proxies available, including ice rafted debris, biogenic silica, along with ice core and biogenic $\delta^{18}O$, and others. In earlier time periods, such as the Pliocene, geographical areas with sediment that have not been altered by secondary processes are more limited thus restricting the number of effective proxies. A set of conditions necessary for a sedimentary succession to be an effective paleoclimate proxy are listed below:

- Succession must have a measurable sedimentary property that is influenced by climatological conditions, including wind intensity, precipitation/groundwater presence, or temperature.
- Sedimentation rates should be consistent with no discontinuities in sediment supply.
- Method of obtaining an accurate age model for succession must be available, ideally multiple dating methods are present for a given deposit to ensure the accuracy of dating.

- Sediment should not be subject to post-depositional alterations which effectively remove or mask climatic conditions present at the time of deposition.

Once a suitable proxy has been identified for the study area and target geologic period, obtaining a paleoclimate proxy record requires numerous steps and considerations surrounding how the proxy responds to climatic fluctuations, sampling criteria, sedimentation rate and age model determination. Analysis of paleoclimate proxies poses numerous challenges in identifying climate cyclicity, in particular low resolution relative to the oscillatory period. Paleoclimate proxies tend to be low resolution in comparison to other time series, such as speech records or seismic data; this can limit the detection of short period cycles where the sampling rate does not meet the Nyquist criterion (Nyquist, 1924). This criterion states that to adequately sample a simple sinusoidal oscillation, the sampling frequency must be at minimum twice the highest frequency present in the oscillation.

This criterion specifies the minimum frequency necessary and represents a signal that is sampled at the edge of reconstructability. It is entirely possible to sample the oscillation as zero when sampling at the Nyquist criterion as demonstrated in Fig. 1.1 where both the red and blue dots are sampled at the Nyquist frequency but result in two very different signal reconstructions. Sampling below the Nyquist frequency can introduce low frequency noise through aliasing. It is difficult to impossible to sample a paleoclimate proxy at exactly the Nyquist frequency due to variations in sedimentation rate and compaction, which would translate into a variable sampling interval. Instead, it is best practice when sampling a signal to sample at a rate higher than the Nyquist criterion

specifies to ensure all high frequency oscillations are captured and do not introduce low frequency artifacts through aliasing.
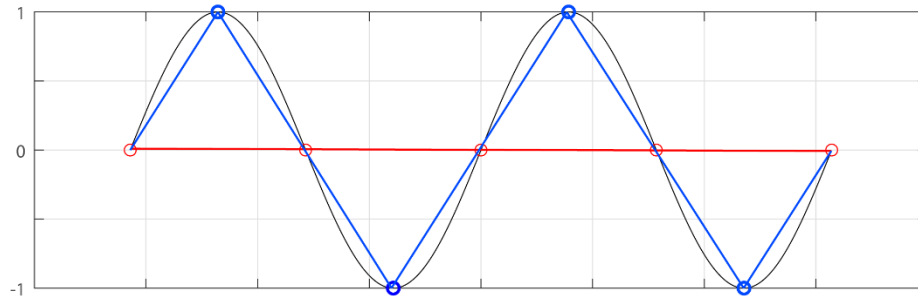
Fig 1.1 Sketch depicting a cosine oscillation sampled at the Nyquist frequency with at least two samples per full wavelength. Black line shows the cosine oscillation being samples, red circles and line represent sampling zero crossings at the Nyquist frequency. Blue circles and lines representing sampling the peaks and troughs at the Nyquist frequency.

Record lengths can also be limited by the extent of sedimentary succession available to sample and when that sediment was deposited. This short record length in relation to the period of the climate cycles of interest results in several intervals, such as during the Holocene, where a relatively small number of full oscillations are recorded by the proxy. Cycles can be sporadic in the record, such as the Holocene 1.5 kyr cycle, further limiting the number of full oscillations present to analyze. When an insufficient number of full oscillations are captured in the analysis window, the spectral peaks in the time-frequency transform are widened along the frequency axis, making precise determination of the instantaneous period more difficult (Oppenheim and Schafer, 1999).

Measured as a function of total section depth, these paleoclimate proxies do not describe temporal climatic evolution alone, one additional step must be taken to obtain a paleoclimate time series to analyze. This step involves determining the sediment accumulation rate and applying this rate to convert section depth to geologic age. Sediment accumulation rate is typically determined either by direct measurements (i.e. radiocarbon dating) or observations of events of known geologic age. Certain sections contain several useful age markers which all contribute to the development of an exceptional age model, for instance, Seierstad et al. (2014) incorporated the age model constraints for several Greenland ice cores to refine the age model for the NGRIP ice core. This age model improvement allows for the detection of sub-millennial scale climate oscillations in the re-dated oxygen isotope record. Other sections, such as the red clay deposits in Northern China, have limited dating options available and are presently limited to only magnetostratigraphy and cyclostratigraphy; Anwar et al. (2015) propose both methods be used jointly to date these types of succession.

The Holocene (present day - 11.7 ka) is one of the most widely analyzed periods within the last ~20 years, with many proxies available across the Northern and Southern hemispheres. In addition to the abundance of well dated proxies, several proxies such as the Ice Rafted Debris record published by Bond et al. (1997) have been re-analyzed using the CWT in numerous publications (Debret et al., 2007; Kravchinsky et al., 2013; Soon et al., 2014). Through the Holocene, climate cycles with millennial periods of 0.5 kyr, 1 kyr, 1.5 kyr, and 2.4 kyr have been identified in a number of proxies (van Geel et al., 1999; Bond et al., 2001; Hu et al., 2003; Niggemann et al., 2003; Debret et al., 2007; Debret et

al., 2009; Sorrel et al., 2012; Kravchinsky et al., 2013; Soon et al., 2014; Usoskin et al., 2016; Allan et al., 2018). The vast majority publications agree on the nature and forcing mechanism of the 0.5 kyr, 1 kyr and 2.4 kyr cycles, and have attributed these oscillations to variations in solar activity due to the presence of these cycles in solar activity reconstructions using ^{10}Be and ^{14}C isotopes.

The nature of the 1.5 kyr cycle is not as well-understood and numerous publications note the presence of this cycle in spectral analysis provide drastically different explanations for the cycle. Proposed drivers include north-atlantic ocean water circulation (Debret et al., 2009; Sorrel et al., 2012; Di Rita et al., 2018), and solar output fluctuations (Soon et al., 2014). Other work suggests the 1.5 kyr cycle could be an artifact of spectral analysis, and 'admixing' of two spectral peaks with periods longer and shorter than the central 1.5 kyr peak (Clemens, 2005; Obrochta et al., 2012). Another interpretation of this cycle is that it is the same underlying phenomena driving the 1 kyr cycle however, the period of this forcing mechanism or the climatic response to forcing slows down in the late Holocene to explain the transition from 1 kyr to 1.5 kyr (Ramos-Román at al., 2018). This hypothesis is supported by the fact that in certain proxies, the 1.5 kyr cycle is only present when the 1 kyr cycle is absent from the spectra. Resolving ambiguity around the 1.5 kyr cycle extends past the Holocene as some researchers consider this period to be the fundamental pacing of Dansgaard-Oeschger oscillations through the Pleistocene (Schulz, 2002; Rahmstorf, 2003). The Holocene benefits from having a very wide array of proxies available for analysis, distributed across the globe but particularly in the Northern Hemisphere. In addition, the proxies available are often of high resolution and are sampled much higher than the Nyquist criterion specifies. Despite

this, inconsistencies in the identification and interpretation of the 1.5 kyr persist and it is still not well understood what is driving this cycle and how it is distributed across the Northern Hemisphere.

Shorter period obliquity and precession cycles have yet to be demonstrated in the red clay deposits and are rarely demonstrated in continental settings, thus there is uncertainty surrounding how these orbital fluctuations impact continental climate. Red clay deposits are sensitive to temperature and precipitation due to alternations of magnetic mineralogy taking place during pedogenesis as demonstrated by Nie et al. (2007). Increased moisture content and temperature during the soil forming process increases the oxidation rate of hematite producing superparamagnetic maghemite which is detected in Magnetic Susceptibility (MS) and Frequency Dependence (FD). The absence of demonstrated obliquity cycles could be caused by numerous factors including erroneous age models, lack of sufficient sampling resolution, or frequency smearing in spectral analysis masking specific signals. These pitfalls have limited our ability to fully understand not just the long term east Asian winter monsoon variability, but on a broader scale how the shorter period orbital cycles influence continental climate.

1.2 Motivation and Contribution

As society faces the urgent threats of climate change, understanding and quantifying the extent of natural evolution taking place in the absence of anthropogenic influence is increasingly important as this evolution dictates, in part, how the climate will continue to evolve in the future. Understanding how past climates evolved depends on

resolving ambiguities described above. The methodology applied to obtain and analyze an effective paleoclimate proxy varies between studies and the lack of a consistent and repeatable framework not subject to visual interpretation is a probable source of this ambiguity.

This research will investigate methods which can be implemented to more accurately identify specific paleoclimate cycles to improve our understanding of how external forcing mechanisms influence climate. This will be done by addressing specific challenges present when analyzing three distinct geologic time periods, each of which presents specific pitfalls in obtaining accurate depictions of climate cyclicity. The process of obtaining the most accurate estimates of paleoclimate cyclicity starts at the sampling stage to ensure the Nyquist criterion is met for the climate signals of interest. It is also heavily dependent on the development of a robust age model to ensure cycles are timed appropriately prior to spectral analysis. Finally, the spectral analysis applied should be consistent and repeatable to ensure estimates of cyclicity are not subject to visual interpretation. When considered together, the methodology described in each chapter represents an effective process to obtain the most reliable paleoclimate interpretations.

1.3 Thesis Overview

Chapter 2 illustrates how the Synchrosqueezing Transform (SST) can be applied to paleoclimate data from the Holocene to improve cyclicity estimates by removing the visual interpretation aspect from estimates and improve consistency between records. A detailed evaluation of spectral analysis techniques common in paleoclimatology is

performed using synthetic data. These methods are compared to the SST to illustrate the advantages the SST presents in terms of time-frequency localization. Advantages of the Inverse Synchrosqueezing (ISST) Transform are demonstrated by analyzing four different Holocene paleoclimate proxies distributed across the Northern Hemisphere to obtain an estimate of paleoclimate cyclicity that is consistent across all four records. The similarities observed in reconstructed oscillations across the Northern Hemisphere using the proposed ISST technique demonstrate the effects of the mid-Holocene transition are observed across the Northern Hemisphere and not just limited to the North Atlantic region.

Chapter 3 addresses challenges that are present when investigating longer scale orbital cyclicity in continental settings, specifically, the preservation of obliquity in the red clay deposits found in the Chinese loess plateau. Age models developed for the section prior to this study are used to determine a sampling interval that exceeds the Nyquist criteria for orbital obliquity, ensuring it will be captured in the record. The high-resolution magnetic susceptibility time series presented in this chapter is subsequently dated using a pre-existing age model and tuned to a numerical orbital eccentricity solution. The methodology described in chapter 2 is then applied to the high resolution magnetic record to extract orbital obliquity oscillations recorded by the red clays. Achieving this allows for a detailed comparison of the amplitude and phase of continental climate removed from oceanic influence to the astronomical solution.

Chapter 4 examines a third geologic period, the Last Glacial Maximum, which occurred prior to the Holocene, when ice sheet coverage across the Northern Hemisphere was widespread and sea surface temperatures were lower than the present day by several

degrees. In comparison to the Holocene climate oscillations, the behavior of centennial and millennial scale climate fluctuations in the late Pleistocene are not as well understood, and until recently records spanning this time period were of insufficient resolution to investigate such fluctuations. In this chapter, the chronology for a high resolution lacustrine succession is revised using a statistical approach to develop a non-linear age model; this succession is compared to other high resolution proxies spanning the same period. Spectral analysis is applied to demonstrate the presence of multiple climate cycles of solar origin, including the solar de Vries cycle, the unnamed 0.5 kyr cycle, and the 1 kyr eddy cycle, all of which are observed in the Holocene. The result of this analysis demonstrates how solar fluctuations, in addition to orbital fluctuations, and persistent aspects of natural climate change.

Chapter 5 presents the conclusions of the thesis and highlights possible directions for future research, discussing methods which can be implemented to further reduce inconsistencies in paleoclimate cyclicity introduced by visual interpretation. This chapter also discusses approaches that could be applied to better quantify any uncertainty in estimates of the period of specific oscillations.

2. The Synchrosqueezing Transform to evaluate paleoclimate cyclicity

2.1 Introduction

During the Holocene, centennial and millennial scale climate cycles are observed in paleoclimate proxies distributed globally with periods of ~2.3, ~1.5, ~1, ≤0.5 kyr; past studies have related the 2.3 kyr, 1 kyr, and ≤0.5 kyr cycles to fluctuations in solar output (Bray, 1968; van Geel et al., 1999; Bond et al., 2001; Hu et al., 2003; Niggemann et al., 2003; Debret et al., 2007; Kravchinsky et al., 2013; Soon et al., 2014; Usoskin et al., 2016; Allan et al., 2018). Solar reconstructions using 14C and 10Be isotopes by Usoskin et al. (2016) show the 2.3 kyr cycle to be present in both records and that it dominates millennial scale solar variability. Analysis of the 9.4 ka records of cosmic radiation and solar activity from ice cores and tree rings confidently showed the presence of the 1 kyr Eddy, unnamed ~0.35 kyr cycle and ~0.21 kyr Suess - de Vries cycles (Steinhilber et al., 2012). Less statistically significant ~0.5 and 0.71 kyr periodicities in the ice cores and tree rings are also reported in some Asian climate records (Steinhilber et al., 2012). Spectral analysis of the solar activity reconstructed from ^{14}C and ^{10}Be isotopes in the

GRIP ice core show distinct peaks around 0.7, 0.5 and 0.35 kyr, as well as the 0.21 kyr Suess - de Vries cycle from 6 ka (Wanner et al., 2008).

The nature of the 1.5 kyr cycle is still not well understood as it has yet to be shown to correspond to any fluctuations in solar activity and no reliable internal feedback mechanism has been suggested that would explain the geographic distribution of this cycle. Studies by Debret et al. (2009) and Sorrel et al. (2012) suggest this cycle is related to ocean water circulation based on analysis of North Atlantic proxies. Sorrel et al. (2012) attribute the cycle to the late Holocene and interpret it to be influenced by the internal variability in the North Atlantic circulation. Darby et al. (2012) argue that Arctic climate oscillations are dominated by the 1.5 kyr cycle that does not match the spectral features of the solar forcing proxies. It has been shown that this cycle, in addition to 1 kyr and 0.5 kyr cycles, is not just limited to the North Atlantic and has been observed in continental soil deposits in Siberia, where oceanic influence is removed (Kravchinsky et al., 2013). A study conducted by Obrochta et al. (2012) suggests that the 1.5 kyr cycle identified in numerous paleoclimate proxy records may just be an artefact in the spectral analysis performed in the original study due to admixing of the 1 and 2.3 kyr cycles, and Clemens (2005) suggest that the cycle is a mixture of ~1.7 and 1.2 kyr oscillations. Soon et al. (2014) propose a solar activity proxy based on NO_3^- in ice cores from East Antarctica; in this study, wavelet analysis shows a weak spectral peak centered around 1.9 kyr; they conclude that rejecting the 1.5-1.8 kyr cycle as a solar forced cycle is premature and that this cycle may correspond to a fundamental solar mode. The importance of deciphering the ~ 1.5 kyr cycle extends past the Holocene as some research points to these oscillations as the fundamental for pacing the Dansgaard-Oeschger events in Greenland

(Schulz, 2002; Rahmstorf, 2003). Other studies carry out statistical analysis and suggest that this periodicity could be a consequence of random processes (Ditlevsen et al., 2007; Peavoy and Franzke, 2010).

Di Rita et al. (2018) observed one cycle with a period of 1.8 kyr in an Arboreal Pollen from the south-central Mediterranean after detrending and performing wavelet analysis and attribute this cycle to North Atlantic Oscillation-like circulation. Smith et al. (2016) observe a cycle with a period of 1.1 kyr in the early Holocene, which grows longer in the late Holocene to a period of nearly 1.5 kyr in a $\delta^{18}O$ speleothem record from a cave in northern Spain. An additional study applied wavelet analysis on a humidity proxy from southern Spain (Ramos-Román et al., 2018) and found cycles of 1.1 kyr and 2.1 kyr in the early Holocene, and note that the presence of the 1.5 kyr cycle in the late Holocene coincides with the absence of the 1.1 kyr cycle. Kravchinsky et al. (2021) demonstrate that the cycles discussed above are not a unique characteristic of the Holocene and are observed in the Last Glacial Maximum.

The periodicity of paleoclimate proxies can be evaluated in a number of different ways, either qualitatively or quantitatively. Qualitative periodicity estimates are formed by identifying the time duration of each peak/trough cycle or by fitting a monochromatic concise oscillation to a record, as seen in Dansgaard et al. (1993), O'Brien et al. (1995), Wanner & Buetikofer (2008), and Sorrel et al. (2012). Other work determines the period of oscillations mathematically by applying a Fourier Transform to the record (Bond et al., 1997; Hu et al., 2003), however, this approach does not take into account changes in the periodicity through time. Contemporary spectral analysis of time series involves applying

a sliding window to the data and evaluating periodicity within this window. Such approaches are implemented using different methods; the Continuous Wavelet Transform is most commonly used in paleoclimatology (Debret et al., 2007; Debret et al., 2009; Fletcher et al., 2012; Kravchinsky et al., 2013; Soon et al., 2014; Allan et al., 2018).

Spectral analysis of paleoclimate proxies presents numerous challenges related to both the physical processes the proxy is recording and our ability to extract information from the proxy. Periods of forced climate cycles may vary slightly throughout the record due to damping from thermal inertia at the poles (Holland and Bitz, 2003) or slight errors in the age model resulting in differences in the period between any two full cycles (Turner et al., 2016). In addition, various spectral analysis methods are observed to have differing time-frequency resolution when applied to seismic time series (Tary et al. 2014). Our study aims to explore the effectiveness of commonly used contemporary methods when applied to the Holocene climate time series, although they may be applied to any time interval. Time-frequency (*t-f*) resolution refers to the method's ability to resolve two signals with similar frequencies and/or overlapping durations.

The Holocene represents a very short snapshot in geologic time; when a spectral analysis is performed to estimate the period of longer cycles (with periods 1/10 to 1/5 the total record length), the observation of such few full wavelengths becomes a large obstacle (Oppenheim and Schafer, 1999). Because of this, spectral estimates, regardless of the technique used, will be subject to poor frequency localization due to spectral smearing (widening of spectral peaks in the frequency domain) as the short record length

effectively shortens the analysis window and makes evaluation of the cycles more challenging in the Holocene.

In this manuscript, we introduce the Synchrosqueezing Transform (SST) and its inverse which is used to decompose a paleoclimate proxy time series into constituent components. Using synthetic test data, we explore the pros and cons of the SST compared to the Short-Time Fourier Transform and Continuous Wavelet Transform. We then analyze various Holocene paleoclimate proxies distributed across the Northern Hemisphere to assess the suitability of the approach to detect and reveal short-duration nonstationary phenomena in data sets with different characteristics. The results of this analysis show that it is possible to detect a sporadic 1.5 kyr cycle in the presence of other non-stationary cycles and to precisely determine the onset and cessation of this cycle, which can be seen across multiple records in the Northern Hemisphere.

2.2 Material and methods

2.2.1 Short-Time Fourier Transform

As described by Allen and Rabiner (1977), the Fourier Transform quantifies the similarity of a signal to a set of basis functions consisting of sines and cosines. The Short-Time Fourier Transform (STFT) is a modified version of the Fourier Transform where the Fourier Transform is only applied over a given window. This Fourier Transform variant can be applied to non-stationary data where oscillatory prions vary with time, common to paleoclimate proxy data. The continuous Short-Time Fourier Transform can be expressed mathematically as

$$S_f(\tau, f) = \int_{-\infty}^{\infty} s(t)\, w(t - \tau) exp\,(-2\pi i f t)\, dt, \qquad (1)$$

where $S_f(\tau, f)$ is the amplitude spectra of the time series $s(t)$, and $w(t\text{-}\tau)$ is the tapered analysis window. This taper applies scaling to the time series in the analysis window to reduce the amplitude near the edge of the window, typically resembling a trapezoid.

This integral is discretized to be computed numerically, such as the Short Time Fourier Transform (STFT) implementation in Matlab

$$S_\tau(f) = \sum_{-\infty}^{\infty} s(t)\, w\big(t - \tau(l - v)\big) exp\,(-2\pi i f t), \qquad (2)$$

where l is the window length and v is the window overlap, both specified as a number of samples. In the above expression, the term $S_\tau(f)$ is a discrete Fourier Transform calculated over a window of length l centered at a time of $\tau(l\text{-}v)$.

2.2.2 Continuous Wavelet Transform

The continuous wavelet Transform is similar to the STFT, however, the analysis taper in the STFT is replaced with a 'parent wavelet' (Ψ) in the CWT, which can be scaled by a factor a and shifted in time by τ. The mathematical foundation of the Continuous Wavelet Transform (CWT) is described in depth in Daubechies (1992). The CWT represents the cross-correlation of the signal with a set of child wavelets (temporally scaled and shifted parent wavelet) and is represented mathematically by the following expression:

$$W_s(a, \tau) = \frac{1}{\sqrt{a}} \int_{-\infty}^{\infty} s(t)\, \Psi\left(\frac{t - \tau}{a}\right) dt, \qquad (3)$$

16

Where $W_s(a, \tau)$ is the CWT of the time series s(t), and Ψ is the mother wavelet

shifted by τ and scaled by a factor of a. The same temporal shift τ is applied to the

mother wavelet as it is in the STFT, but by scaling the mother wavelet, the CWT is not

limited to a fixed window length like the STFT is. The CWT assumes the data outside

each child wavelet is periodic and has a zero mean to obtain a t-f transform, thus, the

input time series needs to be standardized appropriately. $W_s(a, \tau)$ represents coefficients

forming a concentrated time-frequency representation, the actual frequencies are directly

obtained by dividing the central frequency of the wavelet at scale a by the scale itself

using the relation $f=f_0/a$ as described by Mallat and Zhang (1993).

2.2.3 Synchrosqueezing Transform

The Synchrosqueezing Transform (SST) is a frequency reassignment technique

based on the CWT described by Daubechies et al. (2011). The SST concentrates the *t-f*

map around the most representative angular instantaneous frequencies in the wavelet

domain, calculated as the derivative of the Wavelet Transform $W_s(a, \tau)$ with respect to b

using the following relation

$$\omega_s(a, \tau) = \frac{i}{2\pi W_s(a,\tau)} \frac{\partial W_s(a.\tau)}{\partial \tau}, \tag{4}$$

The Synchrosqueezing operation refers to mapping each point in the time-scale

plane to the time-frequency plane; that is, convert every point *(a, τ)* to *(ω_s (a, τ),τ)*

(Daubechies et al. 2011). In other words, the Synchrosqueezing Transform performs re-

assignment on the frequency (or scale) only when mapping the CWT output from the

time-scale plane to the *time-frequency* plane. The SST function T_s *(ω, τ)* is calculated at

the center of a frequency window of width $[\omega_l - \Delta\omega/2, \omega_l + \Delta\omega/2]$, where $\Delta\omega = \omega_l - \omega_{l-1}$ and is expressed mathematically as:

$$T_S(\omega_l, \tau) = \frac{1}{\Delta\omega} \sum_{a_k:|\omega(a_k,\tau)-\omega_l|<\Delta\omega}^{0} W_s(a_k, \tau)\, a^{-\frac{2}{3}} \Delta a_k, \tag{5}$$

where $T_S(\omega_l, \tau)$ is the Synchrosqueezed Transform of the CWT $W_s(a_k, \tau)$. In this expression, the scale a is discretized into k steps, and $\Delta a_k = a_{k-1} - a_k$. The re-assignment is illustrated in Fig. 2.1.

Before Reassignment   **After Reassignment**
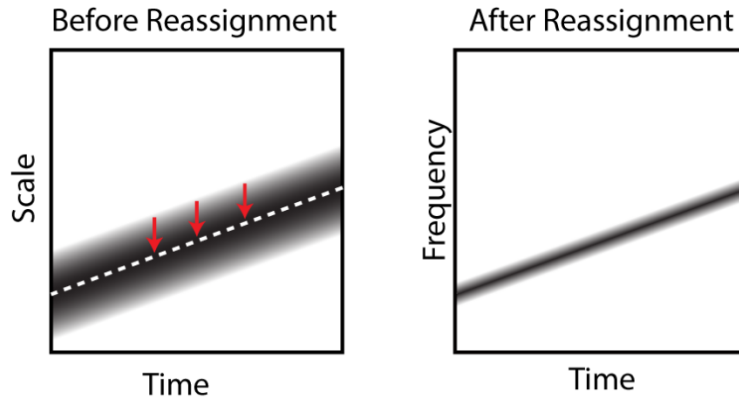
Fig 2.1 Illustration of frequency re-assignment from the time-scale domain to the time-frequency domain. White line before re-assignment indicates instantaneous frequency based on eq (4) and red arrows indicate frequency-reassignment determined by eq (5).

The CWT based SST requires the same input parameters as the CWT (frequency scale and mother wavelet); however, the frequency reassignment offers improved frequency localizations over the CWT, thus facilitating identification of individual signal components. One additional benefit of the SST is that the sparse Transform can be inverted much more reliably, providing an amplitude preserving reconstruction of the original time series or selected portions when compared to simply inverting the CWT.

This is achieved by calculating the inverse CWT over a narrow frequency band around the desired component.

$$s_k(t_a) = 2C_\varphi^{-1}R\sum_l T_S(\omega_l, \tau), \qquad (6)$$

where $T_S(\omega_l, \tau)$ is the Synchrosqueezed wavelet Transform, and C_φ^{-1} is the inverse CWT. See also Herrera et al. (2014, 2015) and Tary et al. (2018) for additional background and illustrative applications of the forward and inverse SST.

The SST can be inverted in different ways that provide varying degrees of user input and constraint on the periods reconstructed based on the t-f transform. One common approach is to perform a ridge extraction which utilizes the instantaneous frequency curves obtained using eq (4) which correspond to the maximum energy in the matrix $T_S(\omega_l, \tau)$ as described in Daubechies et al. (2011). This process allows the user to pre-define the number of ridges to reconstruct as well as a penalty that is assigned to ridges which fall too close to the previously extracted ridge. It is typically best to start with reconstructing the minimum number of ridges then subsequently permit additional ridges until a complete reconstruction is achieved. The alternative to the ridge extraction method is to apply windows, which sets the number of ridges to the number of windows assigned and confines each ridge to the passband of the corresponding window. In this case, no penalty is assigned as this is factored into the decision on the number of windows and the passband of each window; as such it requires some a-priori knowledge of the expected components present in the time-series to achieve a complete reconstruction.

To assign a measure of confidence to spectral peaks, we use the inverse SST in conjunction with a vector dot product to measure the similarity between the original and

19

reconstructed time series. By calculating the dot product between the original record and the reconstruction using specific modes of the inverse SST, we can assign a percentage that each mode contributes to the overall amplitude of the time series. We also include the 95 percent confidence interval calculated using the Monte Carlo method as implemented in methods such as the CWT (Torrence and Compo, 1998).

2.2.4 Synthetic Data

To effectively compare the localization ability of the SST to the CWT and STFT, we generate a synthetic time series with known amplitude, periods, and duration for a 12 kyr interval that roughly corresponds to the Holocene (Fig 2.2). This is done by inputting specific frequencies into a cosine time series with specified durations and superimposing the resultant time series; together forming a synthetic record. The frequencies and durations for each cosine oscillation are defined based on review of literature focusing on the Holocene climate oscillations. The time basis for the synthetic record reflects one time sample every 0.05 kyr through the Holocene that is of the same order as the most high resolution records.
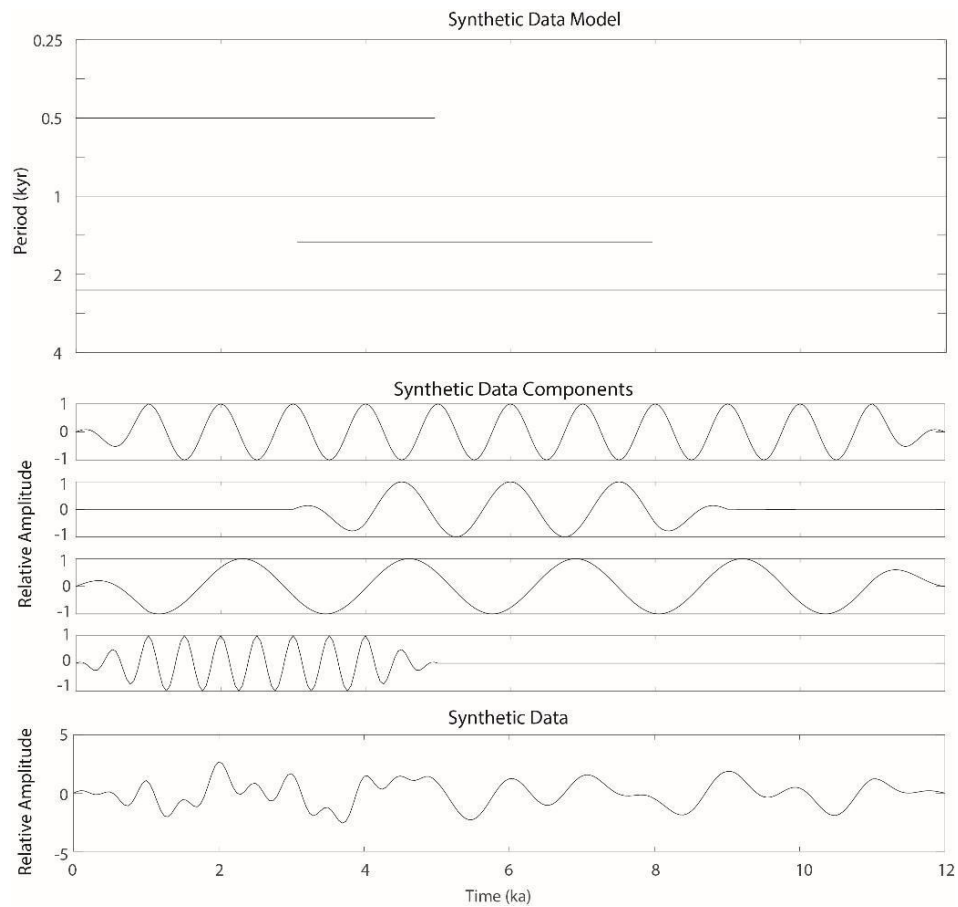
Fig 2.2 a) Model of synthetic data components in the time-frequency domain. b) individual cosine functions of components shown above. c) superstition of all individual components forming synthetic time series for analysis.

The individual components in the frequency domain for this series are shown in Fig 2.2 along with the individual and superposed time domain signals generated by the model. For the synthetic data set, we generate oscillations with periods of 1 kyr and 2.3 kyr for the entire record length, with a shorter 1.5 kyr oscillation from 9 ka to 3 ka as recognized in many climate proxy records (Debret et al., 2007). One additional cycle with

a period of 0.5 kyr is added to the late Holocene (5 ka - present day) to determine how each method performs when sporadic cycles are introduced. The ≤0.5 kyr cycles are also routinely observed in numerous Holocene records (Hu et al., 2003; Clemens, 2005; Steinhilber et al., 2012; Kravchinsky et al., 2013; Lüdecke et al., 2015) and before the Holocene (Adolphi et al., 2014; Kravchinsky et al., 2021). We included the 0.5 kyr cycle in our synthetic model as an illustration of how a short period oscillation influences the total spectra.

2.2.5 Selected Holocene records

We select several illustrative high resolution Holocene records from different parts of the Northern Hemisphere. We intentionally select proxies of different types to assess the suitability of spectral analysis for each type. Each proxy selected is a high resolution, well-dated example for each given type (Petrologic, Isotope, Biogenic, and Organic Content). Each selected proxy exhibits specific characteristics such as abrupt changes, sawtooth oscillations, or high amplitude spikes which may make time-frequency localization more challenging for certain methods (Fig 2.3).
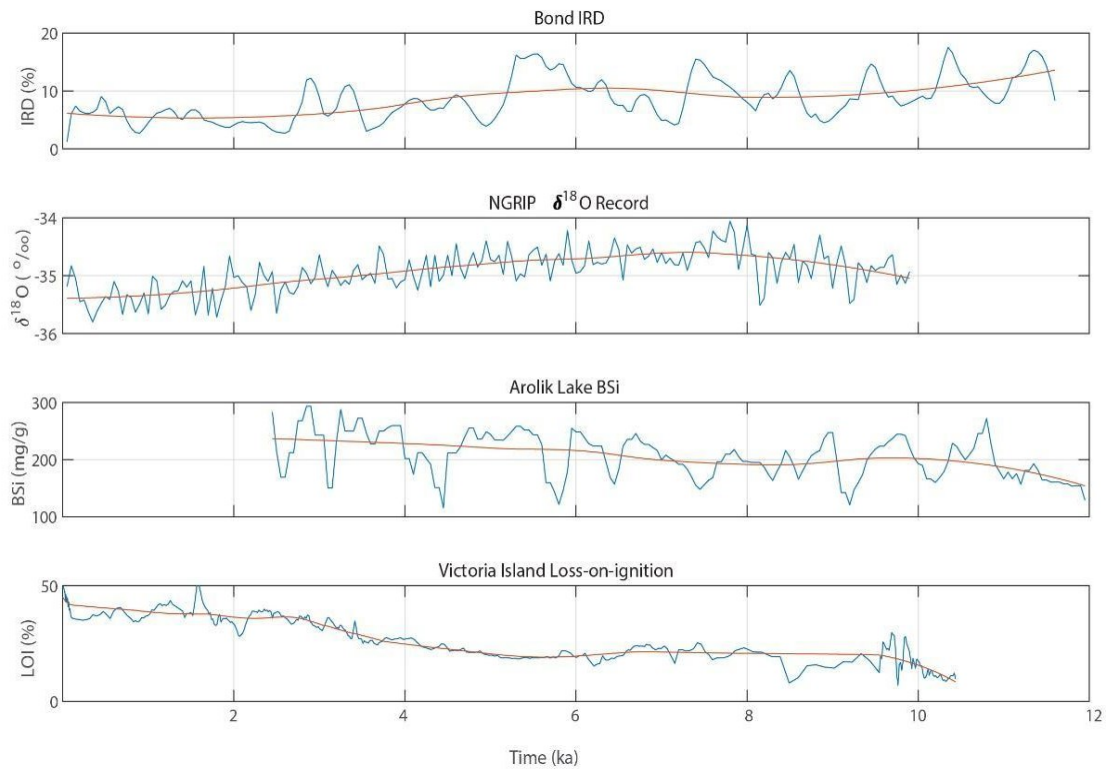
Fig. 2.3. a) Ice rafted debris 'stack' record (Bond et al., 1997). b) Re-dated NGRIP δ18O record (Seierstad et al., 2014). c) BSi record from Arolik Lake, Alaska (Hu et al., 2003). d) Victoria Island organic loss on combustion record (Peros and Gajewski, 2008).

North Atlantic ice-rafted debris

This example uses a classical paleoclimate record for the Holocene published by Bond et al. (1997) (Fig 2.3a). The data set consists of varying percentages of three petrologic tracers found in North Atlantic deep-sea cores which reflect changes in ice drifting; these tracers are hematite stained grains, Icelandic glass, and detrital carbonate. The Ice Rafted Debris (IRD) records are sampled at a resolution between 30 and 50

years; and we resampled the data to a regular interval of 50 years for spectral analysis. An increased presence of the tracers in the deep-sea cores is interpreted as cooler ice bearing surface waters traveling eastward and southward from the Labrador Sea and Nordic Seas and is likely accompanied by strong northerly winds (Bond et al., 2001). Studies have performed spectral analysis on these records in an attempt to report climate cycle periodicity preserved by these records and report on three cycles observed in the record with periods of ~ 2.5 kyr, 1.5 kyr and 1 kyr (Debret et al., 2007, 2009; Obrochta et al., 2012; Kravchinsky et al., 2013). Debret et al. (2007) estimate these periodicities using the CWT and thus may have more uncertainty than indicated due to the spectral smearing associated with the CWT.

Northern Greenland Ice Core Project

One of the highest resolution Holocene datasets published is the North Greenland Ice Core Project (NGRIP) oxygen isotope $\delta^{18}O$ records (Andersen et al., 2004), spanning 123 kyr. Oxygen isotope records from ice cores are an effective temperature proxy as the concentration of the reduced vapor pressure of water containing the heavy oxygen isotope $\delta^{18}O$ causes precipitation to become depleted linearly with condensation temperature (Dansgaard, 1964). Fig 2.3b shows the most recent 11.7 kyr of the NGRIP ice core $\delta^{18}O$ records, the earliest 2 kyr (from 11.7 to 9.7 ka) reflect warming following the Younger Dryas and therefore we analyze the 9.7 kyr interval comparable to the Holocene. The record we use here was re-dated to align with stratigraphy in surrounding ice core records by Seierstad et al. (2014) where they recognize a number of sub-millennial events present. A taper is applied to the shortened record to reduce edge effects in the *t-f*

transformations; this step involves a linear scaling from 0 to 1 of the normalized amplitude for the first and last 1 kyr of the record. The NGRIP $\delta^{18}O$ record has been analyzed for other periods such as during the Last Glacial Maximum (20.6-26 Ka) by Kravchinsky et al. (2021); persistent 0.6 kyr and 1 kyr oscillations were identified in their analysis along with a weak 0.21 kyr cycle using the CWT.

Alaska Arolik Lake biogenic silica records

One of the highest resolution subpolar North Pacific data sets is the biogenic silica (BSi) record of Arolik lake, Alaska (Hu et al., 2003), shown in Fig 2.3c. These BSi variations driven by abundance of single-celled algae are interpreted by Hu et al. (2003) to reflect the global climate changes because they mirror the oxygen isotope variations in ice cores. The studied sedimentary section consists of 3 meters of lacustrine sediment, sampled at an interval 1 cm/sample, and represents a time period from 2.3-12 ka. This translates to a temporal resolution of 45 years/sample on average based on an age model developed through radiocarbon dating of terrestrial plant macrofossils in conjunction with a well-dated tephra layer. Hu et al. (2003) used a traditional Fourier Transform to identify cycles with periods of 135, 170, 195, 435, 590, and 950 years, along with a ~1.5 kyr cycle below the 90% confidence level in their original study. The resolution of this time series makes it a perfect candidate for a more detailed analysis of the temporal evolution of the reported cycles using methods that do not assume stationarity.

Victoria Island pollen organic content

The detailed pollen record from Victoria Island, located in the western part of the Canadian arctic is still one of the only high resolution Holocene climate records in the area (Peros and Gajewski, 2008) (Fig 2.3d). Various measurements were performed on the sediment core collected from the deepest area of an unnamed lake. Peros and Gajewski (2008) established a chronology for the core through radiocarbon dating along with ^{210}Pb dating. The organic content loss-on-ignition (LOI) record has a number of features that correlate with observation records such as the GISP2 ice core and Arolik Lake BSi records as indicated in the original publication. This indicates synchronicity of specific climate events across a large portion of the Northern Hemisphere, which will be further investigated with spectral analysis.

2.3 Calculations

Applying the STFT to the synthetic record is done using eq (2) with a window length of 70 samples or 3.5 kyr, and a window overlap of 68 samples or 3.4 kyr. The CWT is calculated using eq (3) with a Morlet wavelet used as the parent wavelet. The SST is calculated by applying eq (4) to the CWT output to obtain instantaneous frequencies, then performing the Synchrosqueezing using eq (5) to obtain an amplitude spectra using the same Morlet wavelets as the CWT. For these calculations, the thresholding which defines the lowest amplitude oscillations in the CWT that are deemed trustworthy is done using the asymptotically optimal threshold $\sqrt{2\log(n)} * \sigma$, where n is the signal length and σ is the square root of the noise power (Donoho 1995). Fig 2.4

shows spectral analysis results obtained when applying the STFT, CWT, and SST to the synthetic data set.

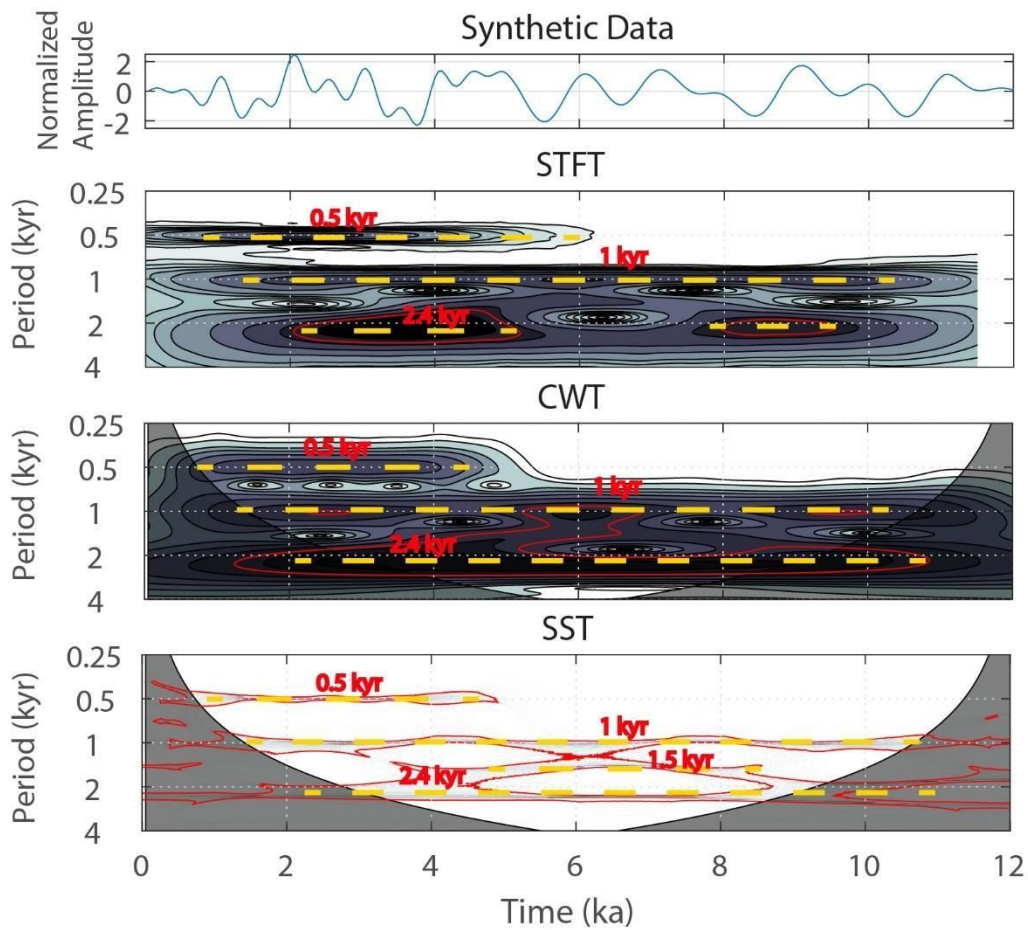Fig. 2.4. a) STFT of synthetic time series calculated with a window width of 3.5 kyr and window overlap of 3.4 kyr. b) CWT of synthetic time series using a Morlet wavelet. c) Synchrosqueezed output of wavelet Transform shown above.

To quantify how the STFT, CWT, and SST perform compared to one another, we calculate the normalized distance between cycles in each synthetic data model and the *t-f*

transform for that synthetic data. This distance is calculated by using the following relation:

$$\text{Dist} = \sum_j \quad \sum_i \quad |A_{ij} - B_{ij}|, \tag{7}$$

where A_{ij} is the model used to create the synthetic data, and B_{ij} is the normalized t-f transform obtained using either the STFT, CWT, or SST. We use this normalized distance as a measure of reconstruction error quantifying how close each method can get to the original input model; a lower normalized distance represents a t-f transform that more closely resembles the input model. Wrap around effects can cause this normalized distance to increase at the edges of the transform, as the window length increases, this area influenced by wrap around is a larger percentage of the record length. For the STFT, this is simple as the window width is fixed, thus the mask replaces values on the edges of the transform with zeros; for the CWT and SST, the mask applied replaces values within the cone of influence (COI) (shaded grey area in Fig 2.4b & 2.4c). The normalized distance is calculated over the entire transform and with the wrap around mask applied; the results are illustrated in Fig. 2.10.

The STFT, CWT, and SST are applied to each of the selected paleoclimate proxies using the same parameters as outlined for the Synthetic Data. With the components of the synthetic data closely matching the components present in Holocene paleoclimate records, the parameters represent an ideal compromise between temporal and frequency localization. Fig(s) 2.11, 2.12, 2.13, and 2.14 show the results of these calculations for each of the selected proxies.

2.4 Results

This synthetic example highlights the benefits of the SST when compared to the CWT and STFT in terms of the improved frequency localization it provides; this is especially apparent in the sporadic signals present in the record. In the case of the sporadic 1.5 kyr cycle, the CWT and STFT have a frequency peak that is not distinguishable from the 2.3 kyr peak within the 95% confidence interval. For the same cycle, the 1.5 kyr peak in the SST does smear into the 2.3 kyr cycle at the onset and cessation of the cycle, however, a clearly distinguishable peak is present within the 95% confidence interval between 5 and 8 kyr.

Fig. 2.5 shows a comparison between the windowed reconstruction process (Fig 2.5a-f) and ridge extraction reconstruction process (Fig 2.5g-k). The spectra shown in Fig 2.5b include the typical 95% confidence interval; these intervals are commonly seen in the spectra obtained using the CWT. In Fig 2.5h, we omit the 95% confidence interval and instead indicate the most representative oscillatory modes identified by the ridge extraction process with red dashed lines.

Fig. 2.5. a) Synthetic data (blue) and superposition of reconstructed modes from windowed inverse SST (orange). b) SST of synthetic data showing individual search windows (cyan, magenta, green, and dark blue) for modes to be reconstructed. c) Reconstructed 0.5 kyr mode. d) Reconstructed 1 kyr mode. e) Reconstructed 1.5 kyr mode. f) Reconstructed 2.3 kyr mode. g) Synthetic data (blue) and superposition of reconstructed modes from ridge extraction inverse SST (orange). h) SST of synthetic data showing individual ridges identified (dashed red lines). i) Reconstruction of ridge 1. j) Reconstruction of ridge 2. k) Reconstruction of ridge 3.

The percentage of total amplitude recovered is calculated using the vector dot product between each reconstructed mode and the original time series; the windowed approach recovers 88% of the total amplitude with four windows each centered on the frequency of the modeled oscillation. In contrast, the ridge extraction process only

recovers 57% of the total amplitude with 3 modes, but requires a priori information regarding cyclicity. The reconstructed modes are stable for both methods with no discontinuities and have similar periodicity with the exception of the ridge extraction failing to model the 0.5 kyr oscillation.

By applying the same ISST reconstruction method to each real-data example, we reconstruct individual oscillations present in each record making a comparison between oscillations present in each record. Fig 2.6 shows the ISST reconstructions of the IRD time series (Bond et al., 1997) using both the windowed approach (Fig 2.6a-f) and ridge extraction method (Fig 2.6g-k). The windowed reconstruction is performed using four windows with periods of 0.5 kyr, 1 kyr, 1.5 kyr, and 2.3 kyr; accounting for 92% of the amplitude present in the record as shown in Fig 2.6a. The ridge extraction process identifies three distinct modes of oscillation, with periods that range from 0.5 kyr to 2.3 kyr and reconstructs 87% of the amplitude variation present in the IRD time series. The time series reconstruction using either approach provides an additional measure of confidence in the presence of these cycles, and provides precise indications of how these cycles change through time.
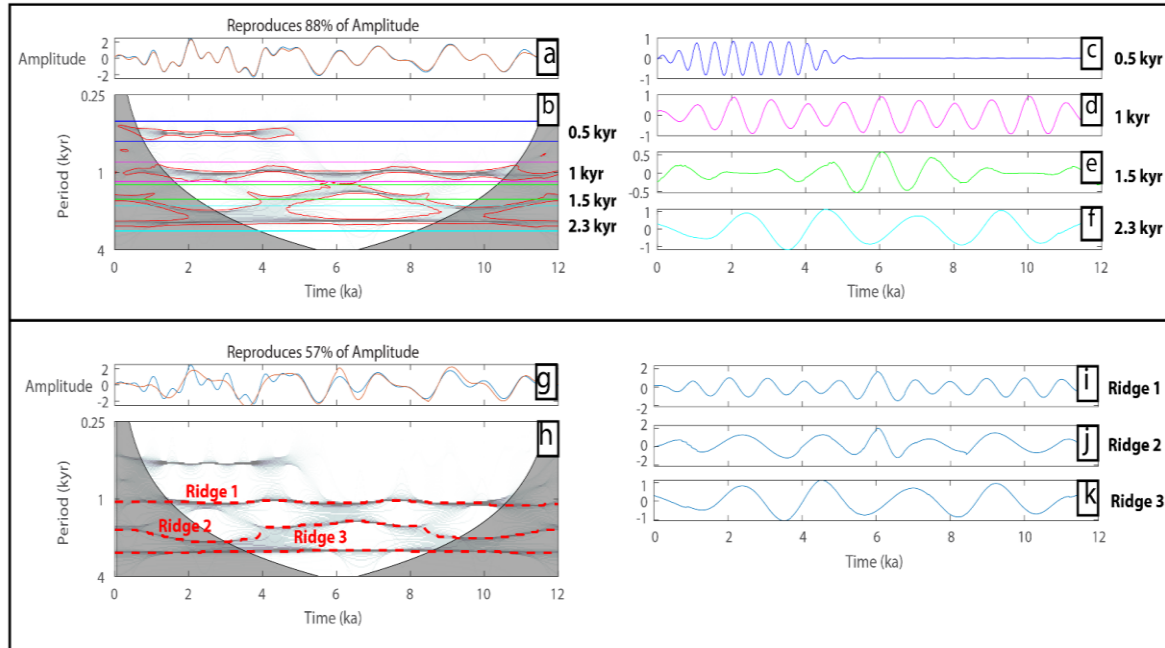
Fig. 2.6. a) Bond IRD data (blue) and superposition of reconstructed modes from windowed inverse SST (orange). b) SST of Bond IRD data showing individual search windows (cyan, magenta, green, and dark blue) for modes to be reconstructed. c) Reconstructed 0.5 kyr mode. d) Reconstructed 1 kyr mode. e) Reconstructed 1.5 kyr mode. f) Reconstructed 2.3 kyr mode. g) Bond IRD data (blue) and superposition of reconstructed modes from ridge extraction inverse SST (orange). h) SST of Bond IRD data showing individual ridges identified (dashed red lines). i) Reconstruction of ridge 1. j) Reconstruction of ridge 2. k) Reconstruction of ridge 3.

Applying the windowed ISST to the NGRIP $\delta^{18}O$ record (Fig 2.7a-f) reconstructs 72% of the amplitude variation, identifying a strong 0.5 kyr oscillation in the late Holocene, along with a 1 kyr oscillation in the early Holocene and a 2.3 kyr oscillation throughout the record. The ridge extraction ISST applied to the NGRIP record (Fig 2.7g-

k) favors shorter period cycles, reconstructing 79% of the amplitude variation using three modes, one of which, Ridge 1 in Fig 2.7i, has a period as short as 0.3 kyr. We include this identified mode in our discussion due to the strong amplitude of the oscillation and high resolution of the NGRIP record.
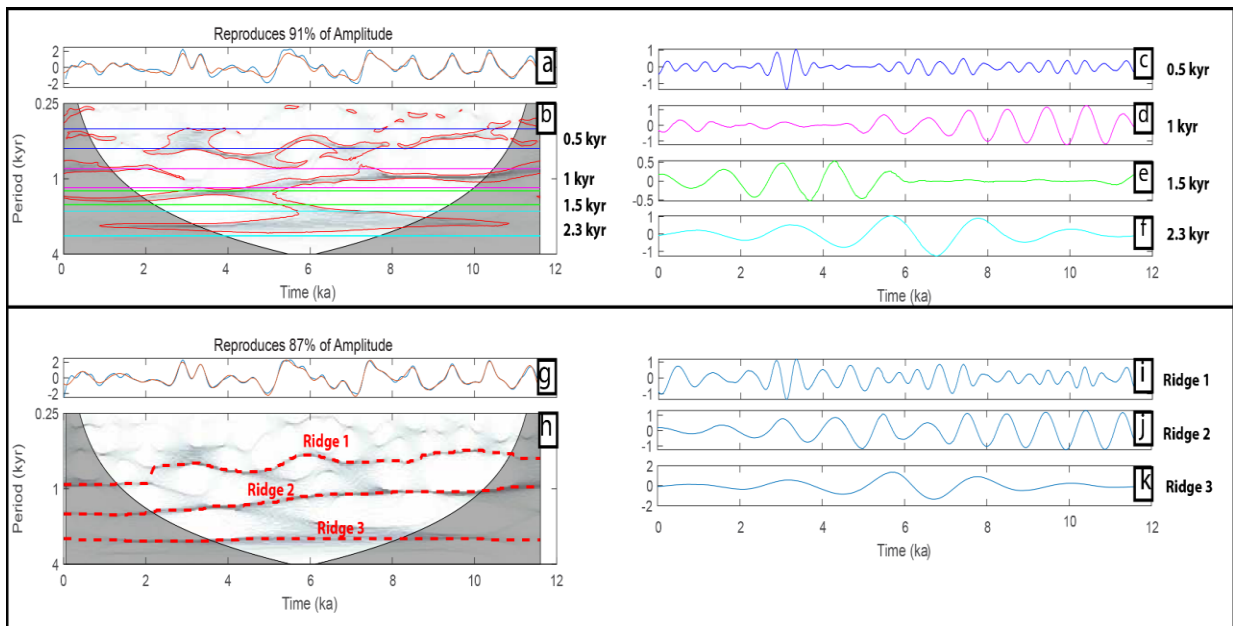

Fig. 2.7. a) NGRIP δ18O data (blue) and superposition of reconstructed modes from windowed inverse SST (orange). b) SST of NGRIP δ18O data showing individual search windows (cyan, magenta, green, and dark blue) for modes to be reconstructed. c) Reconstructed 0.5 kyr mode. d) Reconstructed 1 kyr mode. e) Reconstructed 1.5 kyr mode. f) Reconstructed 2.3 kyr mode. g) NGRIP δ18O data (blue) and superposition of reconstructed modes from ridge extraction inverse SST (orange). h) SST of NGRIP δ18O data showing individual ridges identified (dashed red lines). i) Reconstruction of ridge 1. j) Reconstruction of ridge 2. k) Reconstruction of ridge 3.

The windowed ISST applied to the Alaska BSi record reconstructs 83% of the amplitude variation while the ridge extraction process recovered 93%, and does so using three oscillatory modes. The windowed ISST provides an indication of an oscillatory mode with a period of 1.5 kyr between 3 ka and 7 ka (Fig 2.8e), this corresponds to the cessation of the 1 kyr cycle in Fig 2.8d. The ridge extraction process identifies three oscillatory modes, consisting of the 2.3 kyr oscillation observed in other records, along with one mode with a period of approximately 1 kyr through the record. The third identified mode, Ridge 1 in Fig 8i, has a discontinuity around 5.5 kyr where the period of oscillation increases from 0.5 kyr to ~1.5 kyr.
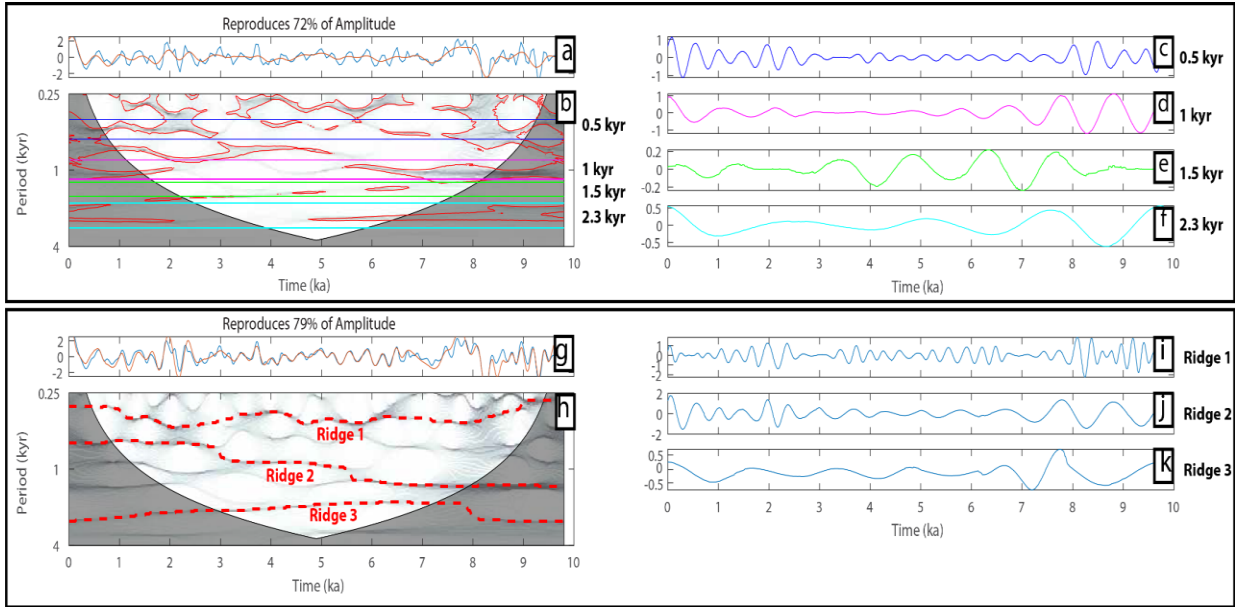

Fig. 2.8. a) Arolik Lake BSi data (blue) and superposition of reconstructed modes from windowed inverse SST (orange). b) SST of Arolik Lake BSi data showing individual search windows (cyan, magenta, green, and dark blue) for modes to be reconstructed. c) Reconstructed 0.5 kyr mode. d) Reconstructed 1 kyr mode. e) Reconstructed 1.5 kyr

mode. f) Reconstructed 2.3 kyr mode. g) Arolik Lake BSi data (blue) and superposition of reconstructed modes from ridge extraction inverse SST (orange). h) SST of Arolik Lake BSi data showing individual ridges identified (dashed red lines). i) Reconstruction of ridge 1. j) Reconstruction of ridge 2. k) Reconstruction of ridge 3.

Finally, the ISST is used to reconstruct oscillations present in the Victoria Island LOI time-series (Fig. 2.9). The windowed approach (Fig. 2.9a-f) does not show the same strong 0.5 kyr oscillation seen in other records, however, the ridge extraction method (Fig. 2.9g-k) identifies an oscillation with a period of 0.5-0.7 kyr (Ridge 1 in Fig. 2.9i). Both methods identify a 1.5 kyr oscillation, with the windowed approach showing this cycle in the early and late Holocene occurring simultaneously with a 1 kyr oscillation. Both methods reconstruct the longer 2.3 kyr oscillation nearly identically despite the differences between shorter oscillations.
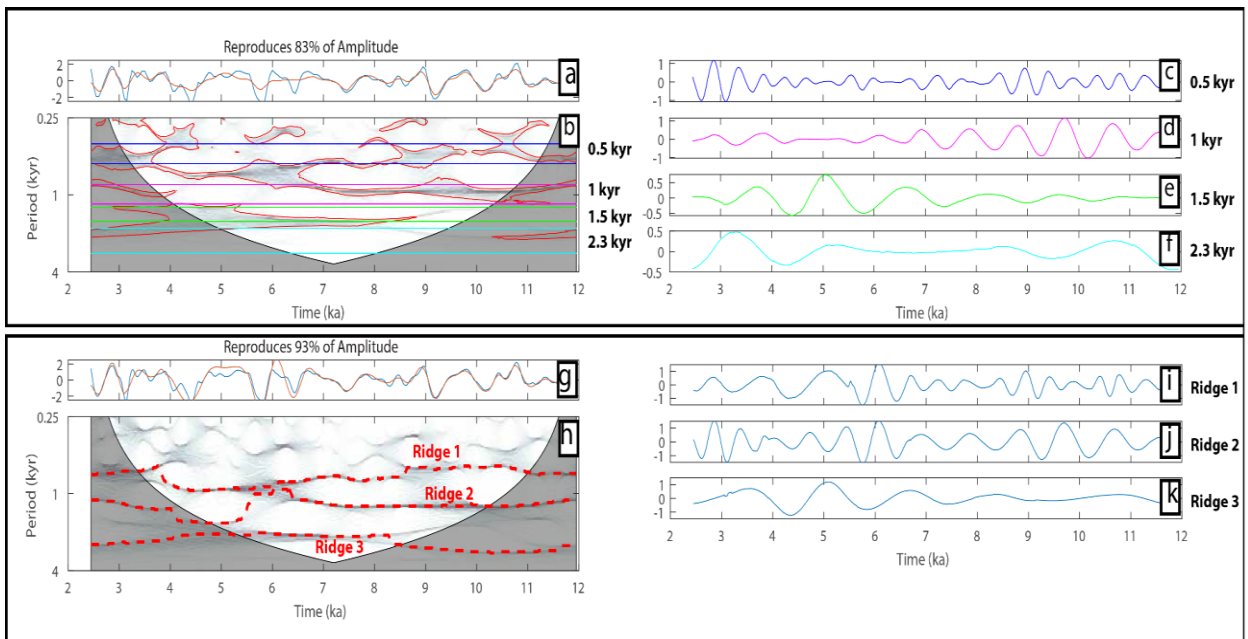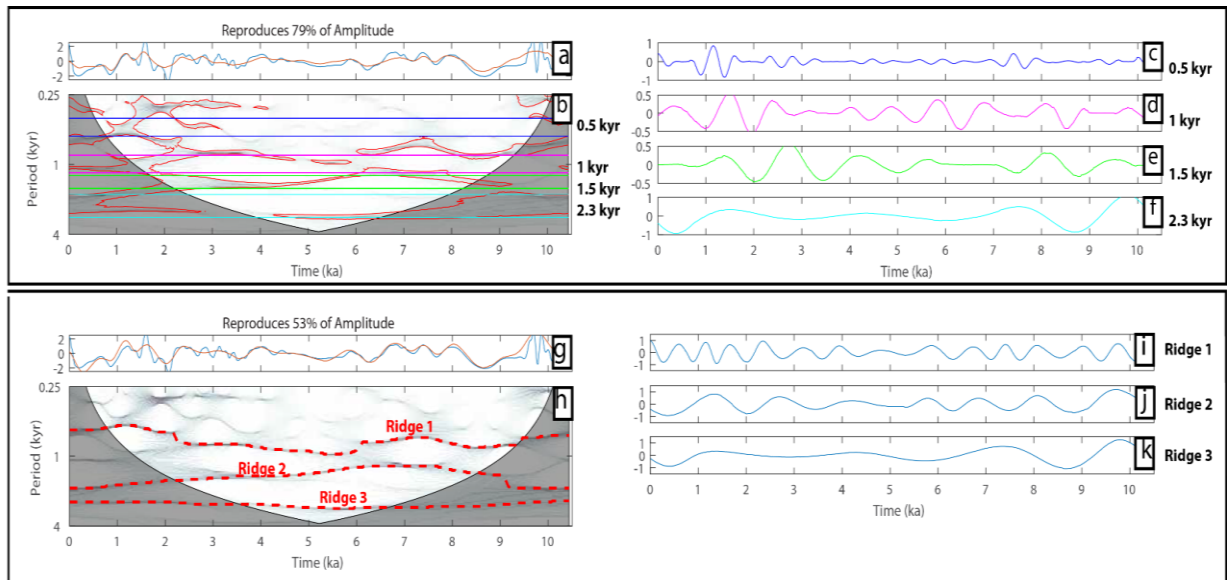
Fig. 2.9. a) Victoria island LOI data (blue) and superposition of reconstructed modes from windowed inverse SST (orange). b) SST of Victoria island LOI data showing individual search windows (cyan, magenta, green, and dark blue) for modes to be reconstructed. c) Reconstructed 0.5 kyr mode. d) Reconstructed 1 kyr mode. e) Reconstructed 1.5 kyr mode. f) Reconstructed 2.3 kyr mode. g) Victoria island LOI data (blue) and superposition of reconstructed modes from ridge extraction inverse SST (orange). h) SST of Victoria island LOI data showing individual ridges identified (dashed red lines). i) Reconstruction of ridge 1. j) Reconstruction of ridge 2. k) Reconstruction of ridge 3.

2.5 Discussion

There are a number of challenges related to spectral analysis of Holocene climate proxies, chief of these challenges is that the Holocene is a very short record length and certain cycles have an insufficient number of full oscillations observed. The criteria provided by Oppenheim and Schafer (1999) recommend that a minimum of five full oscillations should be observed, with ten or more full periods being ideal; this translates to cycles with a period shorter than 1.17 kyr as ideal for the Holocene, however, cycles as long as ~2.35 kyr are still trustworthy. In addition, the Holocene contains non-stationary signals, and limited resolution – all of which contribute to the differences in the interpretation of the 1 and 1.5 kyr cycles. Depending on the study area and analysis method used, results can also differ based on the advantages or shortcomings of the specific method utilized.

2.5.1 Synthetic Benchmark Data

By analyzing transforms and reconstructions of synthetic data with specific *t-f* inputs, we can better understand how these pitfalls affect our ability to distinguish cycles present in real data. We do this with the synthetic benchmark data using the normalized distance of each transform to quantify the reconstruction error. Fig. 2.10 a, b, and c show the reconstruction error of the STFT, CWT, and SST respectively, all with the wrap-around mask not applied; reconstruction errors are listed for each transform. Fig 2.10 d, e, and f show the same comparison, but with the mask applied to remove the wrap around effects that may be present, contributing to a higher reconstruction error. In the case of the SST, when the mask is applied, the reconstruction error is nearly a full order of magnitude lower than the same comparison without the mask. This indicates that the wrap around effects can introduce significant uncertainty in spectral estimates and interpretations should not be made outside the region. It is also apparent that the SST provides a significantly lower reconstruction error as compared to the STFT and CWT, this is due to the fact that the SST is very sparse and thus has a lower error when compared to a sparse input model.
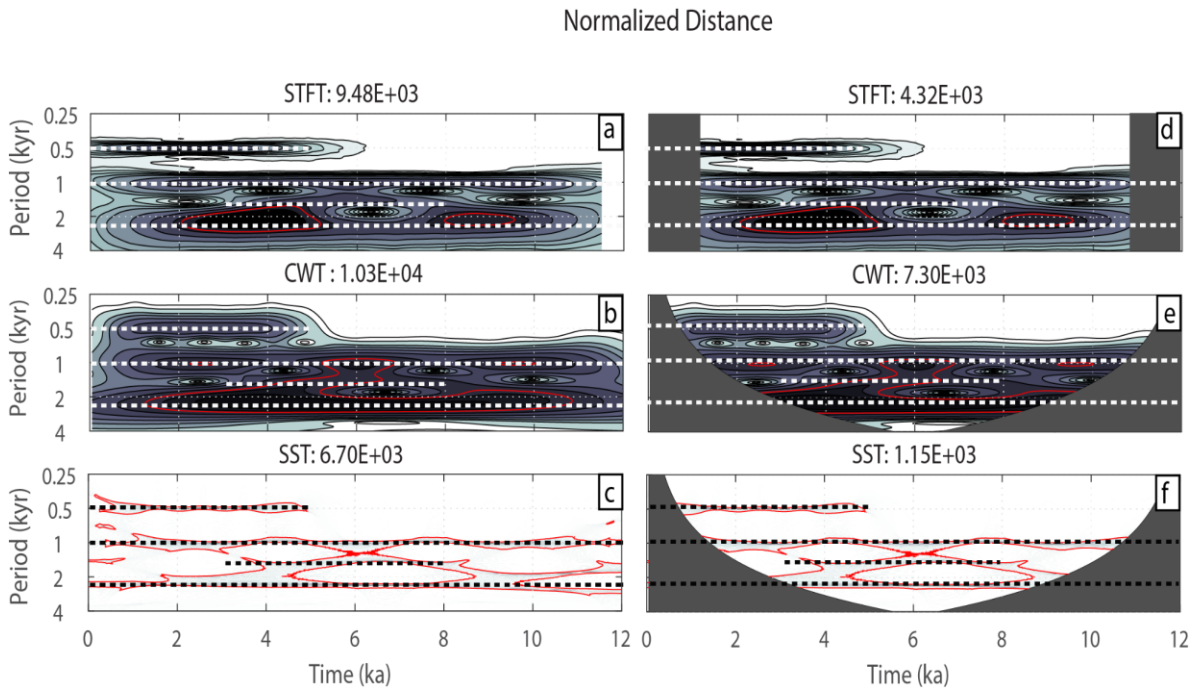
Fig. 2.10. a) STFT of synthetic data with input model overlaid (white). b) CWT of synthetic data with input model overlaid (white). c) SST of synthetic data with input model overlaid (black). d) STFT of synthetic data with input model overlaid (white) and mask applied to account for wrap around (grey). e) CWT of synthetic data with input model overlaid (white) and mask applied to account for wrap around (grey). f) SST of synthetic data with input model overlaid (black) and mask applied to account for wrap around (grey).

The inverse SST is used to assess how well the algorithm can recover specific oscillatory modes, particularly near the onset and cessation of the sporadic cycles. A perfect reconstruction would provide exactly the four signals input into the synthetic data, while no method could achieve an exact reconstruction, different approaches to

reconstructing specific modes could work better or worse depending on the nature of the oscillation.

The synthetic test example provides insight into how each reconstruction method performs in the presence of sporadic cycles (Fig 2.5). The windowed reconstruction provides a clear and precise indication of the onset and cessation of specific cycles, and recovers 88% of the amplitude variation in the data (Fig 2.5a). Subtle differences in amplitude can be observed between individual oscillations, particularly for the 1 kyr and 1.5 kyr cycles, however, the period of each oscillation matches the input model components well. The ridge extraction process does not perform as well (Fig 2.5g), accounting for 57% of the amplitude variation. This is primarily caused by the ridge extraction failing to reconstruct the sporadic 0.5 cycle. The ridge extraction process must identify a ridge present for the entire signal; if the ridge ends partway through the time series, the process will 'jump' to a different ridge; this characteristic is referred to as mode leakage (Bekara and van der Baan, 2009). The main benefit of the ridge extraction is that it requires no user inputs to identify the 1 kyr and/or 2.3 kyr cycles making this process particularly useful when the spectral makeup of a time series is unknown, which is usually the case in paleoclimate studies. For the sporadic signals, however, the ridge extraction breaks down when the cycle is not present; ridges corresponding to other oscillations are identified as being 'most representative' thus the reconstructions have abrupt discontinuities not seen using the windowed approach. In exploratory assessment of a record with unknown cyclicity, the ridge extraction could be advantageous, however, in most circumstances we have a reasonable idea of the frequency content we expect to

see. In cases like this, the advantages of the ridge extraction process may not be worth the trade offs in terms of mode leakage.

Conversely, we believe the field examples imply that the ridge-extraction-based reconstruction is more suitable for recognizing gradually changing characteristic periods within the time series, whereas the windowed reconstruction is favorable in case of more stationary frequencies as in the synthetic example. This can be seen in all field examples where the ridge-extraction often reconstructs the time series with an acceptable or higher correlation percentage, while using one mode less. We thus recommend applying both reconstruction techniques since the presence or absence of non-stationary periods has important implications for potential underlying physical processes. The reconstruction percentage provides an indication which scenario is more likely as highlighted next in the discussions on each individual example.

2.5.2 Spectral signatures in real data

As seen in Fig 2.11, spectral analysis performed on the IRD data (Bond et al., 1997) shows spectral peaks with periods or 1 kyr, 1.5 kyr and 2.3 kyr, these cycles were previously identified by Debret et al. (2007). The STFT (Fig 2.11a) mirrors the results of the CWT (Fig 2.11b) with some degree of spectral smearing present, especially apparent in the widening of the frequency peak for the 2.3 kyr cycle. The chief difference between the STFT and CWT is that in the CWT results, a 0.5 kyr peak is present above the 95% confidence level, while it is absent above this level in the STFT. The SST (Fig 2.11) dramatically reduced this spearing without introducing any leakage effects, thus providing improved localization of these cycles. Applying the SST, we note cycles with

periods of 0.5 kyr, and 2.3, along with one other cycle with a period of 1 kyr in the early Holocene transitioning to 1.5 kyr in the late Holocene. Our interpretation of this cycle differs from the interpretation made by Debret et al. (2007) using the CWT. The ISST reconstruction of the 1 kyr and 1.5 kyr cycles obtained using the windowed approach aligns with observations made by Debret et al. (2007) using the CWT, however, this result is achieved using windows that correspond to the periods identified in their analysis. The model that results from the ridge extraction does not include a separate '1.5 kyr' late Holocene period, but instead shows the 1 kyr oscillation period lengthening to 1.5 kyr in the late Holocene (Fig 2.6j).
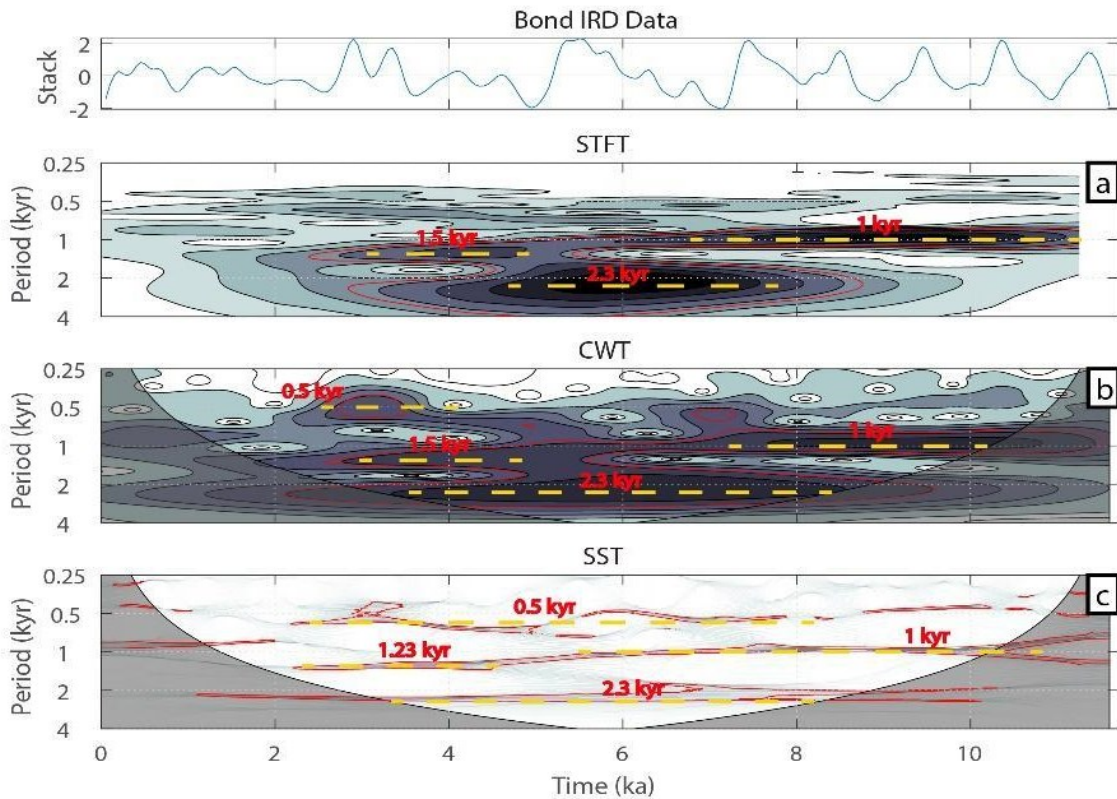
Fig. 2.11. IRD "Stack" data from the North Atlantic spectral analysis (Bond et al., (1997) showing a percentage of the petrologic tracers found in 3 deep-sea cores. a) STFT IRD data (window size 1.9 kyr, window overlap 1.8 kyr). b) CWT of IRD data (using a Morelt wavelet). c) SST of IRD data (using a Morlet wavelet and 32 voices).

The high resolution NGRIP ice core $\delta^{18}O$ record makes it more sensitive to shorter period cycles in both the STFT (Fig 2.12a) and CWT (Fig 2.12b); in the STFT, the temporal localization of these cycles is not as good as in the CWT, due to the fixed window length constraint. The benefit of the variable window width the CWT and SST use is evident in this example, where we see both identification of longer millennial cycles while simultaneously showing the temporal evolution of millennial cycles. Compared to both the STFT and CWT, the SST (Fig 2.12c) provides improved localization of the 1 kyr and 1.5 kyr cycle, showing a transition from a 1 kyr to 1.5 kyr period at approximately 6ka. Applying the ISST (Fig 2.7) using the windowed method shows a strong 1 kyr cycle in the early Holocene with a relatively weak 1.5 kyr cycle in the mid Holocene. The ridge extraction shows a cycle with a period of 1 kyr in the early Holocene shortening to 0.5 kyr in the late Holocene. The ridge extraction also detects one significant oscillation with a period of ~0.35 kyr (Fig 2.7i); this cycle has been previously identified in a solar activity record by Steinhilber et al. (2012). One possible reason this cycle is detected in the NGRIP record but not others discussed here is due to the higher sampling resolution of the NGRIP record, making it more sensitive to shorter oscillations.
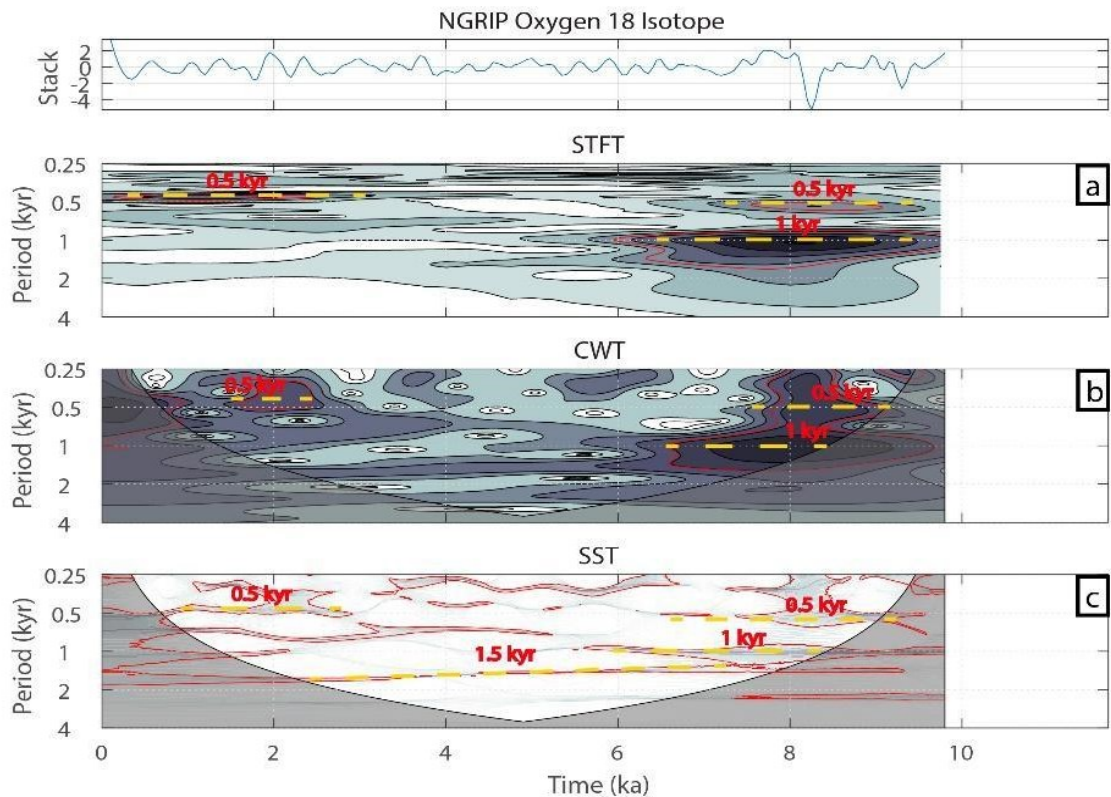
Fig. 2.12. NGRIP δ¹⁸O record spectral analysis (Anderson et al., 2004) between 10 ka and Present with taper applied to edges to reduce edge effects. a) STFT NGRIP δ¹⁸O record (window size 1.9 kyr, window overlap 1.8 kyr). b) CWT of NGRIP δ¹⁸O record (using a Morelt wavelet). c) SST of NGRIP δ¹⁸O record (using a Morlet wavelet and 32 voices).

The lacustrine BSi record (Hu et al., 2003) spectral analysis results show similar features across the STFT (Fig. 2.13a) and CWT (Fig 2.13b) with only subtle differences at the edges, apparent in other examples. Both of which show periods of 1 kyr in the early Holocene, 0.75 kyr in the middle Holocene, and 1.5 kyr in the middle-beginning of the late Holocene. Previously, Hu et al. (2013) analyzed this record using a Fourier

Transform, as a result, their frequency localization was very precise showing several distinct cycles (0.5 kyr, 0.75 kyr, 1 kyr, and some indication of 1.5 kyr), however, they provide no information regarding the temporal evolution of their record. The SST (Fig 2.13c) shows additional detail surrounding all of these cycles, and primarily shows how the cycle with a period of 1 kyr in the early Holocene shortens to a period of 0.75 kyr, at which point the cycle with a period of 1.5 kyr becomes visible. The inverse SST results from the windowed analysis (Fig 2.8a-f) reproduce 83% of the amplitude of the lacustrine record, while the ridge extraction method (Fig 2.8g-k) reproduces 93% of the amplitude, however, it is clear that the periodicity of the extracted ridges (Fig 2.8i-k) vary quite dramatically and abruptly as compared to the modes reconstructed with the windowed method (Fig 2.8c-f). The reconstructed 1.5 kyr (Fig 2.8e) oscillation in this record is a lower amplitude than the 1 kyr (Fig 2.8d), however, a clear transition is seen in the mid-Holocene where the amplitude of the 1.5 kyr oscillation increases while the 1 kyr oscillation amplitude decreases.
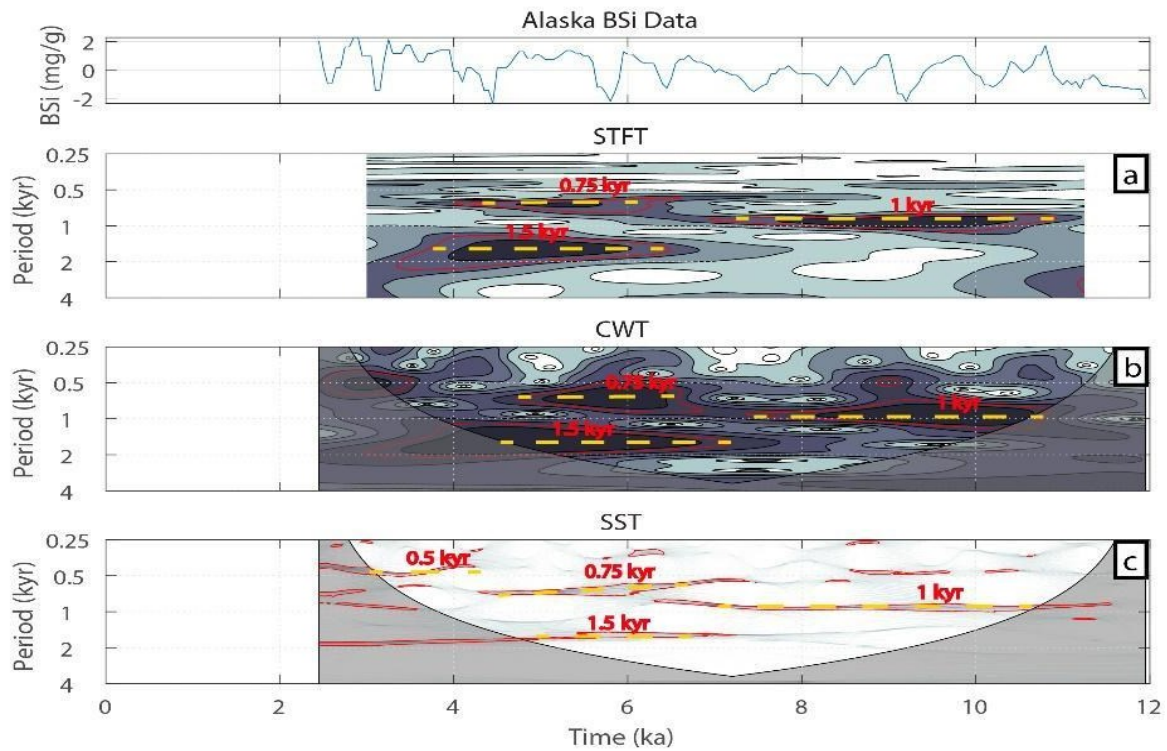
Fig. 2.13. Arolik lake Biogenic Silica record spectral analysis (Hu et al., 2003) a) STFT of Alaska BSi record. (window size 2 kyr, window overlap 1.9 kyr). b) CWT of Arolik lake Biogenic Silica record (using a Morelt wavelet). c) SST of Arolik lake Biogenic Silica record (using a Morlet wavelet and 32 voices).

Spectral analysis of the Victoria Island loss on combustion record is difficult due to the strong trend present in the data. Even after removing the trend, the STFT (Fig 2.14a) and CWT (Fig 2.14b) do not reveal a great deal regarding the spectral makeup of the record; some indication of a 1-1.5 kyr oscillation is present in the late Holocene, however, a large amount of smearing is present. Upon examination of the SST (Fig 2.14c) a more clear indication of this oscillation is seen with a period of 1.5 kyr during both the early and late Holocene. The ISST does not perform as well in this example,

reproducing 79% of the overall amplitude with the windowed method and 53% using the ridge extraction. This is primarily caused by two sporadic, high frequency events at ~9.5 ka and ~1.75 ka are not taken into account by these methods. In this case, the energy is captured in the t-f transform (Fig. 2.9b and Fig. 2.9h), however, we have not prescribed windows short enough to reconstruct this type of variability as we focus on millennial-scale variability. The windowed method shows clear distinction between the 1 kyr (Fig. 2.9d) and 1.5 kyr (Fig. 2.9e) oscillation, and does show the 1.5 kyr oscillation to be more evident in the late Holocene. The reconstructed ridges show one oscillation with a cycle that has period ranging between 0.75 kyr and 0.5 kyr through the entire record, as well as another cycle with a period of 1 kyr in the early Holocene, transitioning to a period of 1.5 kyr in the late Holocene; this transition occurs between 3-5 ka.
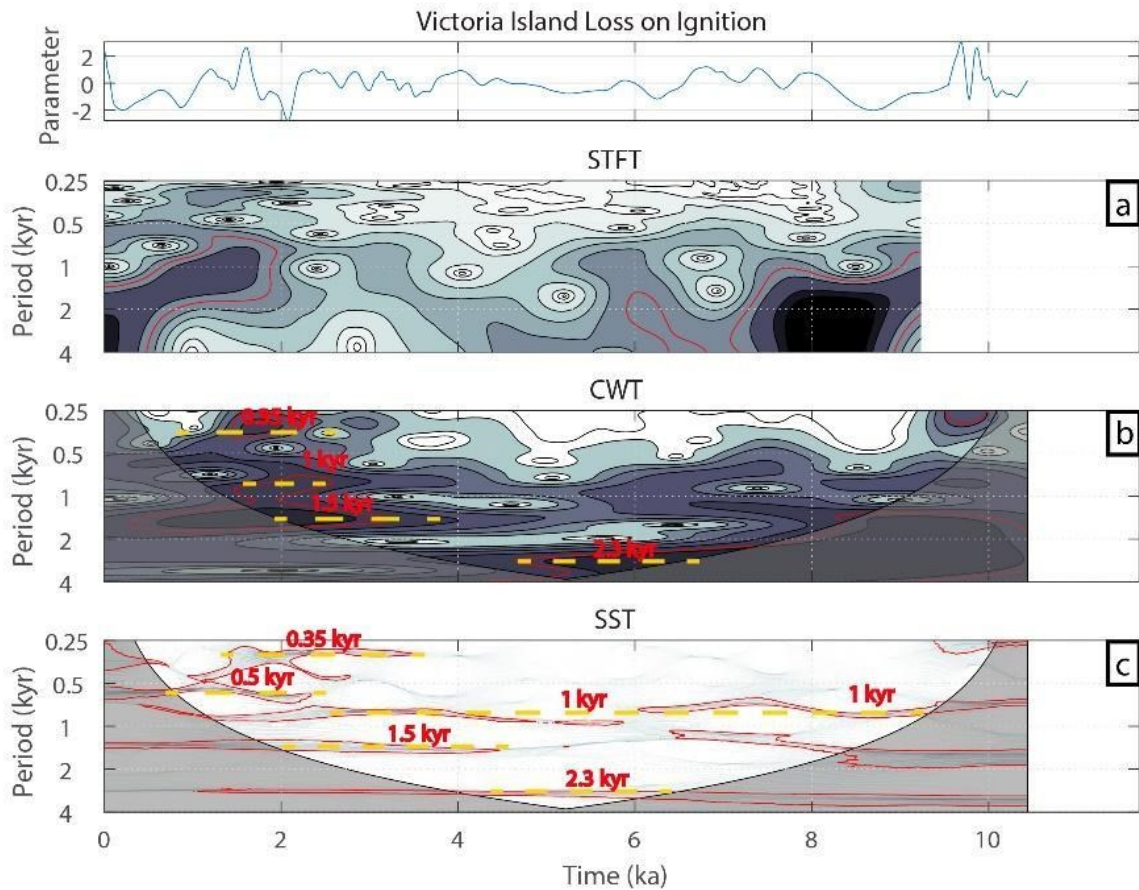
Fig. 2.14. Victoria Island LOI record spectral analysis (Peros and Gajewski, 2008). a) STFT of Victoria Island LOI record. (window size 2 kyr, window overlap 1.9 kyr). b) CWT of Victoria Island LOI record (using a Morelt wavelet). c) SST of Victoria Island LOI record (using a Morlet wavelet and 32 voices).

Results of the ISST for each of the records analyzed are compiled into Table 2.1 to provide a simple and effective comparison of periodicity, onset and cessation of commonly observed Holocene cycles. As described in Table 2.1, the presence of the 1.5 kyr cycle coincides with the cessation of the 1 kyr cycle present in the remainder of the record; this transition occurs between 6 and 8 ka, depending on the proxy analyzed. This

47

timing lines up with the Mid-Holocene transition observed by Debret et al. (2009) in North-Atlantic and circum-Antarctic records where internal forcing begins to dominate and solar forcing has less of an impact on climate oscillations. This would suggest the 1.5 kyr oscillation is driven by an internal forcing mechanism related to ocean water circulation and is not astronomical; our results using this technique reinforce this hypothesis made by Debret et al. (2009) and Sorrel et al. (2012). Reconstruction of solar activity using [10]Be as a proxy, such as a record developed by Steinhilber et al. (2012), shows similar periodicities described in Table 1. The spectral analysis of their record did not extend past periods longer than 1 kyr, however, their results show a 0.5 kyr cycle between 8-5 ka and 3-1 ka, the occurrence of these cycles in the solar activity matching the observations in Table 1 using the ISST confirms the solar origin of the 0.5 kyr climate oscillation. Spectral analysis of the solar activity proxy also shows the 1 kyr solar eddy cycle present between 9-4 ka and absent from 4 ka to the present day, this also aligns with the timing observed using the ISST.

Sorrel et al. (2012) note that this 1.5 kyr cycle intensifying corresponds to a slowing of sea-level rise and cessation of meltwater input and rule-out solar forcing as the primary trigger of millennial scale Holocene storminess maxima. The 2.3 kyr oscillation is present in all four records, however, due to the short duration of the records and a relatively long period of the 2.3 kyr cycle, the majority of this cycle is seen outside the COI where wraparound effects could contribute to uncertainty in the period and timing of the cycle. We also note a common onset of the 0.5 kyr cycle in the late Holocene, at around 0.5-4 ka for each proxy analyzed using the inverse SST. By reconstructing individual oscillatory modes using this process, we observe details in the records such as

the relative amplitude of a given oscillation; details that may otherwise be overlooked when performing Wavelet Analysis (Debret et al., 2009) or fitting mono-chromatic cosine oscillations (Sorrel et al., 2012). Table 2.1 serves as a short example of a much more exhaustive comparison that could be performed using the ISST methods described in this text. This example comparison illustrates the effectiveness of the ISST in determining the exact time of onset or cessation of a climate cycle, and allows better unification of climate cyclicity within a given region.

Table 2.1 Table summarizing cyclical oscillations identified in each time series analyzed using the ISST method

Proxy	Region	0.5 kyr	1 kyr	1.5 kyr	2.3 kyr
Bond IRD	North Atlantic	0.5-4 ka 6-10 ka	5-11 ka	1-6 ka	4-11 ka*
NGRIP $\delta^{18}O$	North Atlantic	0.5-3 ka 7-9 ka	5-10 ka	2-8 ka	2-10 ka*
Alaska BSi	Northern Alaska	0.5-2 ka 6-9 ka	5-9 ka	1-5 ka	6-9 ka*
Victoria Island	Northeast Canada	0.5-4 ka 7-8 ka	4-9 ka	2-6 ka	2-10 ka*

* Outside cone of influence where wrap around effects have a significant influence

2.6 Conclusions

Synthetic benchmarks show the SST to be the best performing method in terms of frequency localization ability when signals are separated by less than one octave; this makes the SST especially suitable when analyzing Holocene proxies. Additionally, using synthetic data, we note that the presence of intermittent cycles (either the cycle of interest or other cycles) can dramatically increase spectral smearing and make interpreting the 1.5 kyr cycle particularly challenging. Reconstructing individual modes using the ISST approach(s) we demonstrate here is particularly useful to achieve a more accurate representation of the exact periodicity of specific climate oscillations, as well as a more precise indication of the temporal onset and cessation of these oscillations. Using this method, we analyze four Northern Hemisphere paleoclimate proxies and observe a number of consistencies in the behavior of millennial scale Holocene climate oscillations, and in the distribution and timing of the mid-Holocene transition. We also observe sporadic sub-millennial climate oscillations distributed across the Northern Hemisphere with consistent timing for the onset and cessation. While this is far from a full review of Northern Hemisphere Holocene paleoclimate proxies, we are able to make a more unified interpretation of the nature of millennial climate oscillations with just a handful of selected proxies. This leads us to recommend the ISST approach presented here be applied on a larger scale, where all available Northern Hemisphere Holocene proxies are re-evaluated to determine a precise representation of the geographic distribution and temporal occurrence of millennial and sub-millennial climate oscillations through the Holocene.

3. Deciphering of sedimentary cycles in the Chinese eolian red clays as obliquity driven

3.1 Introduction

Milankovitch cycles have been recorded and documented in several ice core oxygen isotope records representing a marine environment (Lorius et al., 1985; Jouzel, 1987; Petit et al., 1999) and various proxies in continental settings (Evans et al., 1991; Williams et al., 1997; Heslop et al., 2002; Kravchinsky et al., 2003; Anwar et al., 2015; Qin et al., 2022). The Chinese red clay directly underlies the loess-paleosol deposits of the Chinese Loess Plateau reflecting a continuous record of sedimentation and preserved continental climate conditions during the Pliocene. These deposits have received considerable attention over the past ~30 years with several studies demonstrating preserved eccentricity cycles (Evans et al., 1991; Sun et al., 2006; Gylesjö and Arnold, 2006; Anwar et al., 2015; Nie, 2018; Qin et al., 2022). Shorter period obliquity and

precession cycles have yet to be shown in the red clay due to age model constraints and inadequate sampling rates. Only one study noted an indication of obliquity in their records (Anwar et al., 2015), however, this indication fell outside their spectral analysis confidence intervals.

The primary obstacle in showing obliquity and precession in any record is converting section depth in the development of an accurate age model which provides the time basis for the paleoclimate time series. In the Chinese red clay deposit, the absence of fossils, and other age markers adds additional complexity to this process, leaving magnetic measurements the only way to determine section age. This has been done by a number of authors at the same section in Shilou County, Shaanxi, China, both using magnetostratigraphy alone by Ao et al., (2016; 2018; 2021) or using magnetostratigraphy supplemented by cyclostratigraphy such as the technique used by Anwar et al. (2015). Cyclostratigraphy involves using cycles observed in measurements as additional age constraints in the age model development; this results in a more accurate age model than visual correlation alone could provide. In the study of Anwar et al. (2015), only the eccentricity cycles were used in the cyclostratigraphy portion of their analysis since obliquity and precession were not observed due to 20-cm spaced sample collection which did not satisfy the Nyquist criterion for the shorter Milankovitch periodicities. Observation of the precession and obliquity cycles would not only help in determination of sedimentation rates of the red clay in the Chinese Loess Plateau, but also improve our understanding of how orbital forced climate cycles behave in continental settings and how climate fluctuations influence sedimentation. Kravchinsky et al. (2003) studied the

6.7 Myr Lake Baikal record and demonstrated that ~ 40 kyr obliquity cycles are supposed to be present in the long continental records of the same age interval as the red clay.

This work aims to demonstrate the existence of the obliquity cycles in the Chinese red clay deposit, and assess the relative strength of these cycles compared to the previously identified eccentricity cycles. This will be accomplished through the collection of high-resolution samples to sufficiently sample the higher frequency obliquity and precession cycles without introducing aliasing into the paleoclimate record. Sampling intervals are determined using sedimentation rate models developed for this section by Anwar et al. (2015), areas which show a higher rate of sedimentation will be sampled with a smaller interval, the deepest part of the section will also be sampled at a smaller interval due to increased compaction decreasing temporal resolution. The age model from Anwar et al. (2015) will serve as a preliminary chronology for the section and magnetic susceptibility measurements of the high-resolution samples will be used to develop a new paleoclimate time series. The time series will then be tuned to eccentricity cycles where subtle stretching/shortening is applied such that susceptibility peaks align with eccentricity maxima. Spectral analysis will be performed using the inverse SST algorithm which has been applied to Holocene paleoclimate proxies by Borowiecki et al. (2023); the time-series reconstruction this process produces will be used to determine if the short period oscillations present in the record correspond to Milankovitch periodicities but also used to evaluate the relative strength of these cycles compared to the previously identified 400 kyr and 100 kyr eccentricity cycles.

3.2 Geologic Setting

The Chinese loess and red clay deposit is separated into three distinct sequences; the uppermost sequence being a loess/paleosol sequence from 0-2.6 Ma; and the remaining two sequences being red clay (Evans et al., 1991; Anwar et al., 2015; Nie et al., 2016). Within the red clay deposit, two different sequences are typically observed with a division at ~7 Ma between the upper red clays and lower deposits (Hao and Guo, 2007; Nie et al. 2016). The lower red clay sequence is only accessible in certain geographic locations in the western part of the Chinese Loess Plateau (CLP) with depositional ages from 7-22 Ma (Hao and Guo, 2007). There is some degree of ambiguity surrounding the depositional environment of the oldest sequence (7-22 Ma), with some evidence suggesting the sediment is aeolian but influenced by fluvial processes (Hao and Guo, 2007; Alonso-Zarza et al., 2009). The deposition of the first two sequences (0-7 Ma) is generally accepted to be aeolian with little to no evidence of alteration from fluvial processes (Sun et al., 1998; An et al., 2001). The transition from mixed aeolian and fluvial influence to only aeolian coincides with a major phase of the Himalaya-Tibetan plateau uplift, and is interpreted as a response to the initiation of this uplift (An et al., 2001).

The aeolian red clay sediment has experienced pedogenesis and oxidation to a varying extent, resulting in magnetic mineralogy alteration and alternating bands of

carbonate rich and depleted red clays, making this section a very good record of continental climate cyclicity. The magnetic mineral alteration taking place in the overlying loess through pedogenesis has been shown to result in maghemite in the most highly altered soil horizons regardless of the original magnetic mineralogy in the deposits due to its chemical stability (Heller and Evans, 1995). A later study by Nie et al. (2007) observed this same phenomena in the Chinese red clays, and noted a linear correlation between low frequency magnetic susceptibility and magnetic susceptibility frequency dependence (FD).

High frequency (HF), low frequency (LF), and frequency dependence (FD) magnetic susceptibility measurements are commonly used as paleoclimate proxies for the Chinese Loess Plateau (Evans et al., 1991; Heller and Evans, 1995; Nie et al., 2007; Anwar et al., 2015), with a number of studies demonstrating the clear existence of orbital eccentricity cycles preserved in the red clays (Evans et al., 1991; Sun et al., 2006; Gylesjö and Arnold, 2006; Anwar et al., 2015; Nie, 2018). One such example is the Shilou section [37.1°N, 110.7°E] which is located approximately 15 km northwest of Shilou County in the west of Shanxi province, China and is surrounded by the Lüliang Mountains to the east and the Yellow River to the west. Fig. 3.1 illustrates the location of the Shilou section which has been discussed in numerous studies recently.
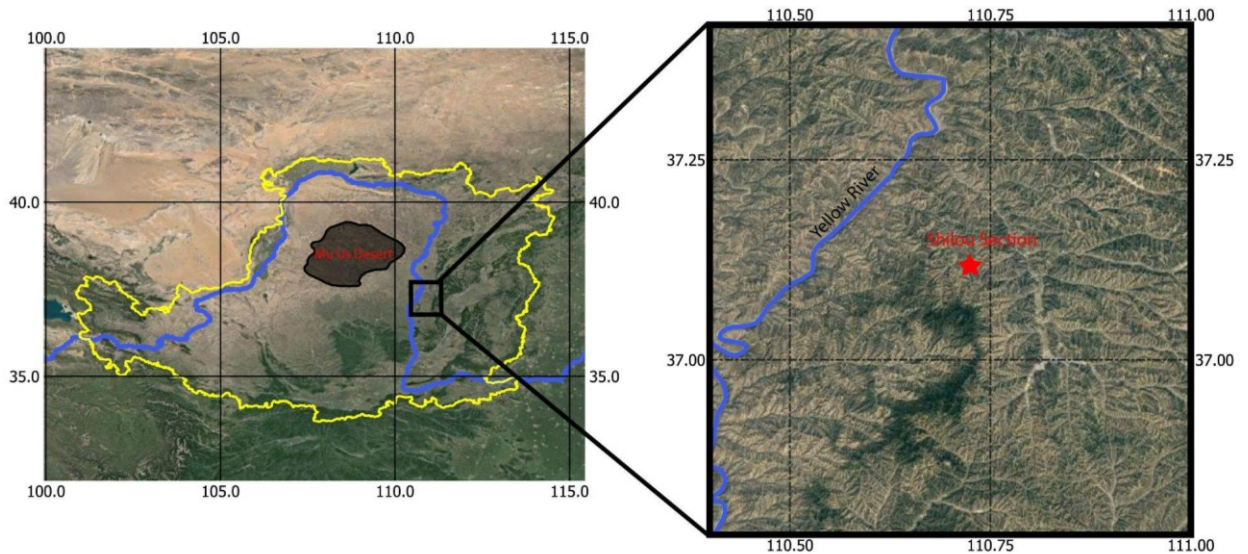
Fig. 3.1. Geographic location of the Shilou section showing the full extent of the Chinese Loess Plateau (yellow polygon).

The Shilou section is a 68 m continuous outcrop of alternating bands of carbonate rich and carbonate depleted red clay which spans approximately 2.5 million years; from 2.58 Ma at the Neogene-Quaternary boundary to ~5.2 Ma with Quaternary brown loess overlying the red clay (Anwar et al., 2015). Fig. 3.2 shows the Shilou section with Quaternary light brown loess overlying the Neogene red clay, and bands of carbonate rich horizons clearly visible at the outcrop scale.

Fig. 3.2. Photo of the Shilou section showing the Quaternary loess (light brown) overlaying the Mio-Pliocene red clay deposit. Alternating bands of carbonate rich and carbonate depleted soil horizons visible at outcrop scale. Reconstructed obliquity (black) overlaid to demonstrate period of oscillations.

3.3 Methods

3.3.1 Sampling and Measurements

In the sedimentation rate model developed by Anwar et al. (2015), the lowest sedimentation rate modeled was 1 cm/kyr, however, the majority of the Shilou section

was deposited at a rate closer to 2 cm/kyr. For our analysis, powder samples were collected at a 5 cm interval, this interval corresponds to a temporal resolution of 2.5-5 kyr depending on the section depth. Sampling started 5.85m above the transition from Loess/brown soil to red clay, this transition signifies the Quaternary/Neogene boundary. This will ensure the Nyquist criterion is satisfied and a sufficient number of samples to observe precession cycles with a period of ~20 kyr. Powder samples were crushed to a grain size less than 1 mm and packed into 10 ml plastic containers. Low Frequency (LF) and High Frequency (HF) magnetic susceptibility were measured for each sample using a Bartington MS2B magnetic susceptibility meter, LF measurements are conducted at 470 Hz and HF measurements are conducted at a 1:10 ratio (4700 Hz). All measurements were performed in the Paleomagnetic Laboratory of the University of Alberta. The Frequency Dependence (FD) parameter was calculated from the LF and HF measurements using eq 3.1; corrections were applied prior to calculation FD to account for magnetic susceptibility contributions from the container.

$$X_{FD} \% = 100 * ((X_{LF} - X_{HF}) / X_{LF}), \qquad (3.1)$$

Where X_{FD} is the frequency dependence parameter (as a percentage), X_{LF} is the low frequency susceptibility, and X_{HF} is the high frequency susceptibility.

When collecting samples, the section lithology was classified into categories based on the extent of pedogenic alteration during and after deposition; this classification is done visually and reflects the amount of carbonate present at a given depth. These

classifications are assigned a numerical value from 1 to 4 in order to allow for spectral analysis to be performed on the apparent lithologic variations in the section in addition to the magnetic susceptibility measurements. The assigned lithology categories consist of 1 - clean red clay, 2 - red clay with sparse carbonate nodules, 3 - red clay with carbonate nodules, and 4 - carbonate rich red clay. Fig 3.3 shows the LF and HF magnetic susceptibility (3.3a, 3.3b) and FD (3.3c) plotted vs. depth with a lithology fill to allow comparison between susceptibility fluctuations and lithologic variations. These alternating bands of carbonate right red clay and clean red clay have been observed in the past (Xu et al., 2009; Anwar et al., 2015), however, unlike variations in magnetic susceptibility; they have not been shown to correspond with any paleoclimate oscillations driven by eccentricity. For our analysis, we focus on performing a detailed analysis on only the LF susceptibility data as the HF and FD record(s) closely mirror the LF record with a similar response to changes in soil type. The Quaternary/Neogene boundary (2.588 Ma, 5.85m depth) is indicated in Fig. 3.3, this boundary serves as the reference datum for comparing samples from previous studies such as Anwar et al. (2015).
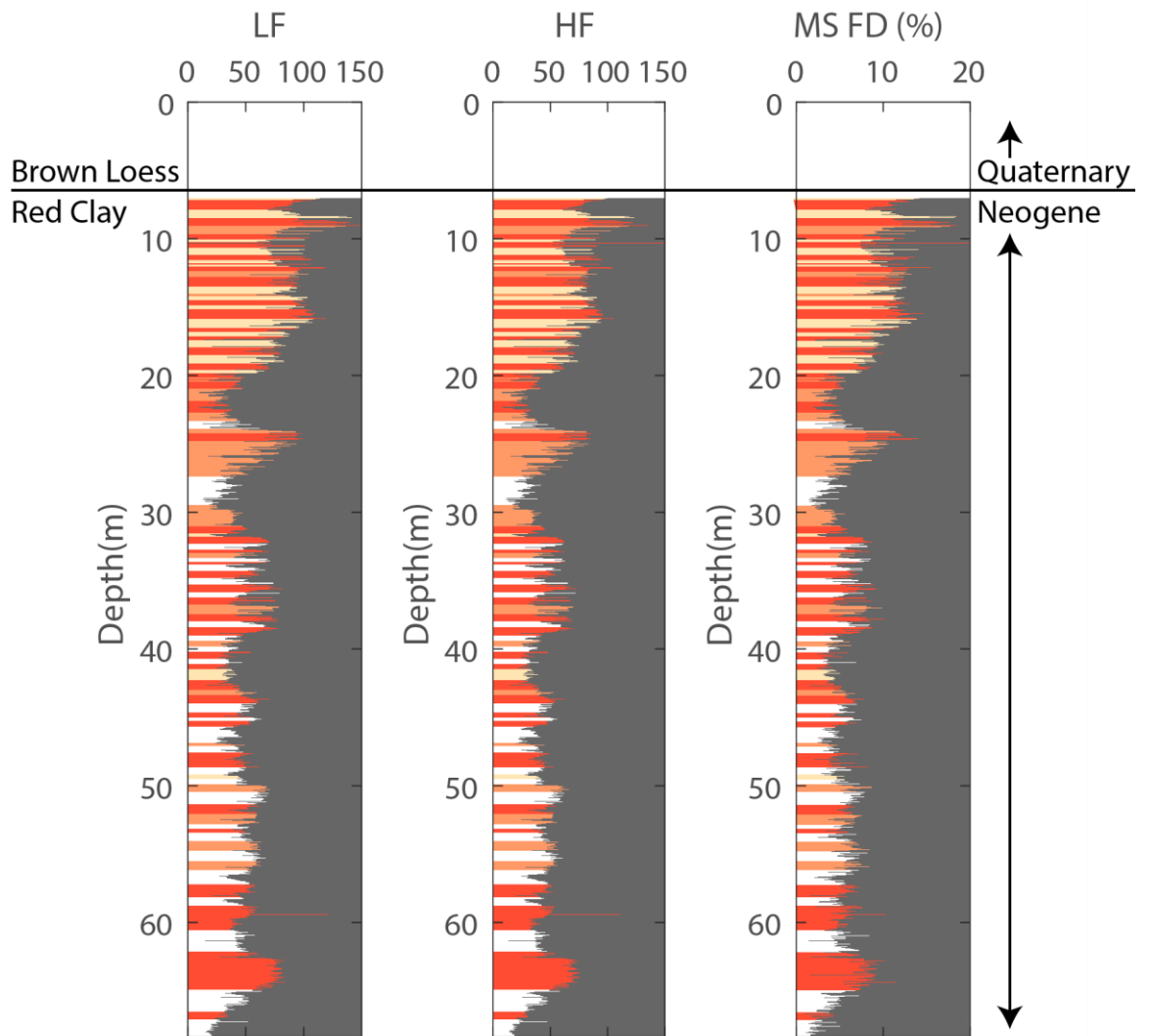
Fig. 3.3. a) Low frequency susceptibility vs depth. b) high frequency susceptibility vs depth. c) calculated FD vs depth. Lithology fill corresponds to: 1 - clean red clay, 2 - red clay with sparse carbonate nodules, 3 - red clay with carbonate nodules, and 4 - carbonate rich red clay.

3.3.2 Age Model

We use the age model developed by Anwar et al. (2015); this age model was developed on the same section with samples collected at the same datum, so this age model can be easily applied to our high-resolution MS records. Visual correlation between our high resolution MS record and the record published by Anwar et al. (2015) is performed by matching up peaks between the two records. This step is performed using the program AnalySeries developed by Paillard et al. (1996) which provides useful outputs such as sedimentation rate in addition to shifting a target record to match a reference. The age is extracted at depth points identified in Anwar's record, and used as age markers for our new high-resolution record. Linear interpolation is performed between age markers, and a preliminary age model for the new records is determined. Since the two sets of samples measure across the Quaternary/Neogene boundary, the transition from Loess/brown soil to red clays is used as a reference datum to align the sample depths between records and serves as the starting point of the age model (5.88 Ma).

Manual orbital tuning is used to further improve the age model for the section. This process requires identifying reference curves, and making small incremental adjustments to the dated magnetic susceptibility record, and performing a linear interpolation between correlated events in the reference curve and the high resolution susceptibility and lithology records. The AnalySeries software (Paillard et al., 1996) is used once again to complete this, with a numerical solution for orbital eccentricity developed by Laskar et al. (2004). Manual orbital tuning is utilized over automated

methods such as the Dynamic Time Warping (DTW) algorithm (Herrera et al., 2014) as it permits user input into specific constraints, providing more control over age model adjustments. The DTW algorithm works by iteratively applying a stretch to a target record to maximizing the correlation coefficient between the target and reference. The method works well for records that are of similar resolution, however, with the resolution difference between the MS record from Anwar et al. (2015) and the record presented here, the method tends to apply extreme stretches to some cycles and extreme compressions to others. Fig. 3.4 shows the high-resolution MS time series (Fig 3.4a) and FD time series (Fig 3.4b) in addition to the revised age model (Fig 3.4c) and sedimentation rate model (Fig 3.4d) following the completion of orbital tuning.
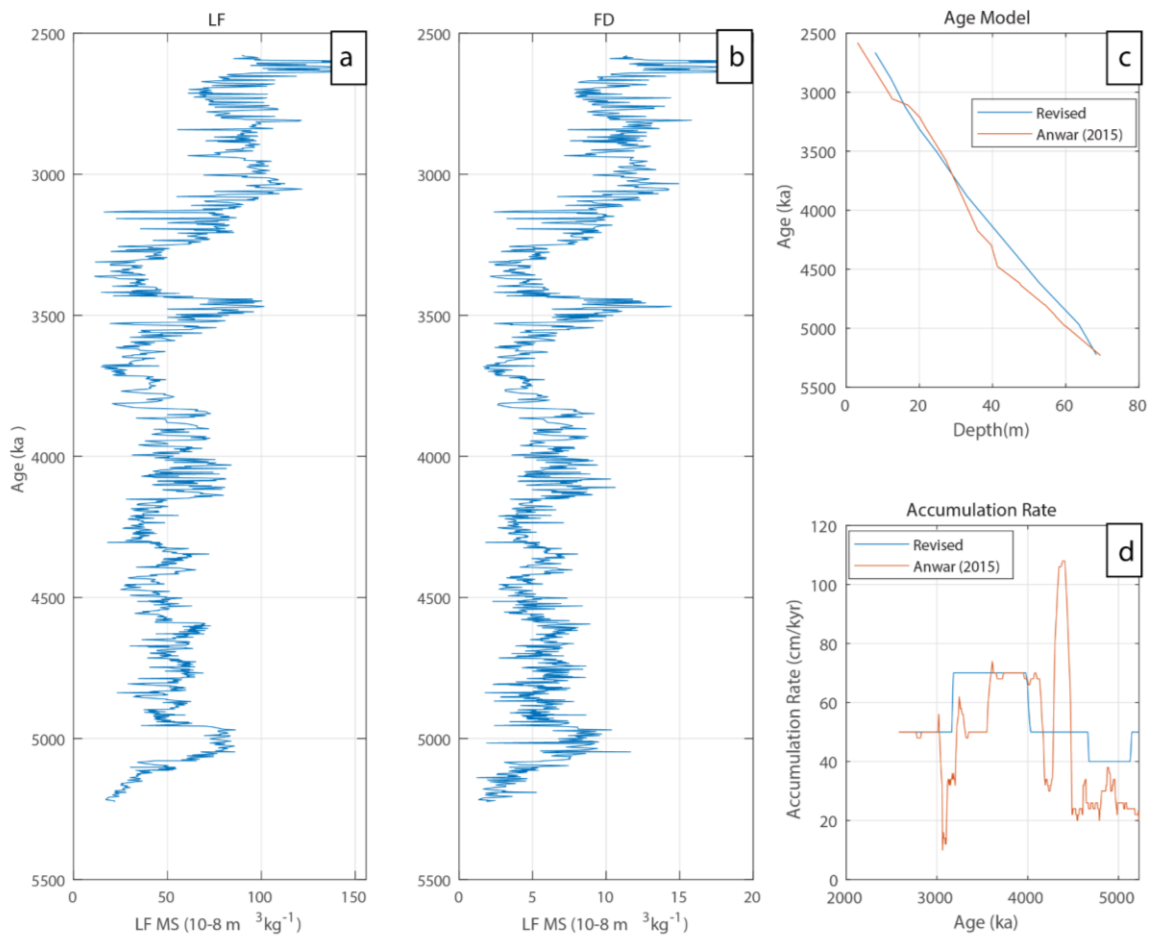
Fig. 3.4. a) Low frequency susceptibility vs time. b) calculated FD vs time. c) Age model revised from Anwar et al. (2015) to account for orbital tuning. d) Sedimentation rate revised from Anwar et al. (2015) to reflect changes from orbital tuning.

3.3.3 Spectral Analysis

Spectral analysis is performed on the high-resolution MS time series using the Inverse Synchrosqueezing Transform (ISST) algorithm proposed by Borowiecki et al. (2023). This approach provides many benefits over methods such as the Continuous

Wavelet Transform; primarily that the SST is a sparse transform which allows for improved separation between cycles that are separated by less than one octave in the frequency domain. In addition, the ISST allows for the reconstruction of individual oscillations, which is not only beneficial when examining the temporal occurrence of sporadic cycles but also in comparing the relative amplitude of one oscillation to another. Two different reconstruction algorithms can be used, either an automatic ridge extraction which identifies and reconstructs the most representative oscillatory modes in the *t-f* transform, or a windowed method which takes user input and reconstructs oscillations present within a predefined window. As outlined by Borowiecki et al. (2023) each approach has advantages and shortcomings depending on the situation it is used in, and it is often most useful to apply both methods and make interpretations on the results together.

Confidence intervals are calculated for the SST and obtained through injection of randomly simulated red noise into the data prior to calculating a *t-f* transform. Signal to noise ratio is set to 3:1 and 100 realizations (*t-f* transforms). The resulting transforms are combined and energy is normalized, the 95% confidence interval is drawn around the area that the 0.95 contour in the red noise intersects the normalized energy in the *t-f* transform for each time step.

3.4 Results

Spectral analysis is performed on the LF susceptibility record following orbital tuning to investigate relationships that may exist between the high frequency variability

present in the MS measurements and the orbital reconstruction developed by Laskar et al. (2004). The analysis on LF susceptibility is presented here, as after performing the analysis on susceptibility FD, the results were very similar with no additional information provided by the FD record. Our spectral analysis is performed using the Inverse SST algorithm proposed by Borowiecki et al. (2023). We apply this analysis to a time series that has not been detrended, and to one that has been detrended. To detrend the LF susceptibility record, we fit a spline to the the data using the built-in Matlab function 'smooth' using a loess regression smoothing function in Matlab to fit the high amplitude, long period oscillations present in the data and remove it from our time series to improve our reconstructions of the short period oscillations present in the MS record. These oscillations correspond to the 400 kyr eccentricity cycle; if left in the record, they would dominate the amplitude of the transform in the t-f domain.

For each of the unfiltered and detrended records, we use both a windowed ISST with windows set to known astronomical periodicities (100 kyr, 40 kyr, and 20 kyr), and an automated ridge extraction process which identifies and reconstructs the most representative periodicities present in the spectra. We include an additional window with a period of 173 kyr, as this periodicity has been observed in a number of red clay deposits, and is associated with orbital interactions between Earth and Saturn (Zhang et al., 2022). To determine window widths for each astronomical period, we apply the SST to a solar insolation reconstruction at a latitude of 37° N, corresponding to the approximate latitude of the Shilou section (Fig 3.5).
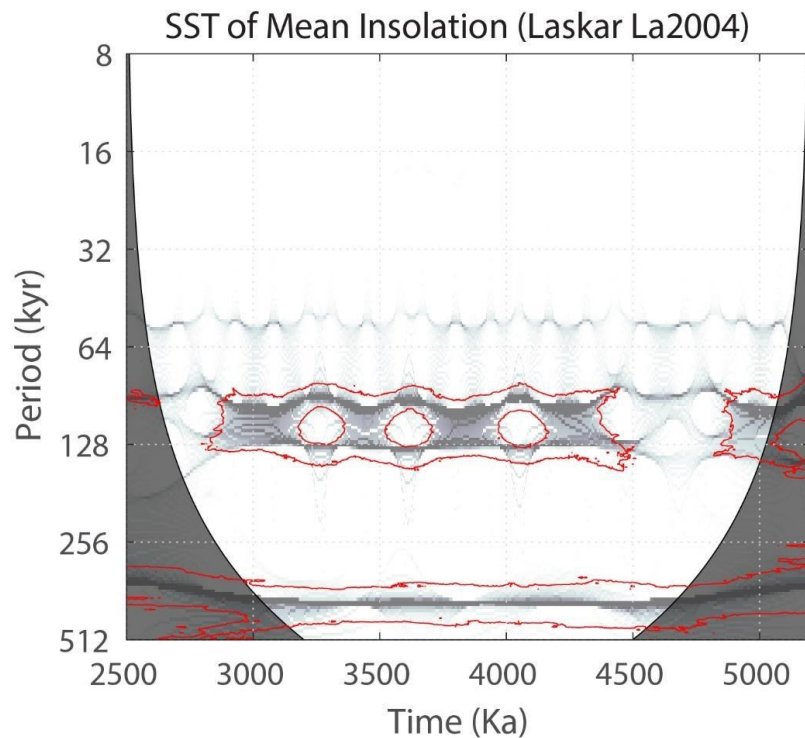
Fig. 3.5. SST of isolation reconstructed using Laskar et al. (2004); solution for latitude of Shilou section (37ºN).

Fig. 3.6 shows the results of this analysis for the unfiltered LF susceptibility record; the SST is calculated using a Morlet wavelet for periods between 8 kyr and 512 kyr. We omit calculating and displaying the 95% confidence interval contour for the ridge extraction (Fig. 3.6h) in order to highlight the ridges identified by the algorithm, however, for the windowed method (Fig 3.6b) we include this contour. An oscillation in the 173 kyr window is reconstructed, starting approximately 4000 ka and continuing to 2600 ka (Fig 3.6f). This oscillation has lower amplitude than the other reconstructed modes, however, it is significant enough to be detected and reconstructed by the ride extraction as well (Fig 3.6l). The ridge extraction process reconstructs oscillations

between 32 kyr and 256 kyr, without detecting short-period oscillations present for the entire record. The ridge extraction also reconstructed a cycle with a period between 60 and 70 kyr; this cycle has been previously identified by Kravchinsky et al. (2003) in lacustrine sediment, and by Zhang et al. (2022) in red clay deposits. While this periodicity does not directly correspond to an orbital cycle, Rial and Anaclerio (2000) suggest that it is likely to be a frequency modulation generated sideband of the 41 kyr obliquity cycle.

Fig. 3.6. a) Unfiltered LF susceptibility data (blue) and superposition of reconstructed modes from windowed inverse SST (orange). b) SST of unfiltered LF susceptibility data
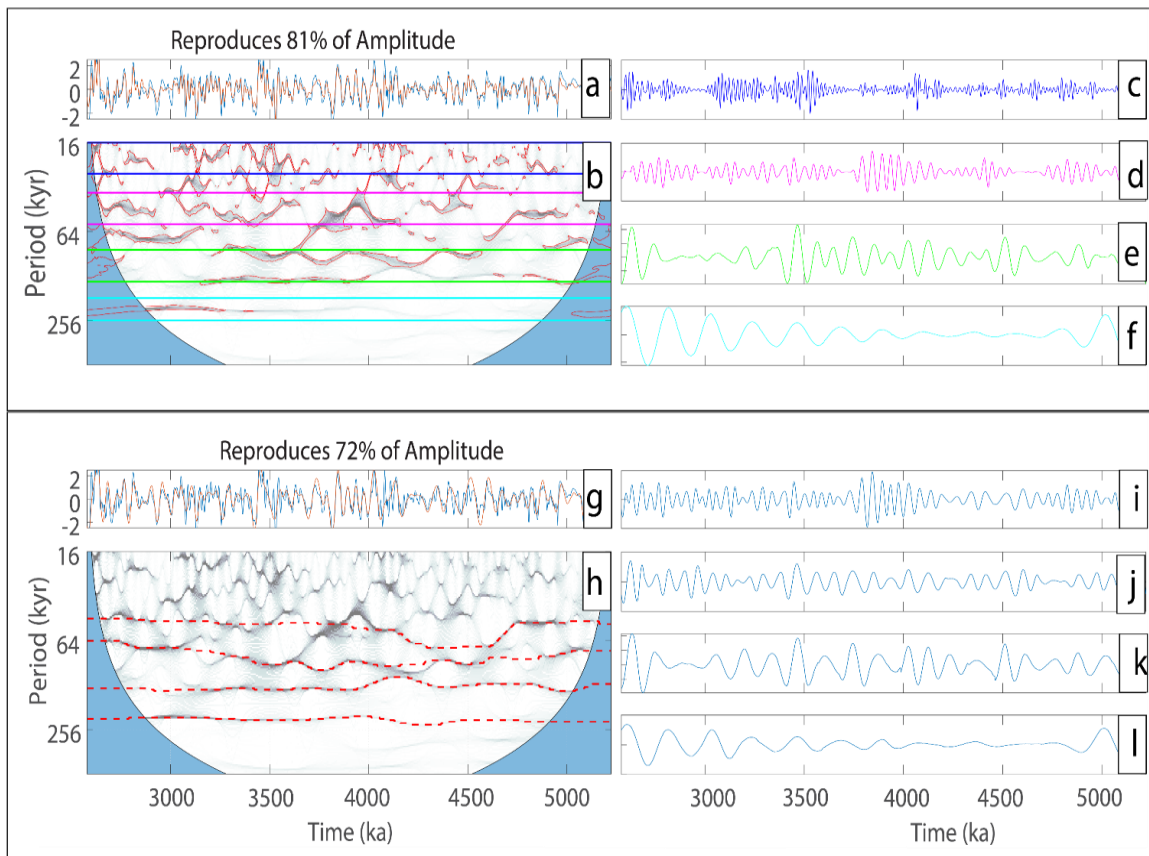
showing individual search windows (cyan, magenta, green, and dark blue) for modes to be reconstructed. c) Reconstructed 20 kyr mode. d) Reconstructed 40 kyr mode. e) Reconstructed 100 kyr mode. f) Reconstructed 173 kyr mode. g) Unfiltered LF susceptibility data (blue) and superposition of reconstructed modes from ridge extraction inverse SST (orange). h) SST of unfiltered LF susceptibility data showing individual ridges identified (dashed red lines). i) Reconstruction of ridge 1. j) Reconstruction of ridge 2. k) Reconstruction of ridge 3. l) Reconstruction of ridge 4.

Fig. 3.7 shows the same analysis applied to the filtered LF susceptibility record. In this case, the 173 kyr window reconstructs an oscillation with a 173 kyr period (Fig 3.7f), however, the amplitude of this oscillation is much lower than in the unfiltered record. In addition, the ridge extraction does not reconstruct this 173 kyr oscillation as seen when looking at the detected ridges in Fig 3.7h as compared to Fig. 3.6h where this oscillation is detected and reconstructed. With the majority of the long period oscillation(s) removed from the record, 76% of the MS record amplitude is reconstructed using windows and 56% using the ridge extraction. Both the windows and ridge extraction reconstruct an oscillation (Fig 3.7d and Fig 3.7i respectively) with a period that ranges from approximately 50 kyr in the early part of the record to approximately 35 kyr in the later half. Similar to the unfiltered record, the ridge extraction does not reconstruct any short period oscillations, however, the windowed reconstruction does. The short-period oscillation reconstructed by the windowed method (Fig 3.7c) is sporadic, and most pronounced in the later part of the time series, from 3500 ka to 2600 ka.

Fig. 3.7. a) Filtered LF susceptibility data (blue) and superposition of reconstructed modes from windowed inverse SST (orange). b) SST of Filtered LF susceptibility data showing individual search windows (cyan, magenta, green, and dark blue) for modes to be reconstructed. c) Reconstructed 20 kyr mode. d) Reconstructed 40 kyr mode. e) Recons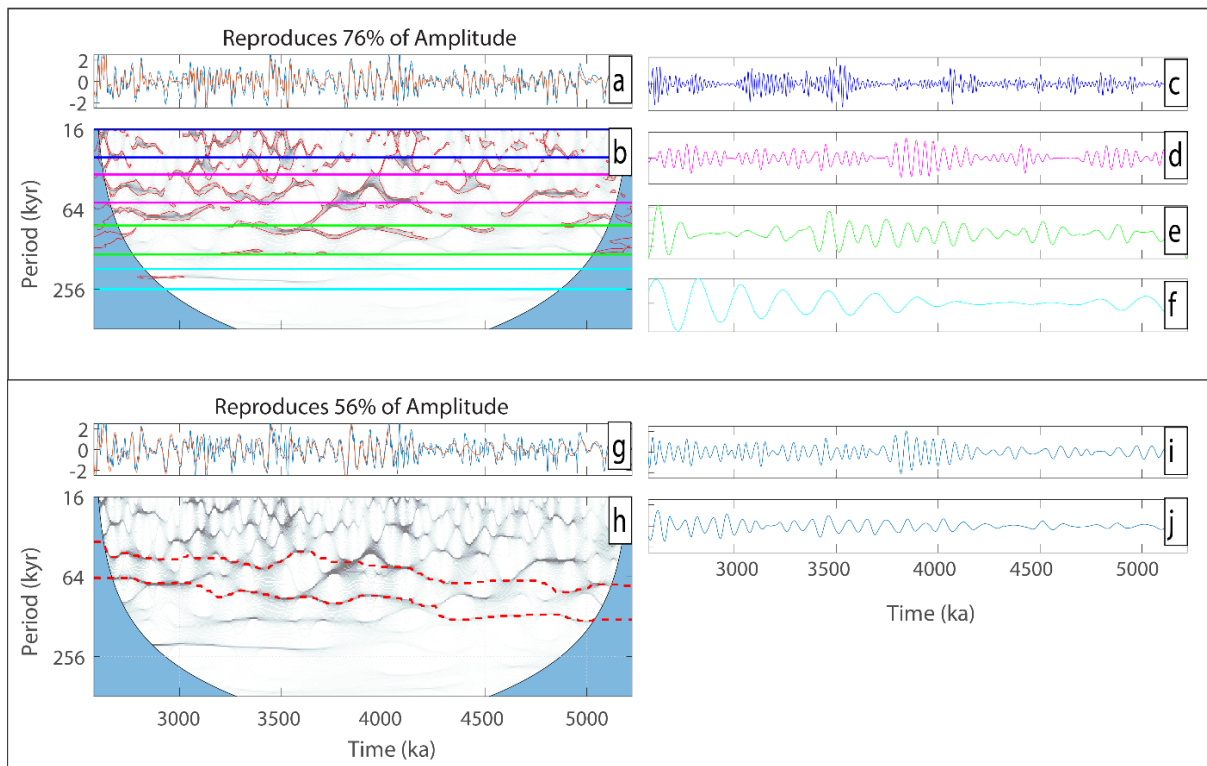tructed 100 kyr mode. f) Reconstructed 173 kyr mode. g) Filtered LF susceptibility data (blue) and superposition of reconstructed modes from ridge extraction inverse SST (orange). h) SST of filtered LF susceptibility data showing individual ridges identified (dashed red lines). i) Reconstruction of ridge 1. j) Reconstruction of ridge 2.

3.5 Discussion

The oscillations reconstructed using the inverse SST allow us to analyze individual cycles present in the MS record, and calculate the relative amount of amplitude each oscillatory mode contributes to the overall amplitude of the record. The windowed reconstruction of the unfiltered MS record shows strong amplitude oscillations with periods of 173 kyr (Fig 3.6f, Fig 3.6l), and 100 kyr (Fig 3.6e, Fig 3.6j), these oscillations correspond to the eccentricity cycles previously demonstrated by others in these deposits (Evans et al., 1991; Sun et al., 2006; Gylesjö and Arnold, 2006; Anwar et al., 2015; Nie, 2018; Zhang et al., 2022). We also observe a consistent oscillation with higher frequency than either of the eccentricity oscillations (Fig 3.6d, Fig 3.6i). Both reconstructions of this oscillation behave similarly in the time domain, with the strongest amplitude present between 3400 and 4500 ka - this oscillation has a period ranging between 50 kyr and 35 kyr, with the majority of the energy focused around 40 kyr which aligns very closely with orbital obliquity (Laskar et al., 2004). The windowed reconstruction also captures additional short-period oscillations the ridge extraction did not capture (Fig. 3.7c); these oscillations are sporadic and have periods between 16 kyr and 25 kyr which matches multiple orbital precession harmonics (Rial and Anaclerio; 2000) The windowed reconstruction of the unfiltered record reproduces 81% of the total amplitude variation present in the LF susceptibility record with windows set to major known astronomical periodicities.

Applying aggressive detrending to the record removes the majority of the 173 kyr eccentricity cycle, however, the trend fit to the record keeps the other eccentricity cycles

with periods of 128 kyr and 100 kyr present with amplitude similar to the record that has no trend removal applied. The short period oscillations reconstructed by the windowed method are very similar to the reconstructions with the trend removed and the ridge extraction process does not identify any oscillations shorter than 32 kyr present for the entire record. The ridge extraction does not perform well in this test as compared to the windowed method as it is unable to capture any of the short period variability due to the sporadic nature of it in the record. This is especially pronounced in the early part of the record, from 4000 ka to 5300 ka where the reconstruction (Fig 3.7g) does not match well with the LF susceptibility record.

For both the windowed and ridge extraction techniques, the reconstruction reflects a lower amount of the total amplitude for the detrended record as opposed to the unfiltered record. While the orbital obliquity and precession are present in the record, the spectral analysis does not perform as well reproducing it as it does with the longer period oscillations. This is most likely caused by the eccentricity being more easily recorded without aliasing as compared to obliquity and precession which are more difficult to sample at a sufficiently high frequency to avoid aliasing. While orbital precession cycles are not sporadic, the reconstructed 20 kyr time series corresponding to precession *is* sporadic. This could be caused by numerous factors including sampling resolution limitations, age model uncertainty, and post-depositional processes taking place that can erase these cycles in certain intervals (Nie et al., 2004; Anwar et al., 2015; Ao et al. 2018)

We use the orbital solution developed by Laskar et al. (2004) to compare the short-period oscillations reconstructed from the LF susceptibility record to an analytic record of orbital obliquity and precession. This is useful in comparing not just the relative

amplitude of reconstructed climate oscillations but also to further investigate phase differences between the orbital solution and the reconstructed oscillations; a phase lag could indicate a delayed climatic response to external forcing or minute age model inaccuracies. Fig 3.8 shows the comparison between the obliquity reconstructed using the solution from Laskar et al. (2004) and one mode reconstructed with the Inverse SST applied to the LF MS record. The timing and phase of each peak/trough cycle between the obliquity reconstruction from Laskar et al. (2004) and the oscillations recovered by the Inverse SST of the detrended MS record are in good agreement for the majority of record. It is unlikely any systematic phase large exists between obliquity and the 40 kyr climate oscillation driven by obliquity, instead, it is more likely the phase lag observed in Fig 3.8 is caused by small inaccuracies in the age model; these inaccuracies could be improved by tuning the MS record to obliquity prior to performing spectral analysis.
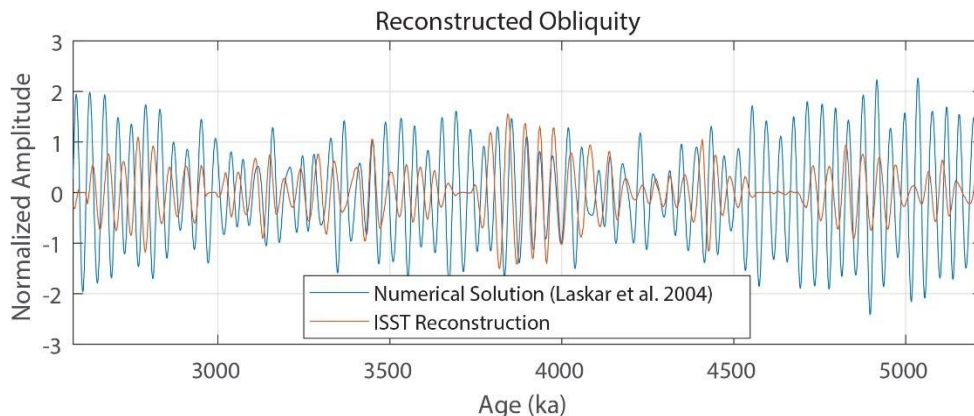

Fig. 3.8 Comparison of numerical obliquity solution (blue) as calculated by Laskar et al. (2004) and reconstructed 40 kyr oscillation extracted from high resolution Shilou LF susceptibility record (orange).

Discrepancies in amplitude exist between 4500-5300 ka, and there is a particularly good agreement in normalized amplitude between 3400-4500 ka. There are a number of reasons that amplitude discrepancies may exist between the orbital reconstruction and cycles preserved in the magnetic susceptibility record, chiefly secondary alteration of magnetic mineralogy producing varying concentrations of maghemite for each soil horizon (Nie et al., 2007). This indicates that the cycle recovered by the Inverse SST of the detrended MS record may be driven by obliquity between 3400 and 4500 Ka, but that the magnetic minerals present in the red clay have experienced some degree of secondary alteration as suggested by Nie et al. (2007).

3.6 Conclusions

The Miocene/Pliocene Chinese red clay deposits are sensitive to variations in continental climate on timescales that are representative of orbital cycles, however, there are a number of difficulties present in reconstructing a paleoclimate time series from these records. The lack of accurate age markers in the succession dictates cyclostratigraphy and magnetostratigraphy should be used together to develop an accurate model, a technique used by Anwar et al. (2015). With an accurate age model, resolution becomes the primary concern, with a high frequency sample interval necessary to uncover shorter period orbital cycles (obliquity and precession). Using the age model developed by Anwar et al. (2015), the high-resolution samples collected from the Shilou

section are accurately dated, and only subtle changes are applied to the timing of individual Eccentricity following the orbital tuning process described in their work.

Spectral analysis was performed on the Shilou MS time series using the Inverse Synchrosqueezing Transform technique previously applied to Holocene paleoclimate time series by Borowiecki et al. (2023). This technique reconstructs individual oscillations in the time domain based on input periodicities for windows or using a ridge extraction technique which identifies the most representative oscillation in the *t-f* domain and reconstructs the amplitude along those ridges. In addition to eccentricity cycles previously identified by numerous studies including Evans et al. (1991), Anwar et al. (2015), Nie, (2018), Qin et al. (2022), we identify multiple shorted period oscillations present in the high-resolution record. One of which corresponds to the ~40 kyr period of orbital obliquity. To further investigate how well this cycle corresponds to obliquity, we compare this oscillation in the time domain to a numerical reconstruction of obliquity developed by Laskar et al. (2004). Upon comparison, we notice similarities in the phase and period of these two time-series, however, note some discrepancies in amplitude between the two records.

A number of hypotheses could explain amplitude discrepancies of individual oscillations including modulation of obliquity signal by orbital eccentricity as suggested by Rial and Anaclerio (2000), or secondary alternation of magnetic minerals as described by Nie et al. (2007). Agreement of normalized amplitude, period, and phase observed in the interval 3400-4500 Ka between the reconstructed climate oscillation and orbital

obliquity solution lead us to conclude that the oscillations between carbonate rich/depleted soil horizons are Obliquity driven during this period. Outside this interval agreement between the obliquity solution and reconstructed 40 kyr oscillation is not as strong suggesting a different forcing mechanism was dominant during that time.

4. Last Glacial Maxima

4.1 Introduction

Centennial to millennial scale climate oscillations in the Holocene Epoch, the current interglacial period, have been reported on continents and in the ocean in each climate zone and extensively reviewed (Soon *et al.,* 2014; Marsicek *et al.,* 2018; Wanner *et al.,* 2018). Observed Holocene temperature fluctuations have amplitudes greater than 1°C (McMichael, 2012). Meanwhile, the centennial scale climate variability remains poorly identified during the Last Glacial Maximum (LGM), defined between ~ 26.5 and 20 ka in Clark *et al*. (2009), because the data typically lack sufficient temporal resolution. To address this, our study analyzes a high resolution continental climate record between ~ 26 and 20.6 ka during the LGM, when ice sheets were at their maximum extent as a result of reduced northern summer insolation, tropical Pacific sea surface temperatures, and atmospheric carbon dioxide (Clark *et al.,* 2009).

Spectral analyses of Holocene climate proxy records from different parts of the world revealed persistent periodicities of ~2300-2500, ~1000, ~700 and ≤500 years that is often interpreted as an indication of variations in solar activity during the Holocene (Debret *et al.,* 2009; Soon *et al.,* 2014; Marsicek *et al.,* 2018; Wanner *et al.,* 2018). Power spectra of the solar activity reconstructed from [10]Be and ^{14}C in the GRIP ice core (Vonmoos et al., 2006) show distinct peaks around 700, 500 and 350 yr, as well as the well-known 210 yr peak (Suess or de Vries cycle) in the last 6 kyrs (Wanner et al., 2008). Analysis of a combination of different [10]Be ice core records from Greenland and Antarctica with the global ^{14}C tree ring record demonstrated presence of significant periodicities at 210, 350 and 1000 yr and less significant cycles at ~500 and 710 yr that are also found in some Asian climate records (Steinhilber *et al.*, 2012).

An earlier reported ~ 1500-yr Bond cycle corresponding to North Atlantic oceanic circulation (Bond *et al.,* 1997; Bianchi and McCave, 1999; Loehle and Singer, 2010) may have widespread global distribution, but only in the late Holocene (Debret *et al.,* 2009). The 1500-yr cycle was reported to dominate the Greenland ice core record and some deep sea cores (Wunsch, 2000; Schulz, 2002). Dima and Lohmann (2009) suggested that the internal threshold response of the thermohaline circulation (THC) to solar forcing is more likely to produce the observed 1500-yr periodicity. The leading explanation of rapid climate fluctuations is cooling and freshening of the North Atlantic by an influx of freshwater (Bond *et al.,* 1999). Rapid climate fluctuations during the early Holocene are explained to be related to feedback mechanisms linked to amplified changes in the amount of solar radiation with the ~ 1000-yr cyclicity with internal climate system

variability with the ~1500-yr cyclicity being important for the second half of the Holocene (Debret *et al.,* 2009). Different feedback mechanisms have been suggested to amplify the centennial scale climate changes caused by solar activity (Gray *et al.,* 2010). The suggested feedback mechanisms include changes in the zonal equatorial and meridional circulations (Walker and Hadley circulations), cloud increase and decrease of solar radiation, direct total solar irradiance increase and decrease over relatively cloud-free subtropical oceans, stratospheric ozone changes, planetary wave propagation when the wind anomaly moves poleward and downward with time and grows significantly in amplitude, stratosphere and troposphere coupling, centennial scale irradiance variations, and changes in energetic particle fluxes. At the same time the 1500-yr cycle observed in the North Atlantic circulation during the last 6.5 kyr is suggested to be of non-solar origin connecting the cycle to internal variability with distinct periods of storminess (Sorrel *et al.*, 2012). The reconstructions of the Holocene sea-ice drift record in the Arctic showed a strong 1500-yr cycle that does not match the spectral characteristics of solar-forcing records suggesting that the circulation patterns in the Arctic Ocean on millennial timescales are not influenced by the solar forcing (Darby *et al.*, 2012). However, the study of the lake sediments in Central Germany suggested that periods of increased storminess occur when solar activity is lowest and solar variability may be influencing climatic changes (Martin-Puertas *et al.*, 2012). All these studies demonstrate that various forcing mechanisms and periodicities may co-exist in the Holocene and different regions may be impacted differently by the combination or domination of some or all of these mechanisms.

Some studies consider that Dansgaard-Oeschger (DO) events (rapid climate fluctuations during the last glacial period) are quasi-periodic (Grootes and Stuiver, 1997) and are separated by intervals with multiples of ~ 1470 years (Rahmstorf, 2003). Such oscillations resemble the Holocene Bond cyclicity (ice rafting events that are linked to climate fluctuations), however, the absence of a regular signal when only multiples are present, is hard to explain. Pisias et al. (2010) obtained the spectral power mode at ~1600 yr when analyzing 38 paleoclimatic records from different parts of the world in the interval of 60–26 ka. Contrary to Rahmstorf (2003) they interpreted such periodicity to be associated with changes internal to the climate system. Long and Stoy (2013) reported that the millennial-scale periodicities in the oxygen isotope records of the Greenland Ice Sheet Project 2, North Greenland Ice Core Project (NGRIP) and sea-surface temperature derived from the Bermuda Rise sedimentary core vary depending on the observational time interval. Some studies, however, showed that a possibility of random event generation for the DO cycles cannot be statistically rejected (Schulz, 2002; Ditlevsen *et al*., 2007; Peavoy and Franzke, 2010).

The Holocene periodicities of 1000-yr and 500-yr are already shown in the climatic proxy series of the Lake Baikal area and compared to the solar activity variance and sunspot number (Kravchinsky *et al.,* 2013). In our current study we analyzed LGM climate records to find out if similar centennial periodicities persisted during the 26 and 20.6 ka in the same Lake Baikal region. The reconstructions of the solar variations on the centennial timescale are available for the Holocene, not for the LGM, therefore analysis of the high-resolution climate proxies plays the leading role in revealing persistent Sun–climate links before the Holocene. It was shown that solar minima correlate with more

negative $\delta^{18}O$ values in the Greenland ice record on the centennial timescale (150–500 yr) suggesting the existence of strong solar forcing on the climate between 22.9 and 14.7 ka (Adolphi *et al*., 2014). The ~2300-2500 yr cycle in the Holocene appears to be the Hallstatt cycle related to the solar activity variations (Usoskin *et al*., 2016) or to a major resonance involving the movements of the four Jovian planets that changes the cosmic ray and dust densities in the inner region of the solar system modulating the radionucleotide production and influencing climate through a cloud modulation (Scafetta *et al*., 2016).

Our data were obtained from the continuous sedimentary record of the Lake Kotokel sediment core KTK10/6, east of Lake Baikal (Fig. 4.1) (drilling site at 52°47.276'N, 108°07.435'E). Müller *et al.* (2014) reported a pollen percentage and a linear age model from the previous study of Bezrukova et al. (2010) in order to evaluate the environmental stability of the region for a large population of herbivores. They demonstrated that the LGM environment of the Lake Baikal region was favorable for inhabiting by hunter–gatherer groups. In this study we report and make public higher resolution results of the pollen analysis comparing to Müller *et al.* (2014) in order to evaluate centennial scale climate variations. We also present a new nonlinear age model using seven accelerator mass spectrometry (AMS) radiocarbon (^{14}C) dates from the sediment core KTK10/6 reported. Tentative linear age model was used in Müller *et al.* (2014) that worked well for describing long-term features but cannot be used for centennial scale event determination. The core was collected from a site in the southern part of Lake Kotokel (Fig. 4.1c). In this study we present the detailed total pollen concentration (TPC) and percentage of

Cyperaceae and *Artemisia*, two types of plants, as these parameters occur in the greatest abundance in Lake Kotokel and depend directly on the humidity conditions in the region.
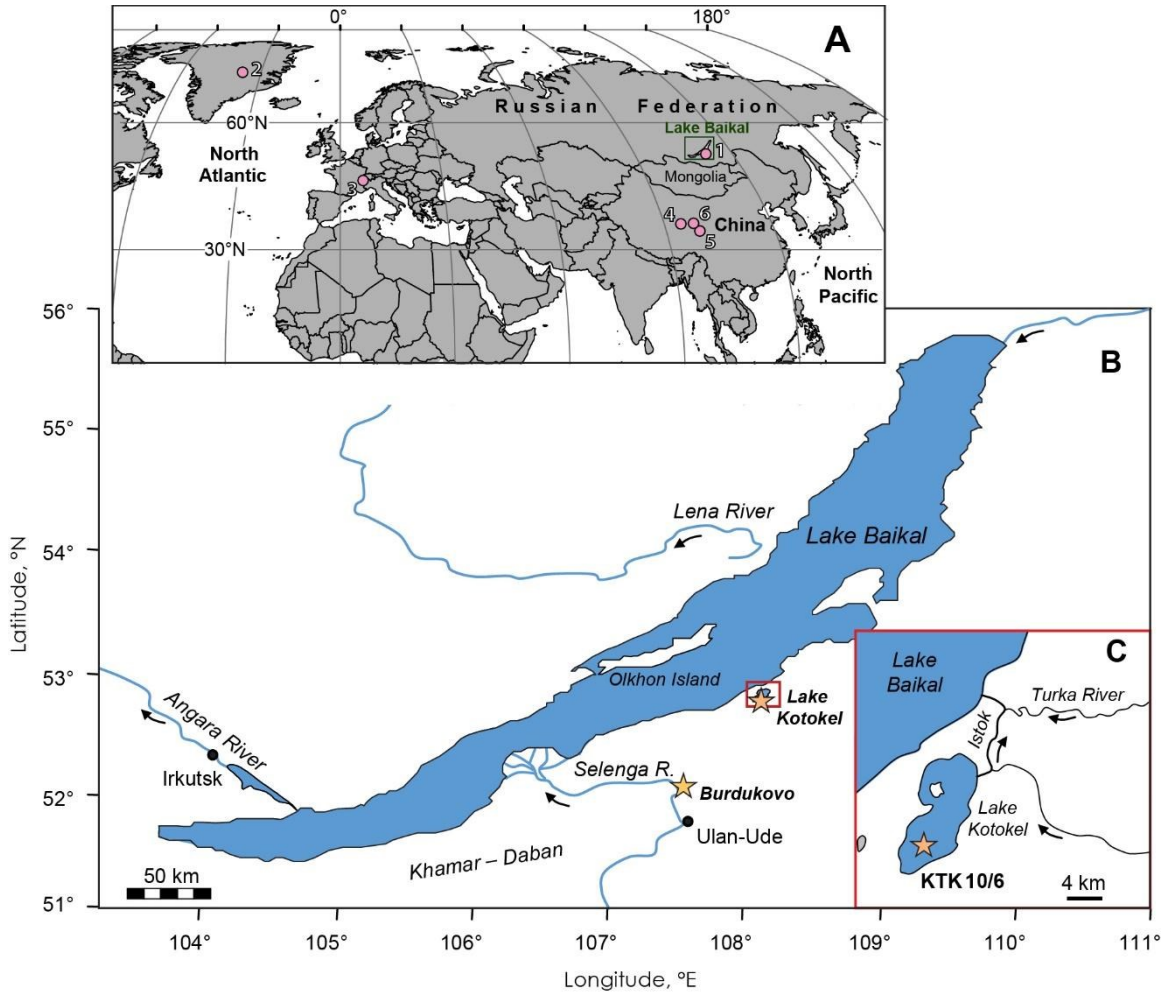
Fig. 4.1 **a)** Geographic location of the study region and other sections used for comparison. b) Location of the Lake Kotokel coring site and the Burdokovo loess-soil section site (Kravchinsky *et al.*, 2013). c) Close-up of the coring site location in Lake Kotokel.

The Lake Kotokel drainage basin is situated in the area of forest-steppe and steppe ecosystems that are highly sensitive to climatic changes created by the interaction of the

three largest systems of atmospheric circulation: Siberian Anticyclone, Westerlies, and Pacific monsoon (Bezrukova *et al.,* 2010; 2011). Dry, cold and sunny winter weather is associated with the Siberian Anticyclone centered at ~ 50°N/100°E. The Anticyclone has a direct influence on the surface air temperature and the Pacific winter monsoon routes (Gong *et al.,* 2001; Panagiotopoulos *et al.,* 2005). The westerly wind from the Atlantic dominates through the year and transports precipitation during autumn and spring, weakening in the summer when warm and wet Pacific air bringing heavy rainfall to the region (Bezrukova *et al.,* 2008, 2010).

The palynology studies of the Lake Kotokel core sediments already demonstrated that the timing and succession of major climatic events in the Kotokel record corresponded to all climatic events registered previously at other lakes in the region including Lake Baikal at mid-latitudes of Eurasia (Tarasov *et al.,* 2005; Shichi *et al.,* 2009; Bezrukova *et al.,* 2008, 2010, 2011; Müller *et al.,* 2014). The sediments record Marine Isotope Stages 1–3, the Younger Dryas, LGM and smaller scale climatic events. Total pollen count (grains/g) and biome scores for steppe and taiga were used in these studies as palaeoclimatic indicators in the Lake Kotokel and Lake Baikal region. Synchronism of short-term climatic fluctuations in the Lake Kotokel and Lake Baikal area with global fluctuations revealed that the pollen analysis provides an excellent climate proxy that was confirmed with geochemistry, diatom analysis and oxygen isotope studies (Tarasov *et al.,* 2009; Kostrova *et al.,* 2016). A redistribution of the atmospheric moisture balance was suggested as a possible mechanism behind rhythmic variations in the environment of the southern part of East Siberia and the Lake Kotokel (Bezrukova *et al.,* 2008, 2010, 2011; Tarasov *et al.,* 2009; Shichi *et al.,* 2009; Müller *et al.,* 2014), therefore variations in

pollen concentration were used as a climate proxy to evaluate relative moisture changes. To reconstruct centennial scale climate fluctuations during the LGM and compare them with available global records, we analyzed a high resolution time series of total pollen concentrations in Lake Kotokel. *Artemisia* (e.g. wormwood, sagebrush, etc.), *Poaceae* (grasses), and *Cyperaceae* (sedges) comprised up to 90% of the pollen in the sediments (Müller *et al.,* 2014), which together with a rich variety of other herbaceous taxa indicates productive vegetation during the LGM. The pollen and non-pollen palynomorph assemblage representing the LGM interval is described in Müller *et al.* (2014). Low percentages of boreal tree and shrub pollen taxa demonstrate an absence of cold deciduous forest biome in the record and imply that the LGM climate was generally colder and drier than today's climate. There is no evidence that the LGM climate was desertic, as pollen percentages of *Chenopodiaceae* and *Ephedra* – taxa typical in the arid inner Asia – were very low (Müller *et al.,* 2014).

4.2 Methods

4.2.1 Sampling, Measurements, Dating

The length of the undisturbed KTK10/6 core section was 190 cm (the depth of the core top was 970 cm). The sampling and lithological description was done on the working half of the core in the Institute of Geochemistry (Russian Academy of Sciences, Irkutsk). The top and middle parts of the KTK10/6 core consist of dense homogenous dark grey slightly laminated silty clay which becomes greenish dark grey in the bottom

part of the KTK10/6 core. The half core was cut into 1 cm slices, packed in plastic containers and transported to the Free University (Berlin) for further analyses. The core has undisturbed organic mud through the whole length; bulk samples for sever depths were sampled for the AMS radiocarbon ^{14}C dating. The dating was performed in the Poznan Radiocarbon Laboratory (Poland). The age spans of pollen and non-pollen palynomorph (NPP) records, based on seven AMS radiocarbon (^{14}C) dates, extended from 20.6 to 26 ka and thus covered the Last Glacial Maximum (LGM) in the definition of Clark et al. (2009).

To build a reliable age model based on the available AMS radiocarbon dates we used the Bayesian statistics approach based on controlling core accumulation rates utilizing a gamma autoregressive semiparametric model (Blaauw and Christen, 2011). Instead of linear interpolation between the average ages that assumes that there was constant sedimentation rate in between, the Bacon algorithm divides a core into many small sections and via Markov Chain Monte Carlo analysis estimates the sedimentation rate for each of these sections independently. In recent years the method has been extensively used to construct age models for the lake and peat sediments (e.g., Blaauw *et al*., 2020; Kaufman *et al*., 2020). The approach is particularly effective for high-density dated cores but also provides reasonable results in low-density dated cores.

Table 4.1 The AMS radiaocarbon dates from the Lake Kotokel sedimentary cores KTK10/6. Uncalibrated dates for the KTK10/6 samples were published in Müller *et al.* (2014). The ages were obtained in the Poznań Radiocarbon Laboratory, Poland, using

bulk sediment. Calibrated age was obtained using the Bayesian statistics approach and software (Blaauw and Christen, 2011; Blaauw *et al*., 2018) applying the calibration curve IntCal20 (Reimer et al., 2020).

Number	Core	Depth (cm)	Sediment type	Uncalibrated age	Calibrated age (calendar years before present)
1	KTK10/6	15-16	Dark grey silty clay	17,230± 90	20,881 ± 298
2	KTK10/6	35-36	Dark grey silty clay	17,310 ± 90	21,370 ± 420
3	KTK10/6	55-56	Dark grey silty clay	18,410 ± 100	22,336 ± 265
4	KTK10/6	75-76	Dark grey silty clay	20,560 ± 120	23,278 ± 458
5	KTK10/6	105-106	Dark grey silty clay	20,120± 90	24,134 ± 268
6	KTK10/6	145-146	Dark grey silty clay	21,780 ± 110	25,246 ± 485
7	KTK10/6	185-186	Dark grey silty clay	21,590 ± 100	25,963 ± 269

In this study we constructed a new age model for the Lake Kotokel sediments that differs from the original linear age model in Müller *et al.* (2014) which was based in turn on the age model of Bezrukova *et al.* (2010). We used the seven radiocarbon dates obtained from an analyzed segment of the KTK10/6 core (Fig. 4.2, Table 4.1). The AMS dates were used as the input for the Bacon software developed by Blaauw and Christen (2011) to construct a robust nonlinear age model. In addition to the absolute dates from both cores, the Bacon software utilizes the expected accumulation rate for lacustrine sediment and allowable rate of change of sediment accumulation ("memory" in the

software). The approach uses these inputs to construct a non-gaussian autoregressive model for sediment accumulation which is informed by *a priori* knowledge of typical accumulation rates. Information on accumulation rates of Lake Kotokel in the Holocene and LGM is still scarce, therefore we used sedimentation rates for a similar age interval in records from the neighbouring Lake Baikal (Tarasov et al., 2005) and Lake Baunt (Solotchin et al., 2020) to make a preliminary estimate of 30 cm/kyr and use this value as initial input in Bacon software. An age model was then modified to better fit the actual age/depth record. We maintained the default 5 cm thickness for the cores in order to treat each age/depth pair as a point observation.
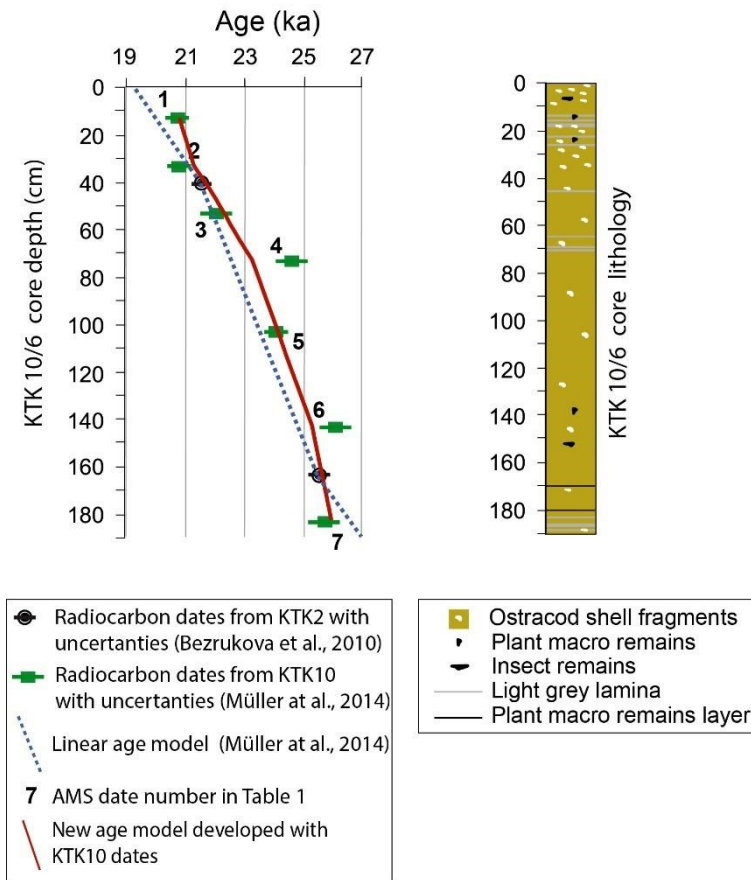
Fig. 4.2 Newly developed nonlinear age model for the Lake Kotokel core KTK10/6 (red line) using the Bayesian statistics approach (Blaauw and Christen, 2011) in comparison with previous linear age model (dotted blue line) for the cores KTK10/6 and KTK2 sampled at the same site (after Müller *et al.,* 2014).

Upon comparison to the original age model developed by Müller *et al.* (2014), the dates for the samples are all shifted slightly older temporally, but the slope remains largely the same indicating there is no significant difference in sediment accumulation rates, and these rates fall well within those expected for lacustrine sediments in this region (Tarasov et al., 2005; Solotchin et al., 2020). Final calibrated age results using the Bayesian statistics approach from the Bacon software, that uses the calibration curve IntCal20 (Reimer et al., 2020), show that the mean 95% confidence interval width is 857 yr with 71% of dates intersecting the 95% confidence interval for the age model (Fig. 4.3). The core section comprises homogeneous, laminated, grey silty clay without any microscopic signatures of sediment composition change or bioturbation that repudiate a possibility of sudden fluctuations or reversals in sedimentation rate (Bezrukova *et al.*, 2010; Müller *et al.*, 2014). Therefore based on the Bayesian statistics approach result we accepted that the age model should not be largely affected by three points deviating from the general trend (35-36 cm, 75-76 cm and 145-146 cm).
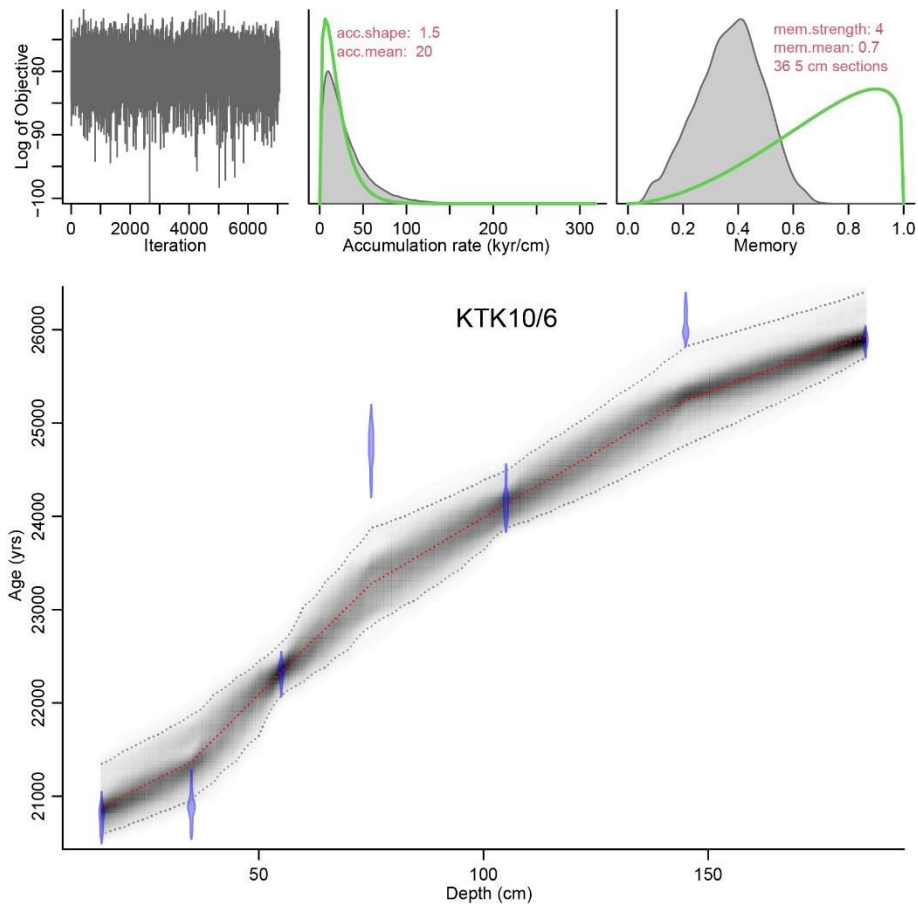
Fig. 4.3 The age model construction outcomes of the Bacon software (Blaauw and Christen, 2011). Top left panel shows Markov Chain Monte Carlo iteration number, and the distance from the objective (iterations stop when changes between interactions are small). Center top panel showing prior (green) and subsequent (grey shaded) histogram for sediment accumulation rate. Top right panel showing histograms for prior (green) and subsequent (grey shaded) memory, or autocorrelation. Main panel shows KTK age/depth input values (blue points), final age/depth relationship (dashed red line) and 95% confidence interval (shaded grey area).

To obtain the pollen composition and concentration 188 samples were analyzed from the Lake Kotokel KTK10/6 core (Fig. 4.4). 60 pollen taxa and 70 non-pollen palynomorphs were identified (Müller *et al.,* 2014).
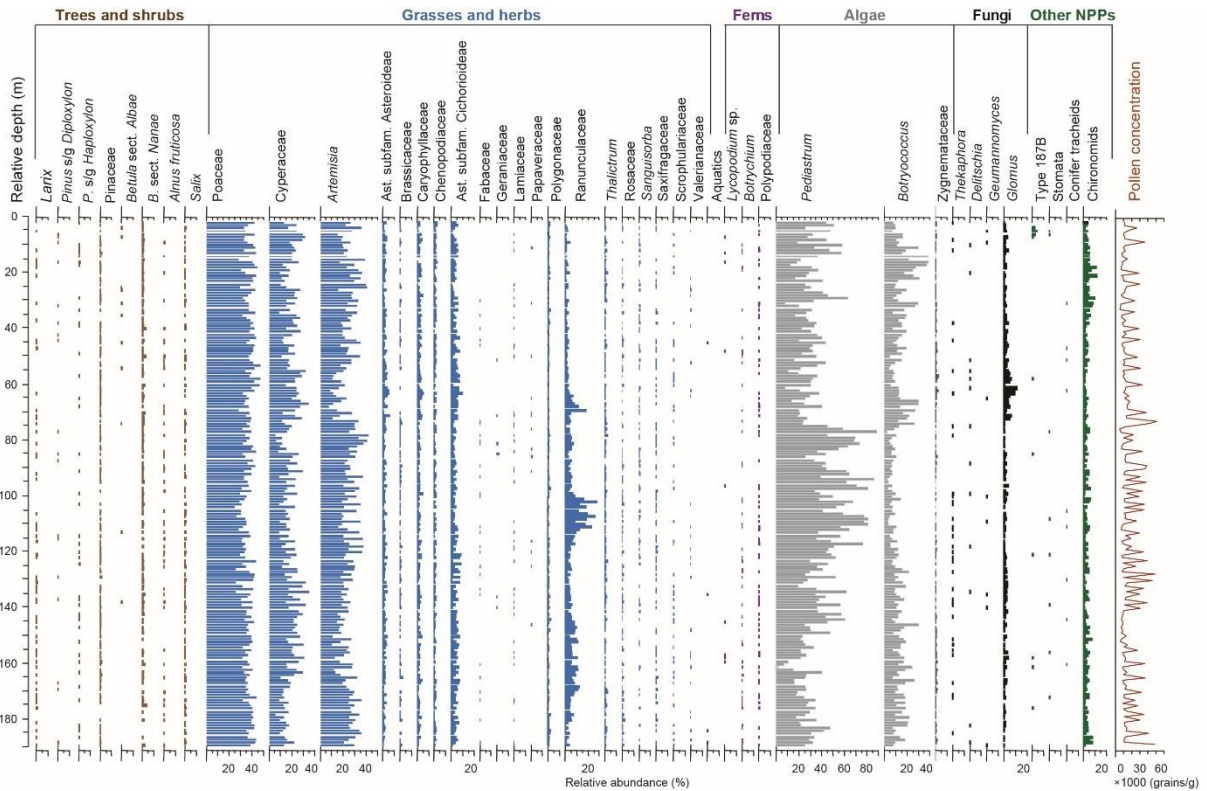
Fig. 4.4 Lake Kotokel pollen percentage diagram including percentages of the selected non-pollen palynomorphs (NPPs) (re-plotted after Müller *et al.,* 2014).

4.2.2 Wavelet analysis of climatic records

Wavelet analysis is particularly useful for non-stationary time series, which are dominated by periodicities that change with time (Debret *et al.,* 2007). The advantage of wavelet analysis in detecting climatic periodicity was demonstrated on numerous climatic

records to evaluate millennial and centennial cycles (Debret *et al.,* 2007). We used the Morlet wavelet implemented in the Matlab code (Torrence and Compo, 1998). Monte Carlo simulation was used to assess the statistical significance of peaks in wavelet spectra. Resulting original data curves were detrended to remove the effect of the long-term climate changes usually related to the Milankovitch cyclicity. To calculate the trend we used the nonlinear locally weighted polynomial regression using weighted linear least squares and a 2nd degree polynomial model implemented in the Matlab functions "smooth" and "loess". The detrended data were resampled in regular intervals (10–40 yr) and normalized for the spectral analysis as Normalized Parameter = Parameter - mean(Parameter)variance (Torrence and Compo, 1998). Background noise for each signal was estimated and separated using the singular spectrum analysis. Autoregressive (AR) modelling implemented in Torrence and Compo (1998), where AR(1) is red noise that is larger than zero, was used for each noise time series to determine the AR(1) stochastic process against which the initial time series was tested.

4.3 Results

Analyses of the pollen data and pollen-based biome allowed reconstructing the LGM environment in the region when steppe and tundra vegetation were composed mostly of grasses and various herbs (Bezrukova *et al*., 2010; Müller *et al*., 2014). The needleleaf coniferous and broadleaf deciduous tree and shrub taxa in our study are thinly distributed and typically presented between 2.4 and 5.4% of the total pollen concentration (TPC)

(Fig. 4.4). The main component in the analyzed TPC is the herbaceous pollen taxa. The most abundant grasses Poaceae (25–40%), sedges Cyperaceae (10–35%) and sagebrush Artemisia (10–40%) are typical for herbaceous tundra and the steppe in the Lake Baikal area. The other grasses presented in smaller quantities are Asteraceae subfamily Cichorioideae (up to 8%), Caryophyllaceae (up to 6%), and Asteraceae subfamily Asteroideae (up to 6%) and Ranunculaceae (the percentage varies largely in the core). The total pollen concentration averages at $\sim16\times10^3$ grains/g with alterations between $\sim4.75\times10^3$ and $\sim51\times10^3$ grains/g. Variations in the pollen composition do not indicate any abrupt changes in the core, which implies that the region surrounding Lake Kotokel was covered by relatively stable vegetation during the LGM (Müller *et al.,* 2014). The Lake Kotokel fossil pollen concentration provides a reconstruction of vegetation and environments in continental Asia between 20.6 and 26 ka with temporal resolution of $\sim$ 40 yr.

The total pollen concentration was a superposition of various pollen taxa in the record. The increase in the pollen concentration corresponded to the relatively warmer and wetter climate and linked to the increase in diatom concentration in the Lake Baikal, Lake Kotokel and the surrounding region (Tarasov *et al.,* 2009; Bezrukova *et al.,* 2010; 2011; Kostrova *et al.,* 2016). The total pollen concentration (Fig. 4.4) acted as a stacked climatic parameter that smoothed the record but at the same time balanced out some uncertainties related to individual reaction of particular taxa to specific short-term conditions.

The grassland vegetation in the area was generally stable during this period, which would provide a persistent source of nourishment and a sustainable environment for large populations of herbivores, and consequently for local hunter-gatherers in the Lake Baikal region. Previous pollen and diatom analysis demonstrated that relatively wetter climate conditions corresponded to the less continental climate and relatively drier conditions corresponded to the cooler climate (Tarasov *et al.,* 2009; Bezrukova *et al.,* 2010, 2011; Kostrova *et al.,* 2016). Wetter and warmer environment was characterized by general increase of vegetation on the shore that led to increase of the TPC values in our record. Fig. 4.5 illustrates the comparison of *Cyperaceae*, a type of plant that is associated with a wetter environment, and *Artemisia*, typical representative of steppe vegetation, i.e. drier environment. These two taxa demonstrated the inverted relationship indicating a relatively wetter vs. drier environment. We normalized and stacked together the two records for further spectral analysis to reduce any data uncertainty related to the lab measurements and field sampling. The stack is more sensitive to the moisture variations in the region comparing to the TPC that is sensitive for both temperature and moisture variations.
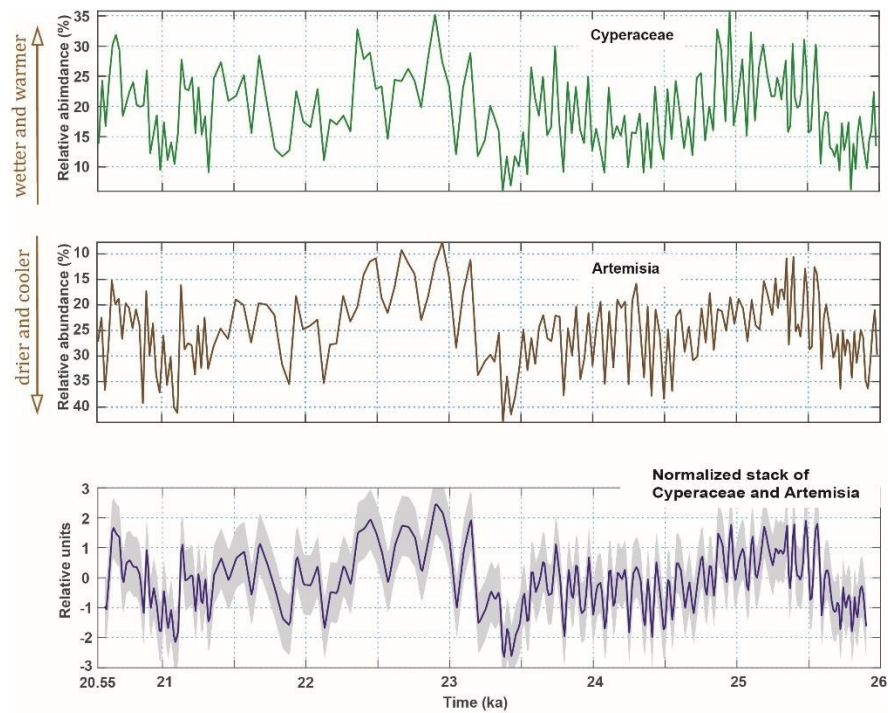
Fig. 4.5 Pollen percentage diagram for *Cyperaceae* and *Artemisia*. The stacked record of both taxa was normalized and detrended. The standard deviation shown in grey.

To explore whether the Lake Kotokel record corresponds to global climatic variations during the LGM we compared our total pollen record with the oxygen isotope $\delta^{18}O$ record from the Greenland ice core project (NGRIP) (Rasmussen *et al*., 2014), dust-fall contributions in Lake Qinghai in China (An *et al.,* 2012), grain size at the Jingyuan and Gulang loess sections near Tengger Desert (Sun *et al.,* 2012) and the composite oxygen isotope $\delta^{18}O$ record from the Alpine cave system 7H (Luetscher *et al.,* 2015) (Fig. 4.1). The $\delta^{18}O$ NGRIP record (75.10° N, 42.32° W) has a resolution of 20 years and is accurately dated (Rasmussen *et al*., 2014) and has therefore it become a climatic reference curve for other paleoclimate records for worldwide comparison and especially for the Northern Hemisphere (i.e., Moreno *et al*., 2014; Mingram *et al*., 2018). The

NGRIP record revealed large millennial and centennial scale variability that is interpreted to be driven by the temperature changes (Kindler *et al*., 2014). The Alps are a barrier for meridional moisture transport and therefore record shifts in the North Atlantic storm track pattern is recorded in the Alpine cave system 7H (46°44'58"N, 7°48'28"E) (Luetscher *et al.,* 2015).

The Lake Qinghai Westerlies climate index (dust flux of > 0.25 μm fraction) is the only climate proxy record in Asia with a resolution (~20 yr) comparable to that of Lake Kotokel (~40 yr). Time series plots of the NGRIP oxygen isotope, the Lake Qinghai dust flux index, Gulang loess grain size, and the Lake Kotokel stack of *Cyperaceae* and *Artemisia* and pollen concentration records are presented in Fig. 4.6. The oxygen isotope record from Greenland demonstrates frequent low amplitude changes in average temperature, with the warmest interval at ~ 23.6 ka and a cooler climate between ~ 23.5 and 26 ka (Fig. 4.6a). Lake Qinghai (36°32'–37°15' N, 99°36'–100°47' E), the largest lake in China, is situated in the border area between the humid monsoon-dominated and the arid continental climate zones (An *et al*., 2012). The dominant arid climate during the LGM brought more dust during relatively cooler intervals. The high dust flux in the Lake Qinghai record corresponds to strong winds and a cool climate (Fig. 4.6b); therefore, the vertical axis in the Lake Qinghai Fig. is inverted relative to the NGRIP and Lake Kotokel records.

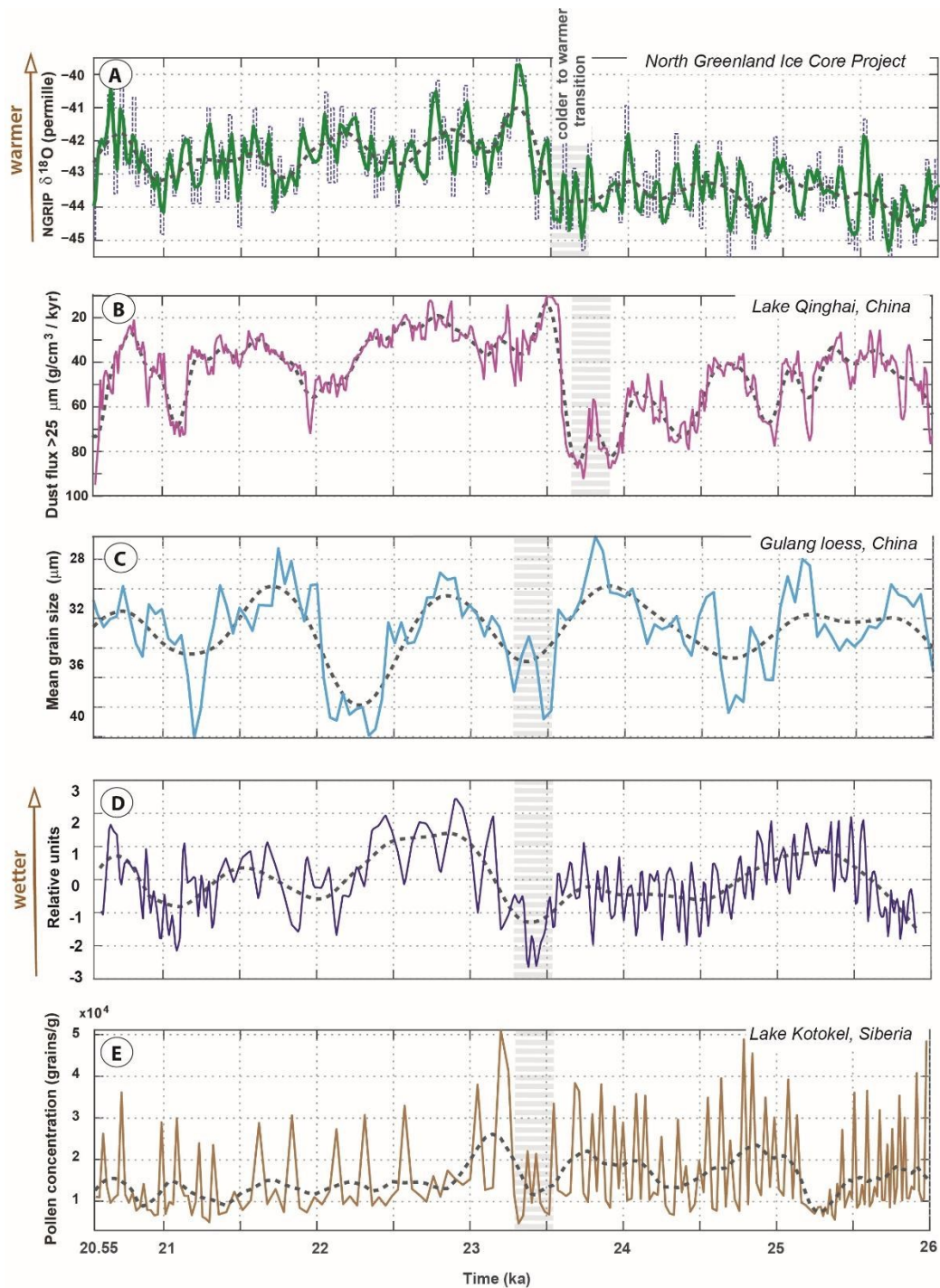Fig. 4.6 Comparisons of a) NGRIP oxygen isotope δ¹⁸O from Greenland
(Rasmussen *et al.*, 2014), b) Lake Qinghai dust flux Westerlies climate index (dust flux
of > 0.25 μm fraction) (An *et al.,* 2012) (note inverted vertical axis), c) Grain size of the

Gulang loess, China (Sun *et al.,* 2012), d) Stack of *Cyperaceae* and *Artemisia* (this study), e) Total pollen concentration in samples from Lake Kotokel (this study). Thin dashed blue lines are original data; green, magenta, blue and brown solid lines represent data that have been smoothed and resampled into equally spaced intervals; the thick dashed grey line is smoothed data, calculated using Matlab function "loess" weighting 5-10% of the whole data set, to visualize the centennial and millennial periodicity.

Loess deposits at Jingyuan (36.35° N, 104.60° E) and Gulang (37.49° N, 102.88° E) are situated in the depocentre of modern dust storms near Tengger Desert (Sun *et al*., 2012). High sedimentation rates and weak pedogenesis make these loess locations sensitive recorders of rapid monsoon changes where the sedimentary grain size primarily reflects changes in winter monsoon strength. The Gulang loess grain size shows higher amplitudes with abrupt transitions (Fig. 4.6c) and the Jingyuan loess has higher accumulation rates and coarser grain size with smoother amplitudes.

The stacked record of *Cyperaceae* and *Artemisia* is generally more sensitive for the wetter/drier climate variations (Fig. 4.6d), and pollen concentration increases during warm intervals and decreases when the climate conditions are cold (Fig. 6e). The pollen quantities reflect regional and local vegetation compositions around Lake Kotokel and vary with apparently larger amplitudes of cool and drier to warm and wetter climate compared to the $\delta^{18}O$ record from the Greenland ice. Since neither the pollen nor the other records are calibrated to temperature, it is unknown which has the larger amplitude

temperature variations. It is also possible that the relationship between climate and the Lake Kotokel pollen concentration could be non-linear to some degree.

There is no striking visual correlation among the NGRIP oxygen isotopes, the Lake Qinghai dust flux, the Gulang loess grain size, and the Lake Kotokel pollen concentration in Fig. 4.6. Possible reasons for that include chronological uncertainties of the data, natural lags in global climate events (Clark *et al.,* 2012), and ocean and continental feedback mechanisms that cause amplification of, or a lag in, particular events (Claussen *et al.,* 2003). We applied thousands of various lags between the records in an iterative manner, but there was no significant improvement in the correlation coefficient. Therefore we plotted a trend line using the locally weighted linear least-squares regression "loess" implemented in Matlab to highlight the visuality of centennial and millennial duration features (black dashed lines in Fig. 4.6), where short events are smoothed out. Five to eight millennial length cycles can be visually identified in the records, although the peaks are shifted relative to each other suggesting different individual proxy responses to the centennial scale global climate change and/or age model imperfections.
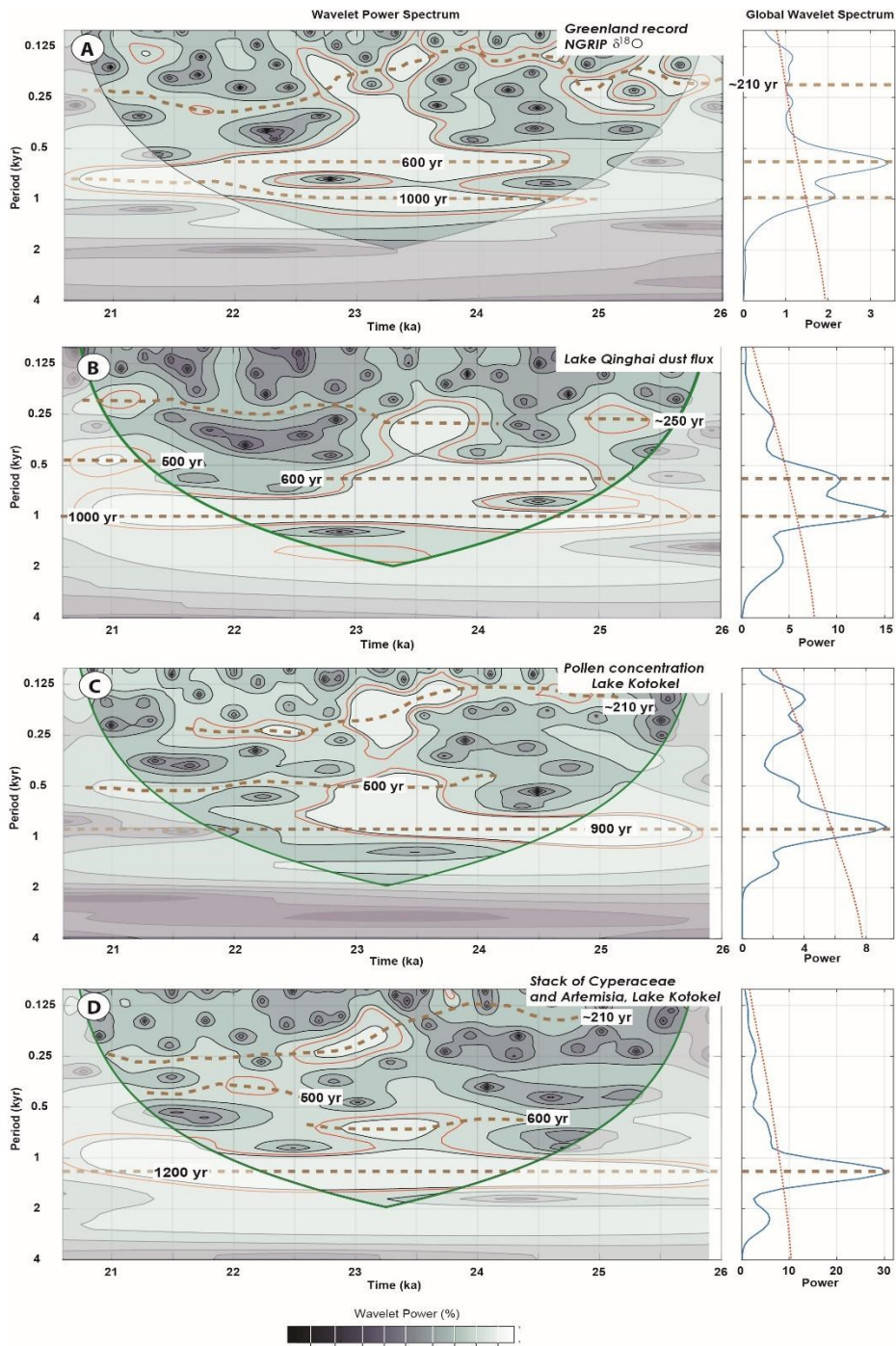
Fig. 4.7 Wavelet transform analyses of the a) 20.6–26 ka interval for the NGRIP

oxygen isotope from Greenland (Rasmussen *et al*., 2014), b) Lake Qinghai dust flux

Westerlies climate index (An *et al.,* 2012), c) total pollen concentration in samples and

stacked record of *Cyperaceae* and d) *Artemisia* from Lake Kotokel. Dashed horizontal lines represent 1000-, 500-, and 250-yr periods. Darker shaded cone shaped areas correspond to cones of influence; the green cone line is the 95% confidence spectrum. Confidence levels of more than 95% are indicated with a red line. Fourier power spectra of the parameters are in separate Fig.s at the right of the main diagrams; the red dashed line is the mean red noise spectrum.
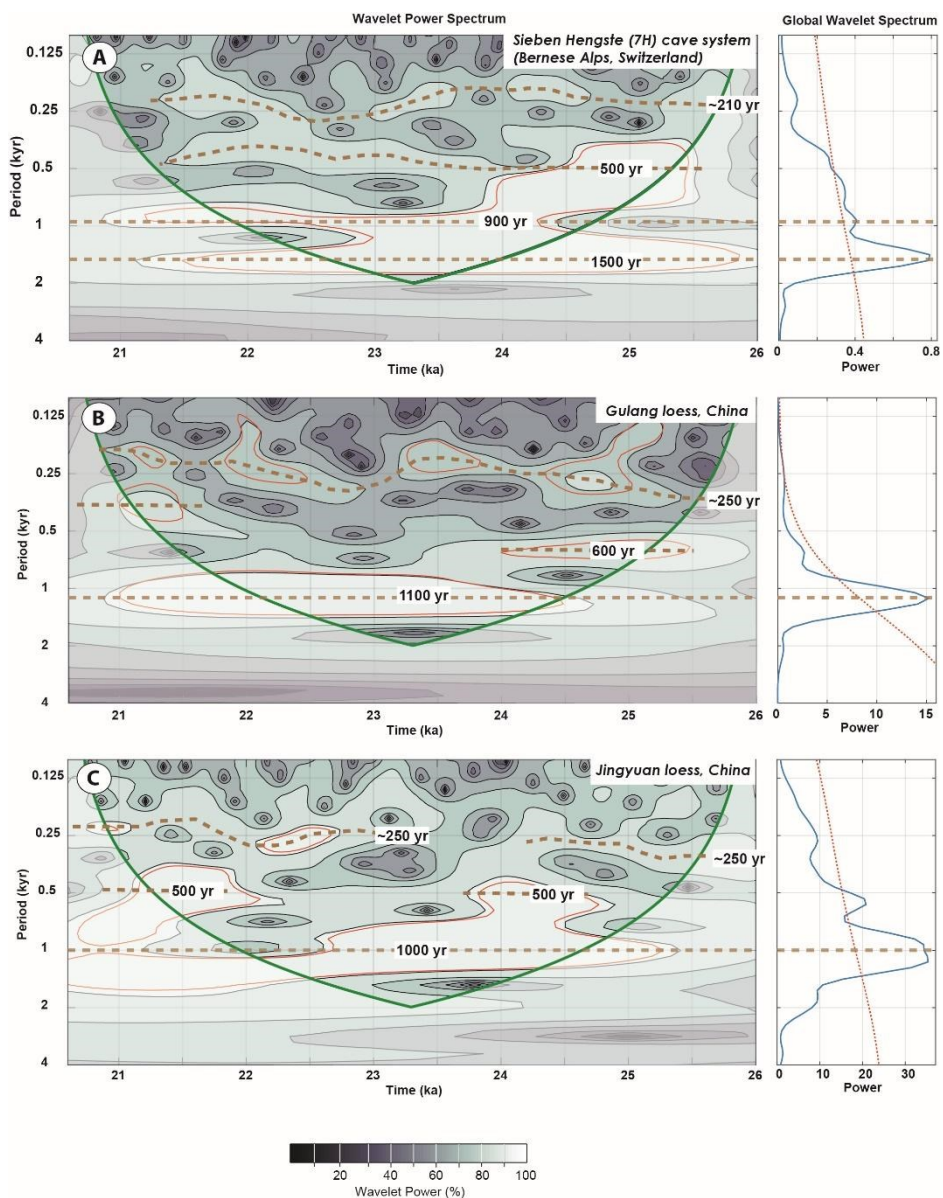
Fig. 4.8 Wavelet transform analyses of the a) 20.6–26 ka interval for the composite oxygen isotope [18]O record from the Alpine cave system 7H (Luetscher *et al.,* 2015) and the grain size at the b) Jingyuan and c) Gulang loess sections near Tengger Desert (Sun *et al.,* 2012). Dashed horizontal lines represent 1000-, 500-, and 250-yr periods. Darker shaded cone shaped areas correspond to cones of influence; the green cone line is the 95% confidence spectrum. Confidence levels of more than 95% are indicated with a red line. Fourier power spectra of the parameters are in separate Fig.s at the right of the main diagrams; the red dashed line is the mean red noise spectrum.

To evaluate a common periodicity in the LGM climate we performed wavelet analyses (WA) on the Greenland ice core oxygen isotopes, the Lake Qinghai dust flux, the Lake Kotokel pollen time series, the stacked record of *Cyperaceae* and *Artemisia* (Fig. 4.7) and the composite oxygen isotope $\delta^{18}O$ record from the Alpine cave system 7H and the grain size in the Gulang and Jingyuan loess (Fig. 4.8). The WA highlights major features at the 95% confidence level; the most prominent cycle in the records is the ~1000-yr cycle throughout most of the LGM period. The ~1500 yr cycle in the Alpine cave system 7H reflects the North Atlantic storm track pattern that are similar to the circulation patterns in the Arctic Ocean and are not influenced by the solar forcing as suggested by Darby *et al*. (2012). The ~1000-yr peaks of the NGRIP, Lake Qinghai dust flux, Lake Kotokel TPC and Jingyuan loess records are distinct throughout the studied LGM interval with some modulations towards longer periods in the stacked record of *Cyperaceae* and *Artemisia*, composite oxygen isotope $\delta^{18}O$ record from the Alpine cave system and Gulang grain size records. Almost the same peak with the maximum at 900-yr can be traced in the Lake Kotokel pollen concentration wavelet analysis spectrum at

22.5–26 ka (Fig. 4.7c) when the millennial cycle amplitude variations are higher than for the interval 20.6–22.5 ka. The average spectral peak in the stacked record of *Cyperaceae* and *Artemisia* is centered at 1200-yr cycle (Fig. 4.7d). The difference with the 1000-kyr peak in other records could be driven by less sharp individual responses of these two types of plants to the humidity and temperature changes in the study region and/or sensitivity of these plants to other environmental factors or be related to a stronger temperature sensitivity of the total pollen concentration vs. a hydrological sensitivity of the Cyperaceae-Artemisia stack. Fig. 4.9 demonstrates the correspondence of the ~ 1000-yr peaks in the relatively smoothed *Cyperaceae* and *Artemisia* stack and the more detailed total pollen concentration record. Sensitivity of the *Cyperaceae* and *Artemisia* record to the variations of moisture, rather than temperature, may lead to the appearance of the cycles at periodicity of ~1200 kyr. The peaks in Fig. 9 are extracted from the whole record by applying the "loess" function that is a built-in Matlab script (see Methods). The millennial peaks 1 and 2 in the TPC record have low amplitude and are manifested by ~500 kyr cycles 1a, 1b, 2a and 2b in the pollen concentration record. The millennial cycles 3–6 have higher amplitudes and are therefore well pronounced in the WA in the interval 22.5–26 ka (Fig. 4.7c). The *Cyperaceae* and *Artemisia* stack has fewer peaks and manifests the smoothing of the response in comparison to the total pollen concentration record. Low amplitude peaks 1b and 2a are recorded as one low amplitude peak. The higher amplitude peaks 2b, 3a and 3b are registered as one high amplitude peak, the peak 4 appears in both records, and the pollen concentration peaks 5 and 6 appear as one peak in the stack. The stack still demonstrates confidently that millennial scale cycles exist in the record, however, the smoothing character of the *Cyperaceae* and *Artemisia* record

cannot be used for accurate extraction of the individual cycles. The total pollen concentration recorded is the better recorder of the centennial scale climate cyclicity in Lake Kotokel.
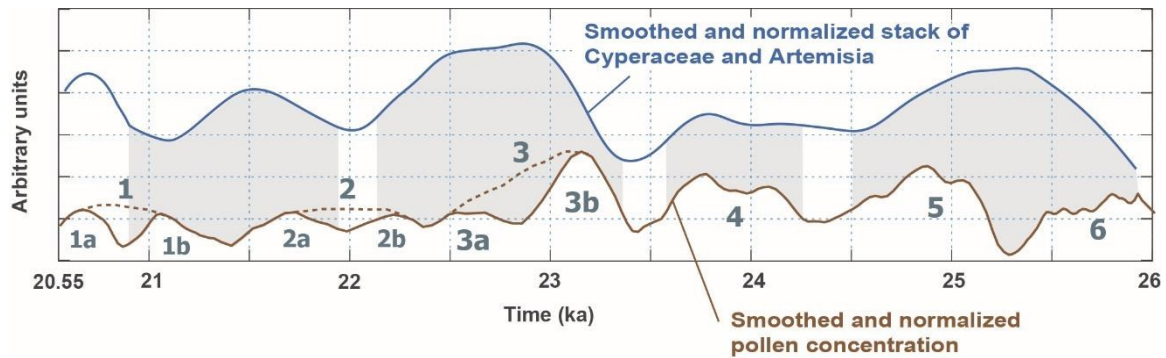
Fig. 4.9 Comparison of centennial and millennial scale cycles for the smoothed and normalized stack of the pollen percentage for *Cyperaceae* and *Artemisia* plants stack and total pollen concentration. Some of the peaks well pronounced in the total pollen concentration are much smoothed and therefore hidden in the stack illustrating that the total pollen concentration record is a better proxy of the centennial scale climate cyclicity.

Fundamental centennial scale solar modes at periodicities of 1000-yr and 500-yr, plus additional periodicities of ~ 700-yr and ~ 300-yr of an uncertain nature, are identified in the Holocene (Soon *et al.,* 2014). The LGM spectra in Figs. 4.6 and 4.7 indicate the presence of relatively weak cycles at ~500-600-yr and ~210-250-yr in all records, which appear at different time intervals. These cycles have weaker amplitudes compared to the 1000-1500 yr cycle in the climate proxy records and sun spot number in the Holocene (Kravchinsky *et al.,* 2013). The 500-600 cycle could be a harmonic or a modulation of

other cycles and it might not be compared exactly between each record considering the age model uncertainty in available records. At the same time, we may confidently report its presence in all the records discussed here. The ~210-250 cycle corresponds well to the de Vries cycle confidently observed in the Holocene (Steinhilber *et al*., 2012).

4.4 Discussion

The most prominent ~ 1000-yr and ~500-600-yr climate periodicity found in the Lake Kotokel pollen record during the LGM has been already reported in Holocene climatic series of the studied Lake Baikal region, in the insolation variance, and sunspot number (Kravchinsky *et al.,* 2013). The Siberian Holocene loess-soil Burdukovo site is close to the Lake Kotokel core site (Fig. 4.1). Both sections are situated in the Lake Baikal region of Siberia and are remote from the ocean. The Holocene spectrum is coherent in both sunspot number and solar modulation spectra at the statistically significant peaks of 1000 and 500 years.

Many Holocene climatic proxies from the North Atlantic Ocean, the Western Pacific Ocean, the Southern (Antarctic) Ocean, and the East Asian monsoon regions show fundamental periodicities of 2300, 1000, and 500 yr (Soon *et al.,* 2014), where 1000 and 500 yr cycles are identical to the periodicities in the LGM reported here. The strong 1000-yr peak in the Holocene spectrum matched the cosmogenic [10]Be and especially ^{14}C records from Northern Atlantic cores (Debret *et al.,* 2007). The concentration of these isotopes depends on solar radiation and the strength of the Earth's

magnetic field, and can therefore be expected to show similarity to the sunspot number and solar insolation variation spectra on the centennial time scale in the Holocene. The power spectrum of tree pollen concentration in the Lake Xiaolongwan sediments in Eastern Asia showed ~500-yr periodicity during the middle-late Holocene that was interpreted to be linked to the Greenland temperature change. The spectral analysis of the solar activity reconstructed from the ^{14}C from the tree ring worldwide records and ^{10}Be records from the ice core of the European Project for Ice Coring in Antarctica revealed statistically significant periodicities at ~210 yr (de Vries cycle), ~350 yr (unnamed cycle), and ~1000 yr (the Eddy cycle) in the last 9400 yrs (Steinhilber *et al*., 2012). They also reported less significant unnamed cycles at ~500 and ~710 yrs. Such periodicities are reported in the Asian climate (Wang *et al*., 2005) and sunspot number (Kravchinsky *et al*., 2013) during the Holocene. The Lake Kotokel TPC carries 500-600 yr periodicity similarly to these Holocene records.

Another prominent cycle in the Lake Kotokel record is centered at ~210-250-yr. It was suggested that the periodicity at 300-yr may hypothetically correspond to responses of the Atlantic thermohaline circulation to external solar modulation and pacing, but the exact reason is not known (Soon *et al.*, 2014). The cross-wavelet analyses of a late Holocene speleothem record from Dongge Cave in China showed statistically strong coherence similar to our study periodicities (200 and 340 yrs) suggesting that solar activities modulate Asian monsoon changes. Such periodicity is close to the ~ 210-250-yr cycle reported here for the LGM. The presence of the ~ 210 yr de Vries cycle in the ^{10}Be data from the GRIP ice core from Greenland was demonstrated between 50 and 25 ka

(Wagner *et al*., 2001) and between 22.5 and 10 ka (Adolphi *et al*., 2014). The age model for the GRIP core, however, was re-evaluated and synchronized to the NGRIP record later (Rasmussen *et al*., 2014). Nevertheless our WA analysis shows the presence of the cycle in the latest version of the oxygen isotope record of NGRIP (Fig. 4.7a).

The short-term variations of the Earth's motion around the Sun over the last 6000 years using 1-yr steps demonstrated that the main centennial scale climate periodicities related to the Earth's motion should be at 250-yr (eccentricity and obliquity) and at ~1000-yr (840-yr obliquity and precession and 930-yr eccentricity) (Loutre *et al.,* 1992). The authors concluded that while precession dominates at any latitude, the obliquity signal is stronger at high latitudes, making the 250-yr signal an important periodicity for climate research, although such changes cause additional amplitude changes in solar insolation of ~ 0.2 Wm^{-2} at the maximum (Soon *et al.,* 2014). The ~ 210-250-yr cycle can be clearly identified in the pollen record of Lake Kotokel (Fig. 4.7c, d), suggesting that the precession and eccentricity components (Loutre *et al.,* 1992) could also potentially contribute to the solar mode variations. At the same time, it has been widely discussed that a change of 1.5–2 W/m^2 in the Holocene solar radiation cannot explain the direct influence of solar variability on climate change without additional and still debated feedback mechanisms (Usoskin *et al.,* 2007). It was shown that the most prominent temporal features of the solar dynamo, including the de Vries cycle, can be explained by combined synchronization with tidal forcing of the Venus–Earth–Jupiter system and the periodic motion of the Sun around the barycenter of the solar system (Stefani *et al.*, 2021). The simulations of the Bond cycles before the Holocene suggested that it is

possible that the solar cyclicity is driven by a stochastic process and therefore quasi-periodic (Stefani *et al*., 2021). In contrast, other climate modeling and observation data in the Holocene suggest that solar forcing may trigger surface temperature variability and atmospheric dynamics via changes in cloud formation (Gray *et al*., 2010; Solanki *et al*., 2013), although a robust link between cosmic rays and cloud cover is not confirmed (Voiculescu and Usoskin, 2012). The review of suggested mechanisms that link solar variability and climate change is provided in Solanki *et al*. (2013). Although the mechanisms behind the centennial periodicities are still actively debated in the literature, our study demonstrates that the LGM climate proxy records from different regions are characterized by the cycles of comparable duration.

4.5 Conclusions

Highlighted by our spectral analysis similarities between Holocene and LGM climate oscillations in the deep continental interior of Asia, thousands of kilometers away from oceanic influence, and in Greenland and Alpine regions suggest that fundamental periodicities in glacial climate conditions and in models describing centennial solar activity can be extrapolated from the Holocene back in time to the LGM. Our findings suggest that such periodicities are a lasting attribute of climate change. The climate variations at ~1000, 500-600 and 210-250-yr were proposed to be linked to the variations of the amount of solar input to the Earth. Such variations may have always been an

existing factor of the global climate dynamics in the geological past in addition to widely

accepted Milankovitch cycles of much longer periods.

5. Conclusions/Future Work

The primary goal of this work was to reduce ambiguity surrounding centennial, millennial, and multi-millennial scale climate oscillations in the Quaternary and Neogene by adapting robust mathematical analysis techniques used outside paleoclimatology and assessing paleoclimate proxies through a signal analysis lens. Multiple time periods are considered in this work, each presenting a specific challenge that has contributed to ambiguity in the determination of paleoclimate cyclicity during that period. Delineating the extent of natural climate evolution taking place in the absence of anthropogenic influence is increasingly important as climate change continues to impact society. Understanding past climate change depends on resolving these ambiguities by implementing methods which improve the quality of paleoclimate time series' and provide consistent, repeatable climate cyclicity estimates which do not depend on visual interpretation. Results must be repeatable and consistent to better determine the relative impact specific climate forcing mechanisms have on a regional scale.

In chapter 2, the Synchrosqueezing Transform was applied to Northern Hemisphere Holocene proxies which provided a more sparse, easily interpreted *t-f* transform with improved frequency localization and reduced temporal smearing over the traditionally applied Continuous Wavelet Transform. In addition to these benefits, the Synchrosqueezing Transform is easily inverted providing a time domain reconstruction of individual climate oscillations present in a proxy record. By applying the SST in this way, it becomes much easier to compare specific oscillations between records and

interpret a set of paleoclimate proxy records rather than focusing on specific oscillations that may only be observed in this record. This chapter adapted the Synchrosqueezing Transform and its inverse to provide precise time-series reconstructions of known Holocene climate oscillations which have been observed in proxies throughout the Northern Hemisphere but lacked a consistent identification of the onset and cessation of each cycle. This lack of consistency is resolved using the inverse SST approach which identified distinct periods where the 0.5 kyr oscillation is strong across the Northern Hemisphere. The approach also revealed the mid-Holocene transition observed by Sorrel et al. (2012) in the north Atlantic is observed across all proxies identified and occurs at 5-6 ka. The synchronous observation of this event across the Northern Hemisphere has important implications on how global climate can be affected by regional changes in ocean water circulation.

Chapter 3 shows a Mio-Pliocene section in Shaanxi, China, which was re-sampled at a high resolution compared to past studies on this interval. The sampling resolution was sufficient to capture orbital obliquity cycles in the interval 2600-5300 Ka at a frequency higher than the Nyquist criterion dictates. Measurements of magnetic susceptibility (Low Frequency, High Frequency, and Frequency dependence) are dated using a previously developed age model and refined using orbital eccentricity cycles. The resulting time series is evaluated using the inverse Synchrosqueezing Transform described in Chapter 2, a specific oscillation with periods matching orbital obliquity is detected within a 95% confidence interval using the windowed inverse. Ridge extraction identified this same oscillation across most of the record, indicating it is present above the estimated noise floor and, thus, a significant periodicity present in the time series.

Reconstructing this oscillation allows the direct comparison with a normalized obliquity numerical solution, upon comparison, it is determined that the alternating bands of carbonate rich and depleted red clays are driven by orbital obliquity during 3400-4500 Ka. This chapter also demonstrates orbital obliquity is the primary control on the alternating bands of clean and carbonate rich soil successions deposited in the Chinese red clays.

Building on the importance of high-resolution records and reliable age models and dating methods to determine the presence of short climate cycles relative to record length, Chapter 4 presents new palynological proxies from Siberia from the Pleistocene. Accelerator Mass Spectrometry 14C dates were used as the basis to construct a robust nonlinear age model using Bayesian statistics. The approach uses these values to construct a non-gaussian autoregressive model for sediment accumulation which is informed by *a priori* knowledge of typical accumulation rates, the age model developed using this technique placed the succession as deposited in the Last Glacial Maxima. As compared to the Holocene, the nature of centennial and millennial scale climate oscillations in the Last Glacial Maxima are not as well understood, primarily due to resolution constraints of existing proxies. This process is recognized to provide more stable sedimentation accumulation rates and does not display abrupt changes that linear interpolation methods can show. With the age model applied to the new palynological proxy record, the time series is analyzed using the Continuous Wavelet Transform. Cycles with centennial and millennial scale periodicities are detected and match the periods of those observed in the Holocene, demonstrating that these oscillations are a lasting attribute of climate change and not specific to conditions present in the Holocene

epoch. These cycles were validated using additional high-resolution paleoclimate proxies spanning the Last Glacial Maximum.

Directions for Future Work

The proxies in chapter 2 are representative of marine or coastal environments, it is still unknown if the mid-Holocene transition observed in these environments would be prevalent in continental settings. Over the past decade, several continental Holocene paleoclimate proxies have been developed, such as the magnetic susceptibility record from Kravchinsky et al. (2013). The inverse SST methodology would be very useful in analyzing these records and allow a direct comparison of relative amplitudes in the time domain to determine if the effects of the mid-Holocene transition are as strong in continental settings as they are in marine or coastal environments. The approach illustrated in the Holocene in Chapter 2 could be applied much more broadly to a full database of paleoclimate proxies where the envelope for each reconstructed mode can be extracted using the Hilbert Transform, allowing the process to be automated. The output from this could then be used to create a map showing the evolution of climate oscillations for a specific continent over a given geologic time period such as the Holocene where countless paleoclimate proxies are available. The methodology could be further refined to use the 95% confidence intervals determined by injection of red noise to prevent oscillations below this threshold to be reconstructed by the ISST by applying a frequency dependent threshold. Multivariate spectral analysis methods such as the maximum entropy method (Zhang et al., 2018) may provide an alternative method to parse a wide array of paleoclimate proxies simultaneously.

The work presented in chapter 3 could be expanded to incorporate data from other studies, which present different data types such as geochemical measurements to develop a composite record with an improved signal-to-noise ratio compared to the individual magnetic susceptibility measurements. Mineral magnetic data collected by Ao et al. (2018) revealed differences in response between superparamagnetic, and stable single domain magnetic mineralogizes and related these to increased extent of oxidation during pedogenesis. In addition, calcimetry measurements could be utilized to quantify the amount of calcium carbonate present in a sample and thus provide opportunities to assess temporal relationships that may exist between the of superparamagnetic grain development and calcium carbonate nucleation. This will allow further refinement of the age model, and thus provides enhanced clarity and additional confidence in even higher frequency oscillations such as orbital precession, which has never been observed in the Chinese red clay deposits.

Furthermore, while it is difficult to externally validate the age model due to the limited number of continental Mio-Pliocene paleoclimate proxies of sufficient resolution, alternative dating methods could be further explored to add additional age constraints. Recent advances in the use of cosmogenic nuclides have allowed enhanced detection of minute, trace concentrations of isotopes formed in the atmosphere in the presence of solar radiation. This approach quantifies the duration of surface exposure for a given sample by analyzing the changes in concentration of isotopes such as ^{10}Be, and ^{26}Al (Schaefer et al. 2022). While the method is still highly experimental, it is possible that trace amounts of these isotopes may be detectable in the Shilou red clay samples, thus providing a supplement to current dating using only magnetic methods. The use of cosmogenic

nuclides as a means of obtaining surface exposure durations may provide additional

validation to any paleoclimate proxy discussed in this work.

References

Adolphi, F., Muscheler, R., Svensson, A., Aldahan, A., Possnert, G., Beer, J., Sjolte, J., Björck, S., Matthes, K. & Thieblemont, R. 2014. Persistent link between solar activity and Greenland climate during the Last Glacial Maximum. *Nature Geoscience*, 7(9), 662-666.

Allan, M., Deliège, A., Verheyden, S., Nicolay, S., Quinif, Y. & Fagel, N. 2018. Evidence for solar influence in a Holocene speleothem record (Père Noël cave, SE Belgium). *Quaternary Science Reviews*, *192*, 249-262.

Allen, J.B. & Rabiner, L.R. 1977. A unified approach to short-time Fourier analysis and synthesis. *Proceedings of the IEEE*, *65*(11), 1558-1564.

Alonso-Zarza, A. M., Zhao, Z., Song, C. H., Li, J.J., Zhang, J., Martin- Perez, A.,Martín- García, R., Wang, X.X., Zhang, Y. and Zhang, M.H. 2009. Mudflat/distal fan and shallow lake sedimentation (upper Vallesian-Turolian) in the Tianshui Basin, Central China: evidence against the late Miocene eolian loess. Sedimentary Geology 222,42–51

Andersen KK, Azuma N, Barnola JM, Bigler M, Biscaye P, Caillon N, Chappellaz J, Clausen HB, Dahl-Jensen D, Fischer H, & Flückiger J. 2004. High-resolution record of Northern Hemisphere climate extending into the last interglacial period. *Nature* 431, (7005), 147-151.

An, Z., Colman, S. M., Zhou, W., Li, X., Brown, E. T., Jull, A. T., Cai, Y., Huang, Y., Lu, X., Chang, H., Song, Y., 2012. Interplay between the Westerlies and Asian monsoon recorded in Lake Qinghai sediments since 32 ka. Scientific reports. 2, 619.

An, Z.,., Kutzbach, J. E., Prell, W. L., & Porter, S. C. 2001. Evolution of Asian monsoons and phased uplift of the Himalaya–Tibetan plateau since Late Miocene times. *nature*, *411*(6833), 62-66.

Anwar, T., Kravchinsky, V. A., & Zhang, R. 2015. Magneto-and cyclostratigraphy in the red clay sequence: New age model and paleoclimatic implication for the eastern Chinese Loess Plateau. *Journal of Geophysical Research: Solid Earth*, *120*(10), 6758-6770.

Ao, H., Dekkers, M.J., Roberts, A.P., Rohling, E.J., An, Z., Liu, X., Jiang, Z., Qiang, X., Xu, Y. & Chang, H., 2018. Mineral magnetic record of the Miocene-Pliocene climate transition on the Chinese Loess Plateau, North China. *Quaternary Research*, *89*(3), 619-628.

Ao, H., Roberts, A.P., Dekkers, M.J., Liu, X., Rohling, E.J., Shi, Z., An, Z. & Zhao, X., 2016. Late Miocene–Pliocene Asian monsoon intensification linked to Antarctic ice-sheet growth. *Earth and Planetary Science Letters*, *444*, 75-87.

Ao, H., Rohling, E.J., Zhang, R., Roberts, A.P., Holbourn, A.E., Ladant, J.B., Dupont-Nivet, G., Kuhnt, W., Zhang, P., Wu, F. & Dekkers, M.J., 2021. Global warming-induced Asian hydrological climate transition across the Miocene–Pliocene boundary. Nature communications, 12(1), 1-13.

Bekara, M. and Van der Baan, M. 2009. Random and coherent noise attenuation by empirical mode decomposition. *Geophysics*, *74*(5), 89-98.

Bezrukova, E.V., Tarasov, P.E., Solovieva, N., Krivonogov, S.K., Riedel, F., 2010. Last glacial-interglacial vegetation and environmental dynamics in southern Siberia: chronology, forcing and feedbacks. Palaeogeography, Palaeoclimatology, Palaeoecology. 296, 185–198.

Bezrukova, E.V., Tarasov, P.E., Kulagina, N.V., Abzaeva, A.A., Letunova, P.P., Kostrova, S.S., 2011. Palynological study of Lake Kotokel' bottom sediments

(Lake Baikal region). Russian Geology and Geophysics. 52(4), 458–465.

Blaauw, M., & Christen, J. A., 2011. Flexible paleoclimate age-depth models using an autoregressive gamma process. *Bayesian analysis*. *6*(3), 457-474.

Blaauw, M., Christen, J. A., Bennett, K. D., & Reimer, P. J., 2018. Double the dates and go for Bayes—Impacts of model choice, dating density and quality on chronologies. Quaternary Science Reviews. 188, 58-66.

Bond, G., Showers, W., Cheseby, M., Lotti, R., Almasi, P., DeMenocal, P., Priore, P., Cullen, H., Hajdas, I., & Bonani, G. 1997. A pervasive millennial-scale cycle in North Atlantic Holocene and glacial climates. *Science*, *278*(5341), 1257-1266.

Bond, G.C., Showers, W., Elliot, M., Evans, M., Lotti, R., Hajdas, I., Bonani, G., Johnson, S., 1999. The North Atlantic's 1–2 kyr climate rhythm: relation to Heinrich events, Dansgaard/Oeschger cycles and the little ice age, in: Clark, P.U., Webb R.S., Keigwin, L.D. (Eds.), Mechanisms of Global Change at Millennial Time Scales. Geophysical Monograph, American Geophysical Union, Washington DC, pp. 59–76.

Bond, G., Kromer, B., Beer, J., Muscheler, R., Evans, M. N., Showers, W., Hoffman, S., Lotti-Bond, R., Hajdas, I., & Bonani, G. 2001. Persistent solar influence on North Atlantic climate during the Holocene. *Science*, *294*(5549), 2130-21.

Bianchi, G.G., McCave, I.N., 1999. Holocene periodicity in North Atlantic climate and deep-ocean flow south of Iceland. Nature. 397, 515–517.

Borowiecki, R., Kravchinsky, V.A., van der Baan, M., & Herrera, H. 2023 The Synchrosqueezing Transform to evaluate paleoclimate cyclicity. Under review in Computers and Geosciences.

Bray, J. R. 1968. Glaciation and solar activity since the fifth century BC and the solar cycle. *Nature*, *220*, 672-674.

Clark, P.U., Dyke, A.S., Shakun, J.D., Carlson, A.E., Clark, J., Wohlfarth, B., Mitrovica, J.X., Hostetler, S.W., McCabe, A.M., 2009. The Last Glacial Maximum. Science. 325(5941), 710–714.

Clark, P.U., Shakun, J.D., Baker, P.A., Bartlein, P.J., Brewer, S., Brook, E., Carlson, A. E., Cheng, H., Kaufman, D.S., Liu, Z., Marchitto, T.M., 2012. Global climate evolution during the last deglaciation. Proceedings of the National Academy of Sciences. 109(19), E1134–E1142.

Claussen, M., Ganopolski, A., Brovkin, V., Gerstengarbe, F.W., Werner, P., 2003. Simulated global-scale response of the climate system to Dansgaard/Oeschger and Heinrich events. Climate Dynamics. 21(5-6), 361–370.

Clemens, S.C. 2005. Millennial-band climate spectrum resolved and linked to centennial-scale solar cycles. *Quaternary Science Reviews, 24(5-6),* 521-531.

Dansgaard, W. 1964. Stable isotopes in precipitation. *tellus*, *16*(4), 436-468.

Dansgaard, W., Johnsen, S.J., Clausen, H.B., Dahl-Jensen, D., Gundestrup, N.S., Hammer, C.U., Hvidberg, C.S., Steffensen, J.P., Sveinbjörnsdottir, A.E., Jouzel, J. & Bond, G. 1993. Evidence for general instability of past climate from a 250-kyr ice-core record. *Nature*, *364*(6434), 218-220.

Darby, D.A., Ortiz, J.D., Grosch, C.E. & Lund, S.P. 2012. 1,500-year cycle in the Arctic Oscillation identified in Holocene Arctic sea-ice drift. *Nature Geoscience, 5(12),* 897-900.

Daubechies, I. 1992. Ten lectures on wavelets. *Society for industrial and applied mathematics.*

Daubechies, I., Lu, J., & Wu, H. T. 2011. Synchrosqueezed wavelet Transforms: An empirical mode decomposition-like tool. *Applied and computational harmonic analysis*, *30*(2), 243-261.

Debret, M., Bout-Roumazeilles, V., Grousset, F., Desmet, M., McManus, J. F., Massei, N., Sebag D., Petit JR., Copard Y., & Trentesaux, A. 2007. The origin of the 1500-year climate cycles in Holocene North-Atlantic records. *Climate of the Past Discussions*, *3*(2), 679-692.

Debret, M., Sebag, D., Crosta, X., Massei, N., Petit, J. R., Chapron, E., & Bout-Roumazeilles, V. 2009. Evidence from wavelet analysis for a mid-Holocene transition in global climate forcing. *Quaternary Science Reviews*, *28*(25-26), 2675-2688.

Di Rita, F., Fletcher, W.J., Aranbarri, J., Margaritelli, G., Lirer, F. & Magri, D. 2018. Holocene forest dynamics in central and western Mediterranean: periodicity, spatio-temporal patterns and climate influence. *Scientific reports, 8(1)*, 1-13.

Dima, M. and Lohmann, G., 2009. Conceptual model for millennial climate variability: a possible combined solar-thermohaline circulation origin for the ~ 1,500-year cycle. Climate Dynamics, 32(2), 301-311.

Ditlevsen, P. D., Andersen, K. K., & Svensson, A. 2007. The DO-climate events are probably noise induced: statistical investigation of the claimed 1470 years cycle. *Climate of the Past*, *3*(1), 129-134.

Donoho, D., 1995. De-noising by soft-thresholding: IEEE Transactions on Information Theory 41, 613–627.

Evans, M. E., Wang, Y., Rutter, N., & Ding, Z. 1991. Preliminary magnetostratigraphy of the red clay underlying the loess sequence at Baoji, China. *Geophysical Research Letters*, *18*(8), 1409-1412.

Fletcher, W.J., Debret, M. & Goñi, M.F.S., 2013. Mid-Holocene emergence of a low-frequency millennial oscillation in western Mediterranean climate: Implications for past dynamics of the North Atlantic atmospheric westerlies. *The Holocene, 23(2)*, 153-166.

Friis-Chrisensen, E., Svensmark, H., 1997. What do we really know about the sun–climate connection? Advances in Space Research. 20, 913–921.

Gong, D.Y., Wang, S.W., Zhu, J.H., 2001). East Asian winter monsoon and Arctic oscillation. Geophysical Research Letters. 28(10*)*, 2073–2076.

Gray, L.J., Beer, J., Geller, M., Haigh, J.D., Lockwood, M., Matthes, K., Cubasch, U., Fleitmann, D., Harrison, G., Hood, L., Luterbacher, J., 2010. Solar influences on climate. Reviews of Geophysics, 48(4).

Grootes, P.M., Stuiver, M., 1997. Oxygen 18/16 variability in Greenland snow and ice with 10−3 to 105 year time resolution. Journal of Geophysical Research: Oceans, 102(C12), 26455-26470.

Gylesjö, S., & Arnold, E. 2006. Clay mineralogy of a red clay–loess sequence from Lingtai, the Chinese Loess Plateau. *Global and Planetary Change*, *51*(3-4), 181-194.

Hao, Q., & Guo, Z. 2007. Magnetostratigraphy of an early-middle Miocene loess-soil sequence in the western Loess Plateau of China. *Geophysical Research Letters*, *34*(18).

Heller, F., & Evans, M. E. 1995. Loess magnetism. *Reviews of Geophysics*, *33*(2), 211-240.

Holland, M. M., & Bitz, C. M. 2003. Polar amplification of climate change in coupled models. *Climate Dynamics*, *21(3-4)*, 221-232.

Herrera, R. H., Han, J., & van der Baan, M. 2014. Applications of the synchrosqueezing transform in seismic time-frequency analysis. *Geophysics*, *79*(3), V55-V64.

Herrera, R. H., Tary, J. B., van der Baan, M., & Eaton, D. W. 2015. Body Wave Separation in the Timefrequency Domain, Geoscience and Remote Sensing Letters. *IEEE*, *12*(2), 364-368.

Herrera, R. H., Fomel, S., & Van Der Baan, M. 2014. Automatic approaches for seismic to well tying. *Interpretation*, *2*(2), SD9-SD17.

Heslop, D., Dekkers, M. J., & Langereis, C. G. 2002. Timing and structure of the mid-Pleistocene transition: records from the loess deposits of northern China. *Palaeogeography, Palaeoclimatology, Palaeoecology*, *185*(1-2), 133-143.

Hu, F. S., Kaufman, D., Yoneji, S., Nelson, D., Shemesh, A., Huang, Y., Tian, J., Bond, G., Clegg, B., & Brown, T. 2003. Cyclic variation and solar forcing of Holocene climate in the Alaskan subarctic. *Science, 301(5641),* 1890-1893.

Jouzel, J., Lorius, C., Petit, J. R., Genthon, C., Barkov, N. I., Kotlyakov, V. M., & Petrov, V. M. 1987. Vostok ice core: a continuous isotope temperature record over the last climatic cycle (160,000 years). *Nature*, *329*(6138), 403.

Kaufman, D., McKay, N., Routson, C., Erb, M., Davis, B., Heiri, O., Jaccard, S., Tierney, J., Dätwyler, C., Axford, Y., Brussel, T., 2020. A global database of Holocene paleotemperature records. Scientific data. 7(1), 1-34.

Kindler, P., Guillevic, M., Baumgartner, M., Schwander, J., Landais, A. and Leuenberger, M., 2014. Temperature reconstruction from 10 to 120 kyr b2k from the NGRIP ice core. Climate of the Past, 10(2), 887-902.

Kostrova, S.S., Meyer, H., Tarasov, P.E., Bezrukova, E.V., Chaplgin, B., Kossler, A., Pavlova, L.A., Kuzmin, M.I., 2016. Oxygen isotope composition of diatoms from sediments of Lake Kotokel (Buryatia). Russian Geology and Geophysics. 57(8),

1239–1247.

Kravchinsky, V. A., Krainov, M. A., Evans, M. E., Peck, J. A., King, J. W., Kuzmin, M. I., Sakai, H., Kawai, T., & Williams, D. F., 2003. Magnetic record of Lake Baikal sediments: chronological and paleoclimatic implication for the last 6.7 Myr. *Palaeogeography, Palaeoclimatology, Palaeoecology*, *195*(3-4), 281-298.

Kravchinsky, V. A., Langereis, C. G., Walker, S. D., Dlusskiy, K. G., & White, D. 2013. Discovery of Holocene millennial climate cycles in the Asian continental interior: Has the sun been governing the continental climate?. *Global and Planetary Change*, *110*, 386-396.

Kravchinsky, V.A., Zhang, R., Borowiecki, R., Tarasov, P.E., van der Baan, M., Anwar, T., Goguitchaichvili, A., & Müller, S., 2021. Centennial scale climate oscillations from southern Siberia in the Last Glacial Maximum. *Quaternary Science Reviews, 270*, 107171.

Laskar, J., Fienga, A., Gastineau, M., & Manche, H. 2011. La2010: a new orbital solution for the long-term motion of the Earth. Astronomy & Astrophysics, 532, A89.

Loehle, C., Singer, S.F., 2010. Holocene temperature records show millennial-scale periodicity. Canadian Journal of Earth Sciences. 47, 1327–1336.

Long, J.A., Stoy, P.C., 2013. Quantifying the periodicity of Heinrich and Dansgaard-Oeschger events during marine oxygen isotope stage 3. Quaternary Research, 79(3), 413-423.

Lorius, C., Jouzel, J., Ritz, C., Merlivat, L., Barkov, N. I., Korotkevich, Y. S., & Kotlyakov, V. M. 1985. A 150,000-year climatic record from Antarctic ice. *Nature*, *316*(6029), 591.

Loutre, M.F., Berger, A., Bretagnon, P., Blanc, P.-L., 1992. Astronomical frequencies for climate research at the decadal to century time scale. Climate Dynamics. 7, 181–194.

Lüdecke, H. J., Weiss, C. O., & Hempelmann, A. 2015. Paleoclimate forcing by the solar De Vries/Suess cycle. *Climate of the Past Discussions, 11(1),* 279-305.

Luetscher, M., Boch, R., Sodemann, H., Spötl, C., Cheng, H., Edwards, R.L., Frisia, S., Hof, F., Müller, W., 2015. North Atlantic storm track changes during the Last Glacial Maximum recorded by Alpine speleothems. Nature Communications, 6, 6344.

Mallat, S. G., & Zhang, Z. 1993. Matching pursuits with time-frequency dictionaries. *IEEE Transactions on signal processing*, *41*(12), 3397-3415.

Marsicek, J., Shuman, B.N., Bartlein, P.J., Shafer, S.L. and Brewer, S., 2018. Reconciling divergent trends and millennial variations in Holocene temperatures. Nature, 554(7690), 92.

Martin-Puertas, C., Matthes, K., Brauer, A., Muscheler, R., Hansen, F., Petrick, C., Aldahan, A., Possnert, G., Van Geel, B., 2012. Regional atmospheric circulation shifts induced by a grand solar minimum. Nature Geoscience, 5(6), 397-401.

McMichael, A.J., 2012. Insights from past millennia into climatic impacts on human health and survival. Proceedings of the National Academy of Sciences. 109(13), 4730–4737.

Mingram, J., Stebich, M., Schettler, G., Hu, Y., Rioual, P., Nowaczyk, N., Dulski, P., You, H., Opitz, S., Liu, Q. and Liu, J., 2018. Millennial-scale East Asian monsoon variability of the last glacial deduced from annually laminated sediments from Lake Sihailongwan, NE China. Quaternary Science Reviews, 201, 57-76.

Moreno, A., Svensson, A., Brooks, S.J., Connor, S., Engels, S., Fletcher, W., Genty, D., Heiri, O., Labuhn, I., Perşoiu, A. and Peyron, O., 2014. A compilation of Western European terrestrial records 60–8 ka BP: towards an understanding of latitudinal climatic gradients. Quaternary Science Reviews, 106, 167-185.

Müller, S., Tarasov, P.E., Hoelzmann, P., Bezrukova, E.V., Kossler, A., Krivonogov, S.K., 2014. Stable vegetation and environmental conditions during the Last Glacial Maximum: New results from Lake Kotokel (Lake Baikal region, southern Siberia, Russia). Quaternary International. 348, 14–24.

Nie, J., King, J. W., & Fang, X. 2007. Enhancement mechanisms of magnetic susceptibility in the Chinese red-clay sequence. *Geophysical Research Letters*, *34*(19).

Nie, J., Song, Y., & King, J. W. 2016. A review of recent advances in red-clay environmental magnetism and paleoclimate history on the Chinese Loess Plateau. *Frontiers in Earth Science*, *4*, 27.

Nie, J. 2018. The Plio-Pleistocene 405-kyr climate cycles. *Palaeogeography, Palaeoclimatology, Palaeoecology,* 510, 26-30.

Niggemann, S., Mangini, A., Mudelsee, M., Richter, D.K. & Wurth, G., 2003. Sub-Milankovitch climatic cycles in Holocene stalagmites from Sauerland, Germany. *Earth and Planetary Science Letters*, *216*(4), 539-547.

Nyquist, H. "Certain Factors Affecting Telegraph Speed," Bell System Technical Journal, Vol. 3, April 1924, pp. 324-346.

O'Brien, S. R., Mayewski, P. A., Meeker, L. D., Meese, D. A., Twickler, M. S., & Whitlow, S. I. 1995. Complexity of Holocene climate as reconstructed from a Greenland ice core. *Science*, *270*(5244), 1962-1964.

Obrochta, S. P., Miyahara, H., Yokoyama, Y., & Crowley, T. J. 2012. A re-examination of evidence for the North Atlantic "1500-year cycle" at Site 609. *Quaternary Science Reviews*, *55*, 23-33.

Oppenheim, A. V., & Schafer, R. W. 1999. with JR Buck. Discrete-Time Signal Processing, 2.

Paillard, D. 2001. Glacial cycles: toward a new paradigm. *Reviews of Geophysics*, *39*(3), 325-346.

Paillard, D., Labeyrie, L. D., & Yiou, P. 1996. AnalySeries 1.0: a Macintosh software for the analysis of geophysical time-series. *Eos*, *77*(39), 379.

Panagiotopoulos, F., Shahgedanova, M., Hannachi, A., Stephenson, D.B., 2005. Observed trends and teleconnections of the Siberian high: A recently declining center of action. Journal of climate. 18(9), 1411–1422.

Peavoy, D., & Franzke, C. 2010. Bayesian analysis of rapid climate change during the last glacial using greenland δ18O data. *Climate of the Past*, *6*(6), 787-794.

Peros, M. C., & Gajewski, K. 2008. Holocene climate and vegetation change on Victoria Island, western Canadian Arctic. *Quaternary Science Reviews*, *27*(3-4), 235-249.

Petit, J. R., Jouzel, J., Raynaud, D., Barkov, N. I., Barnola, J. M., Basile, I., Bender, M., Chappellaz, J., Davis, M., Delaygue, G. & Delmotte, M. 1999. Climate and atmospheric history of the past 420,000 years from the Vostok ice core, Antarctica. *Nature*, *399*(6735), 429.

Pisias, N.G., Clark, P.U., Brook, E.J., 2010. Modes of global climate variability during marine isotope stage 3 (60–26 ka). Journal of Climate, 23(6), 1581-1588.

Qin, J., Zhang, R., Kravchinsky, V.A., Valet, J.P., Sagnotti, L., Li, J., Xu, Y., Anwar, T. & Yue, L., 2022. 1.2 Myr Band of Earth-Mars Obliquity Modulation on the Evolution of Cold Late Miocene to Warm Early Pliocene Climate. Journal of Geophysical Research: Solid Earth, 127(4), e2022JB024131.

Rahmstorf, S., 2003. Timing of abrupt climate change: A precise clock. *Geophysical Research Letters*, 30(10).

Ramos-Román, M. J., Jiménez-Moreno, G., Camuera, J., García-Alix, A., Anderson, R. S., Jiménez-Espejo, F. J., Sachse, D., Toney, J. L., Carrión, J. S., Webster, C. & Yanes, Y. 2018. Millennial-scale cyclical environment and climate variability during the Holocene in the western Mediterranean region deduced from a new multi-proxy analysis from the Padul record (Sierra Nevada, Spain). *Global and Planetary Change*, 168 35-53.

Rasmussen, S.O., Bigler, M., Blockley, S.P., Blunier, T., Buchardt, S.L., Clausen, H.B., Cvijanovic, I., Dahl-Jensen, D., Johnsen, S.J., Fischer, H., Gkinis, V., 2014. A stratigraphic framework for abrupt climatic changes during the Last Glacial period based on three synchronized Greenland ice-core records: refining and extending the INTIMATE event stratigraphy. Quaternary Science Reviews. 106, 14-28.

Reimer, P.J., Austin, W.E., Bard, E., Bayliss, A., Blackwell, P.G., Ramsey, C.B., Butzin, M., Cheng, H., Edwards, R.L., Friedrich, M., Grootes, P.M., 2020. The IntCal20 Northern Hemisphere radiocarbon age calibration curve (0–55 cal kBP). Radiocarbon, 62(4), 725-757.

Rial, J. A., & Anaclerio, C. A. 2000. Understanding nonlinear responses of the climate system to orbital forcing. *Quaternary Science Reviews*, *19*(17-18), 1709-1722.

Scafetta, N., Milani, F., Bianchini, A., Ortolani, S., 2016. On the astronomical origin of the Hallstatt oscillation found in radiocarbon and climate records throughout the Holocene. Earth-Science Reviews. 162, 24-43.

Schaefer, J. M., Codilean, A. T., Willenbring, J. K., Lu, Z. T., Keisling, B., Fülöp, R. H., & Val, P. 2022. Cosmogenic nuclide techniques. *Nature Reviews Methods Primers*, *2*(1), 18.

Schulz, M., & Paul, A. 2002. Holocene climate variability on centennial-to-millennial time scales: 1. Climate records from the North-Atlantic realm. *Climate development and history of the North Atlantic realm*, 41-54.

Seierstad, I.K., Abbott, P.M., Bigler, M., Blunier, T., Bourne, A.J., Brook, E., Buchardt, S.L., Buizert, C., Clausen, H.B., Cook, E. & Dahl-Jensen, D., 2014. Consistently dated records from the Greenland GRIP, GISP2 and NGRIP ice cores for the past 104 ka reveal regional millennial-scale δ18O gradients with possible Heinrich event imprint. *Quaternary Science Reviews*, *106*, 29-46.Shichi, K., Takahara, H., Krivonogov, S.K., Bezrukova, E.V., Kashiwaya, K., Takehara, A., Nakamura, T., 2009. Late Pleistocene and Holocene vegetation and climate records from Lake Kotokel, central Baikal region. Quaternary International. 205(1-2), 98–110.

Solanki, S.K., Krivova, N.A., Haigh, J.D., 2013. Solar irradiance variability and climate. Annual Review of Astronomy and Astrophysics, 51, 311–351.

Solotchin, P. A., Solotchina, E. P., Bezrukova, E. V., Zhdanova, A. N., 2020. Climate signals in the late quaternary bottom sediments of lake Baunt (Northern Transbaikalia). Russian Geology and Geophysics. 61(10), 1146-1155.

Soon, W., Herrera, V. M. V., Selvaraj, K., Traversi, R., Usoskin, I., Chen, C. T. A., Lou, J.Y., Kao, S.J., Carter, R.M., Pipin, V. & Severi, M. 2014. A review of Holocene solar-linked climatic variation on centennial to millennial timescales: Physical processes, interpretative frameworks and a new multiple cross-wavelet Transform algorithm. *Earth-Science Reviews, 134*, 1-15.

Sorrel, P., Debret, M., Billeaud, I., Jaccard, S. L., McManus, J. F., & Tessier, B. 2012. Persistent non-solar forcing of Holocene storm dynamics in coastal sedimentary archives. *Nature Geoscience, 5(12)*, 892-896.

Steinhilber F., Abreu J.A., Beer J., Brunner I., Christl M., Fischer H., Heikkilä U., Kubik P.W., Mann M., McCracken K.G. & Miller H. 2012. 9,400 years of cosmic radiation and solar activity from ice cores and tree rings. *Proceedings of the National Academy of Sciences. 109 (16),* 5967-71.

Sun, Y., Clemens, S. C., An, Z., & Yu, Z. 2006. Astronomical timescale and palaeoclimatic implication of stacked 3.6-Myr monsoon records from the Chinese Loess Plateau. *Quaternary Science Reviews*, *25*(1), 33-48.

Sun, Y., Clemens, S.C., Morrill, C., Lin, X., Wang, X., An, Z., 2012. Influence of Atlantic meridional overturning circulation on the East Asian winter monsoon. *Nature Geoscience*, 5(1), 46.

Sun, D., Shaw, J., An, Z., Cheng, M., & Yue, L. 1998. Magnetostratigraphy and paleoclimatic interpretation of a continuous 7.2 Ma Late Cenozoic eolian sediments from the Chinese Loess Plateau. *Geophysical Research Letters*, *25*(1), 85-88.

Smith, A., Wynn, P., Barker, P., Leng, M., Noble, S., & Stott, A. 2016. Cave monitoring and the potential for palaeoclimate reconstruction from Cueva de Asiul, Cantabria (N. Spain). *International Journal of Speleology*, *45*(1), 1-9.

Tarasov, P., Granoszewski, W., Bezrukova, E., Brewer, S., Nita, M., Abzaeva, A., Oberhänsli, H., 2005. Quantitative reconstruction of the last interglacial vegetation and climate based on the pollen record from Lake Baikal, Russia. Climate Dynamics. 25(6), 625–637.

Tarasov, P.E., Bezrukova, E.V., Krivonogov, S.K., 2009. Late Glacial and Holocene changes in vegetation cover and climate in southern Siberia derived from a 15 kyr long pollen record from Lake Kotokel. Climate of the Past. 5(3*)*, 285–295.

Tary, J.B., Herrera, R.H., Han, J. & van der Baan, M., 2014. Spectral estimation—What is new? What is next?. *Reviews of Geophysics, 52(4),* 723-749.

Tary, J. B., Herrera, R. H., & van der Baan, M. 2018. Analysis of time-varying signals using continuous wavelet and synchrosqueezed transforms. *Philosophical Transactions of the Royal Society A: Mathematical, Physical and Engineering Sciences*, *376*(2126), 20170254.

Torrence, C., & Compo, G. P. 1998. A practical guide to wavelet analysis. *Bulletin of the American Meteorological Society*, *79*(1), 61-78.

Turner, T. E., Swindles, G. T., Charman, D. J., Langdon, P. G., Morris, P. J., Booth, R. K., Parry, L.E., & Nichols, J. E. 2016. Solar cycles or random processes? Evaluating solar variability in Holocene climate records. *Scientific reports, 6,* 23961.

Usoskin, I. G., Gallet, Y., Lopes, F., Kovaltsov, G. A., & Hulot, G. 2016. Solar activity during the Holocene: the Hallstatt cycle and its consequence for grand minima and maxima. *Astronomy & Astrophysics*, *587*, A150.

Van Geel, B., Raspopov, O. M., Renssen, H., Van der Plicht, J., Dergachev, V. A., & Meijer, H. A. J. 1999. The role of solar forcing upon climate change. Q*uaternary Science Reviews, 18(3)*, 331-338.

Voiculescu, M., Usoskin, I., 2012. Persistent solar signatures in cloud cover: spatial and temporal analysis. *Environmental Research Letter*s, 7(4), p.044004.

Vonmoos, M., Beer, J., Muscheler, R., 2006. Large variations in Holocene solar activity: Constraints from 10Be in the Greenland Ice Core Project ice core. *Journal of Geophysical Research: Space Physics*. 111(A10).

Wang, Y., Cheng, H., Edwards, R.L., He, Y., Kong, X., An, Z., Wu, J., Kelly, M.J., Dykoski, C.A. and Li, X., 2005. The Holocene Asian monsoon: links to solar changes and North Atlantic climate. *Science*, 308(5723), 854-857.

Wanner, H., Beer, J., Bütikofer, J., Crowley, T.J., Cubasch, U., Flückiger, J., Goosse, H., Grosjean, M., Joos, F., Kaplan, J.O. & Küttel, M., 2008. Mid-to Late Holocene climate change: an overview. *Quaternary Science Reviews, 27(19-20)*, 1791-1828.

Wanner, H., & Buetikofer, J. 2008. Holocene Bond Cycles: real or imaginary. *Geografie*, *113*(4), 338-349.

Williams, D. F., Peck, J., Karabanov, E. B., Prokopenko, A. A., Kravchinsky, V., King, J., & Kuzmin, M. I. 1997. Lake Baikal record of continental climate response to orbital insolation during the past 5 million years. *Science*, *278*(5340), 1114-1117.

Wunsch, C., 2000. On sharp spectral lines in the climate record and the millennial peak. *Paleoceanography*, 15(4), 417-424.

Xu, Y., Yue, L., Li, J., Sun, L., Sun, B., Zhang, J., Ma, J., & Wang, J. 2009. An 11-Ma-old red clay sequence on the Eastern Chinese Loess Plateau. *Palaeogeography, Palaeoclimatology, Palaeoecology*, *284*(3-4), 383-391.

Zhang, R., Li, X., Xu, Y., Li, J., Sun, L., Yue, L., Pan, F., Xian, F., Wei, X. and Cao, Y. 2022. The 173 kyr Obliquity Cycle Pacing the Asian Monsoon in the Eastern Chinese Loess Plateau From Late Miocene to Pliocene. *Geophysical Research Letters*, *49*(2).

Zhang, X., Lohmann, G., Knorr, G., Purcell, C., 2014. Abrupt glacial climate shifts controlled by ice sheet changes. Nature. 512(7514), 290–294.

Zhang, Z., Zhang, K., & Khelifi, A. 2018. *Multivariate time series analysis in climate and environmental research*. Cham: Springer International Publishing.